GUEST-MOLECULE DYNAMICS & CONDUCTIVITY EFFECTS IN CARBON-BASED MOLECULAR SOLIDS

EFSTRATIA MITSARI

SUPERVISORS:
Dr. Roberto MACOVEZ
Prof. Dr. Josep Lluís TAMARIT MUR

Barcelona, June 2016
PhD programme in Computational and Applied Physics
DEPARTAMENT DE FÍSICA

UNIVERSITAT POLITÈCNICA
DE CATALUNYA
BARCELONATECH

Cover Design: Isaac Sànchez Lastra

UNIVERSITAT POLITÈCNICA DE CATALUNYA
BARCELONA**TECH**
Escola de Doctorat

Acta de calificación de tesis doctoral

Curso académico:

Nombre y apellidos

Programa de doctorado

Unidad estructural responsable del programa

Resolución del Tribunal

Reunido el Tribunal designado a tal efecto, el doctorando / la doctoranda expone el tema de la su tesis doctoral titulada ____

____

Acabada la lectura y después de dar respuesta a las cuestiones formuladas por los miembros titulares del tribunal, éste otorga la calificación:

☐ NO APTO ☐ APROBADO ☐ NOTABLE ☐ SOBRESALIENTE

(Nombre, apellidos y firma) Presidente/a	(Nombre, apellidos y firma) Secretario/a

(Nombre, apellidos y firma) Vocal	(Nombre, apellidos y firma) Vocal	(Nombre, apellidos y firma) Vocal

________________________, ________ de ____________________ de _________________

El resultado del escrutinio de los votos emitidos por los miembros titulares del tribunal, efectuado por la Escuela de Doctorado, a instancia de la Comisión de Doctorado de la UPC, otorga la MENCIÓN CUM LAUDE:

☐ SÍ ☐ NO

(Nombre, apellidos y firma) Presidente de la Comisión Permanente de la Escuela de Doctorado	(Nombre, apellidos y firma) Secretario de la Comisión Permanente de la Escuela de Doctorado

Barcelona a ________ de ______________________ de ___________

Στην οικογένεια μου...

ABSTRACT

Disordered systems are abundant in everyday life and so their study is of importance from a scientific and a technological point of view. The most common non-crystalline solid phases are structural glasses (of which ordinary window glass is an example), in which both translational and orientational degrees of freedom are disordered. While at low temperature (in the glass state) the disorder is static, at higher temperature a viscous molten state is reached, where the disorder is dynamic (as in a normal liquid). Other systems exist, namely molecular solids, which display different types of disorder (either static or dynamic depending on temperature) due to the larger variety of microscopic degrees of freedom compared to atomic solids (chapter 1). For instance, molecular solids display phases in which the molecules' average centers of mass occupy lattice positions while their orientations are disordered (*orientationally disordered phases*). Such phases are usually formed by small molecules or molecules with a globular shape like the carbon-only fullerene molecule (C_{60}). Molecular solids display low electrical conductivities due to localization of valence electrons on single molecules, so that electron hopping is the main charge transport mechanism. The type of disorder, and whether it is static or dynamic, are both factors that have an important impact on the conductivity.

This thesis is an experimental study of the dynamic disorder and conduction properties of molecular solids, focusing in particular on

hydrated molecular materials and on fullerene systems. The experimental technique of choice, which allows studying simultaneously molecular dynamics and electrical conductivity, is broadband dielectric spectroscopy (chapters 2 and 3). Studying water inside organic systems is of great importance in several contexts, ranging from the study of food texture and quality and the stability of biotechnology products and pharmaceuticals to the investigation of macromolecular function in cellular and other biochemical systems for which hydration water plays a preeminent role. Fullerene solids are relatively simple systems to study the impact of water and in general of heterogeneous species inside an organic matrix. Hydrophilic or hygroscopic fullerene derivatives can be obtained by functionalization with oxygen or hydroxyl groups, as in the case of the fullerenol molecule ($C_{60}(OH)_{24}$, chapter 5) We show in this thesis that water molecules not only display interesting orientational dynamics, but they also contribute to the enhancement of the conductivity due to proton hopping through surface hydration layers. These phenomena are not specific to functionalized fullerenes (chapter 5) but also to other organic materials, as we show for the case of an organic dye of the rhodamine family (chapter 4). As for the dynamics of the fullerene molecules themselves, it is well known that the solid phase of pure C_{60} exhibits order-disorder orientational transition. We show that a derivative of C_{60} functionalized with oxygen-containing groups and produced by a standard oxidaton procedure, also displays several orientational transitions (chapter 6). A decrease in the electronic conductivity accompanies the full orientational melting at high temperature, reminescent of that of solid C_{60}. Finally, we analyze the structural and dynamic orientational disorder in a co-crystal of C_{60} with a small ethane derivative (C_{60}:(1,1,2)-trichloroethane, chapter 7). We are able to observe two distinct orientational dynamics of the ethane molecules. To the best of our knowledge, ours is the first-ever report of the relaxation dynamics of guest molecules intercalated inside C_{60}. Considering the very broad variety of (partially) disordered structures that can be obtained in binary systems containing fullerene molecules, these solids may represent model systems to investigate the impact of disorder and of the interaction geometry on the molecular dynamics of heterogeneous systems. The results of this thesis represent a first step in the direction of extending the current experimental knowledge of disordered solid phases to more complex systems of relevance in organic chemistry and biology, or with possible commercial applications.

CONTENTS

1. INTRODUCTION 1

1.1 Disordered Solids 3

1.1.1 Molecular Solids 4

1.2 Conduction mechanisms in disordered solids 8

1.3 Water inside molecular solids 11

1.4 Outline of the thesis 14

2. DIELECTRIC RELAXATIONS AND CONDUCTIVITY CONTRIBUTIONS IN SOLIDS 21

2.1 Introduction 21

2.2 Dielectrics in electric fields 23

2.3 Polarization Mechanisms 26

2.4 Charge-Transport Mechanisms and related dielectric losses 32

2.5 Dielectric relaxation processes 40

3. EXPERIMENTAL TECHNIQUES 49

3.1 Thermal Analysis Methods 49

3.1.1 Thermogravimetric Analysis 49

3.1.2 Differential Scanning Calorimetry 51

3.2 Vibrational Spectroscopy Techniques (FTIR, RAMAN) 53

3.2.1 Fourier-transform Infrared Spectroscopy 53

3.2.2 Raman Spectroscopy 54

3.3 X-ray powder diffraction 55

3.4 Broadband Dielectric Spectroscopy 56

3.5 Analysis of Dielectric Data 60

3.5.1 Relaxations Models 61

4. DYNAMICS OF WATER INSIDE SOLID RHODAMINE 6G 69

4.1 Introduction 69

4.2 Experimental methods 71

4.3 Thermal Analysis of hydrated Rh6G 72

4.4 FT-IR characterization of Rhodamine 6G 77

4.5 Broadband Dielectric Spectroscopy study 81

4.6 Dielectric Relaxations intrinsic of Rhodamine 6G 89

4.7 Analysis of the H2O dynamics inside Rh6G 95

4.7.1 Atypical temperature-dependence of water-related dynamics 105

4.7.2 Space-charge relaxation in quasi-anhydrous Rh6G 110

4.8 Conclusions 114

5. DYNAMICS OF H2O IN SOLID FULLERENOL 121
5.1Introduction 121
5.2 Experimental methods 123
5.3 Thermal study of a hydrated fullerenol 125
5.4 Spectroscopic and Structural Characterization (FT-IR, XRD) 128
5.5 Dielectric Spectroscopy study 134
5.6 Analysis of the water relaxation dynamics 140
5.6.1 Fastest and slowest relaxation of water inside fullerenol 142
5.6.2 Intermediate relaxation of water inside fullerenol 148
5.7 Conclusions 157

6. ORIENTATIONAL TRANSITIONS& CONDUCTIVITY-INDUCED EFFECTS IN SOLID OXOFULLEROL 163
6.1Introduction 163
6.2 Experimental methods 165
6.3 FTIR analysis of oxC60 167
6.4 Thermal behavior of as-stored and water-free oxC60 169
6.5 X-ray diffraction study of the pure (water-free) compound 174
6.6 Dielectric signature of the orientational phase transitions in oxC60 179
6.7 Conclusions 190

7. C60 SOLVATE WITH (1,1,2) -TRICHLOROETHANE: DYNAMIC STATISTICAL DISORDER AND MIXED CONFORMATION 195
7.1Introduction 195
7.2 Experimental methods 198
7.3 XRD Patterns and Structural Modeling 200
7.4 Dielectric Relaxations and Raman Spectroscopy Results 204
7.5 Conclusions 215

CONCLUSIONS 223
LIST OF PUBLICATIONS 229

Chapter 1

INTRODUCTION

Matter is composed of atoms, molecules and ions. The strength and the range of the interactions between these constituent particles determine the physical state (gas, liquid, solid…) of a particular specimen. The gaseous state is composed of a collection of particles in constant motion with no interactions between them and thus no correlation. When the interactions start to become more important (e.g. by cooling down or compressing), the phase becomes more dense. A correlation then emerges between the motions and the relative positions and orientations of the particles. By further cooling, the motion is significantly reduced, and the particles end up occupying fixed positions, with only limited freedom of movement around the latter. The positions and the orientations of the particles are fully determined in the solid state; their arrangements can be regular, as in a crystalline solid, where their consituent particles are situated in a repeating three-dimensional array over large distances, or disordered, as in a glassy solid, where the dynamic disorder typical of liquid phases is “frozen” into a static disorder.

Crystalline solids are characterized by long-range order, and they correspond to the phase of lower energy (equilibrium phase) at low temperature (below the crystallization temperature). However, another type of condensed matter can result upon rapidly cooling a liquid (or a dynamically disordered system) below the crystallization temperature, in which case a glass is formed. Unlike crystals, long-range order is absent in these glassy solids. The glass phase is not an equilibrium phase, but it is nonetheless relatively stable because the limited molecular motions are not enough to allow the molecules to arrange themselves in an ordered fashion.

Disordered materials (glasses, liquids, liquid crystals, …) are more abundant in everyday life than crystalline solids, and so their study is of importance. Fundamental scientific investigations are being carried out to explore the many fascinating condensed-matter issues related with disorder.[1,2] From a technological/commercial point of view, disordered systems find applications in many areas. Applied disordered materials include for example optically transparent glasses for windows or fast signal transmission, amorphous semiconductors as photovoltaic materials and as memory elements, liquid crystals for light-emitting displays, amorphous pharmaceutical active principles with enhanced bioavailability, cosmetics and food components, biological structures, etc.[3,4,5,6]

Many biologically relevant disordered systems contain water, the most abundant liquid on earth, covering more than 70% of the earth's surface, which is also the major constituent of living organisms. Despite its ubiquity and simple chemical formula, the properties of water, both in pure form and as a component of a more complex specimen, are not yet fully understood. Studying water inside organic solids, and how it affects disorder and dynamics, is of great importance in several contexts. These range from the study of food texture and quality[7,8] and the stability of biotechnology products and pharmaceuticals[9] to the investigation of macromolecular function in cellular and other biochemical systems for which hydration water plays a preeminent role.[10,11]

1.1 Disordered Solids

Cooling rapidly a liquid below its melting point results in a metastable phase (supercooled liquid) with esentially the same local structure as the liquid above the melting point but higher viscosity. Further cooling leads to a dramatic slowing down of the particles´ motion, so as they can no longer rearrange further with respect to their neighbors to reach a more ordered configuration as in the crystal phase. When the temperature of the supercooled liquid is so low that the characterstic timescale of molecular motions becomes longer than the available experimental observation time, the supercooled liquid has become a structural glass, and its mechanical properties have change from those of a viscous fluid to those of a solid. The time that the particles need to re-arrange to an applied stress (*relaxation time*) is a characteristic time for each system and it depends on how the random thermal motion of the particles is modified by the interactions between them. Glasses formed by supercooling the liquid state are omnipresent in everyday life (window glasses, plastics, caramels,etc.). Despite their ubiquity, the nature of the transition to the glass phase (glass transition) is still an unsolved issue of condensed matter physics.[1,2]

A system can exhibit different glassy behavior depending on the degrees of freedom displaying dynamic disorder. In a liquid, these degrees of freedom that become frozen in the glass transition are the rototranslational ones, but in polymers or plastic crystals, the degrees of freedom exhibiting disorder may well be only the orientational ones, giving rise to a different kind of (orientational) glassy phase.

1.1.1 Molecular Solids

Depending on the shape of the constituent molecules and on the details of the interactions between them, molecular solids can form a variety of ordered and disordered structures (see Figure 1.1). Molecular solids (unlike the more conventional atomic systems which display only translational degrees of freedom) are composed of molecules that possess also orientational and internal degrees of freedom which lead in a richer variety of possible structural phases. These solids are usually held together by weak intermolecular forces (van der Waals) and constitute a special class of materials with own characteristic features, as pronounced polymorphism, order-disorder transitions, plasticity and strong electron-phonon and Jahn-Teller effects. Due to the relative weakness of intermolecular forces, molecular solids are soft and have relatively low melting points.

Molecular solids can display full order, so that all atoms on a given molecule occupy a fixed position in such a way that a lattice can be defined: this would be the analog of a crystal of a conventional solid, but it actually requires both translational and orientational order of the constituent molecules. At the other extreme, a fully disordered molecular glass can be formed by rapidly cooling from the molten (liquid) state. In between these two extremes, these weakly-bound solids also display phases that have no counterpart in atomic solids: for example, phases in which all molecules have the same or similar orientation but no translational order (*liquid crystals*), or phases in which the molecules' average centers of mass occupy lattice positions while their orientations are disordered (*orientationally disordered solids, OD*). A prominent example of OD solids are the so-called rotator phases (also known as *plastic crystals*), in which the constituent molecules display free-rotor motion (Figure 1.1). These phases are usually formed by small molecules such as methane[12,13,14] or ethane derivatives,[15,16,17,18] or by globular-shaped molecules such as adamantanes[19] or fullerenes.[20,21]

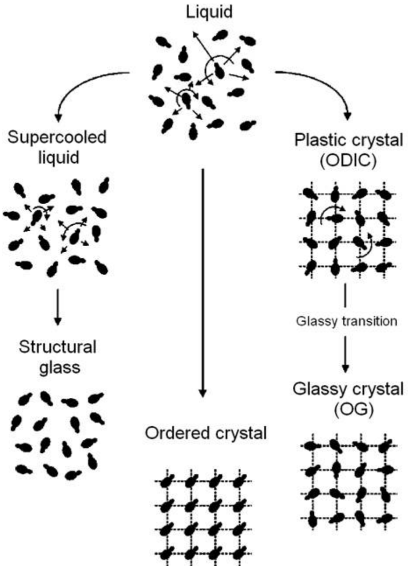

Figure 1.1 Possible transitions upon cooling down the liquid phase of non-spherical molecules: an ordered crystal, a structural glass, or an orientationally disordered glassy form.[22]

Fullerenes, with their globular (quasi-spherical) shape, display an extremely rich variety of behaviors in the solid state: OD phases with free-rotor (plastic crystalline phase) or merohedral disorder has been identified in the solid phase of many fullerenes (such as C_{60}) and their derivatives.[23,24] As the temperature is lowered, C_{60} and some of its derivatives[25] undergo solid-solid transitions which arise from the orientational (rotational) degrees of freedom.

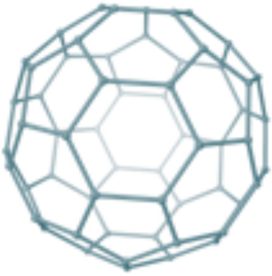

Figure1.2 Molecular structure of the C_{60} molecule.

Orientationally disordered (OD) phases exhibit many of the phenomenological features of glass formers, displaying in particular a continuous, dramatic slowing down of the dynamics of the rotational motions as the material is cooled down,[22,26] which in some cases even leads to a glass-like transition associated with the “freezing” of orientational relaxations.[27,28] Contrary to structural glasses, which do not exhibit any long-range order, OD solids are characterized by a translationally ordered structure and can therefore be more thoroughly characterized with the help of methods that exploit the translational symmetry such as Bragg diffraction, lattice models, or solid-state NMR spectroscopy.

Besides the main translational and orientational disorder, another type of disorder that can be present in molecular materials is the conformational disorder. This can be exhibited by materials whose constituent molecules can exist in more than one possible conformation (isomeric forms). If different molecular isomers are present in the liquid phase, they may be preserved in the glassy phases and even in the crystalline ones.[3] Translational[29] and orientational degress of freedom may also play a role in conformationally disordered phases.[30] Also liquid crystalline phases can display such an “intramolecular” disorder.[31]

Glass-forming systems undergo transitions between the different ordered and disordered (liquid, glass, etc.) phases by the change of thermodynamic variables (such as temperature and pressure). The effect of these variables (e.g. temperature) can be studied by probing how the macroscopic properties of the specimen (viscosity, mechanical resistance, etc.) or the microscopic properties (molecular motions) vary with temperature.[32] The characteristic timescale of motion in disordered materials can be expressed by the relaxation time, the characteristic time that the constituent molecules need to re-arrange to an applied stress (see chapter 3). For most systems where the intermolecular interactions are small, the relaxation time is thermally activated and follows an Arrhenius law (Figure 1.3), that is, it exhibits a dependence on absolute temperature (*T*) of the form:

$$\tau \propto e^{\frac{E_A}{k_B T}}. \qquad [1.1]$$

E_A is the temperature-independent activation energy, which represents the energy barrier that the molecules need to overcome in order to relax,[33] and k_B is Boltzmann's constant. At high temperature (or also at moderate temperatures if the energy barrier is low) the molecules re-arrange rapidly.

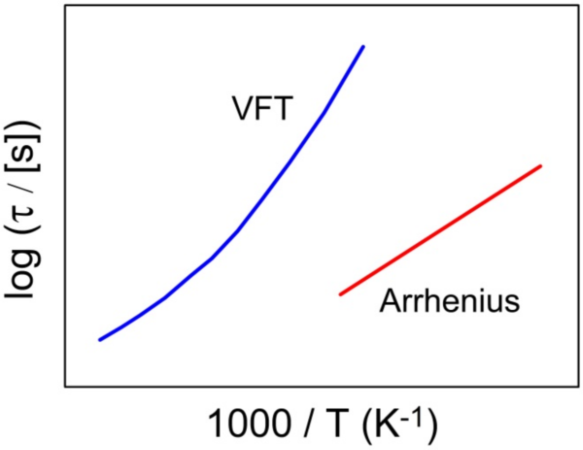

Figure1.3 Arrhenius plot of two relaxation processes with two different temperature dependences. The relaxation process at longer times (blue curve) is described by a Vogel-Fulcher-Tammann (VFT, see chapter 2) behavior and the process at shorter relaxation times (red line) follows an Arrhenius dependence.

Upon decreasing temperature, the higher and higher correlation between the molecules leads to a dramatic increase in the timescale of the dynamic transitions. The characteristic relaxation time for typical glass-forming materials, are not thermally activated close to the glass transition; rather, a non-Arrhenius (Vogel-Fulcher-Tammann) behavior describes their dynamics (Figure 1.3) (see chapter 2).[34,35]

1.2 Conduction mechanisms in disordered solids

The charge conduction in molecular solids can be either electronic (more often) or ionic in nature. Both in the case that the conduction takes place via electrons or ions, in molecular systems the microscopic mechanism by which it occurs is the hopping of charge carriers between one site to the next (in organic molecular materials electrons tend to be localized on single molecules, see below). In the case of electron hopping or proton shuttling, the sites are individual molecules, while for small-ion diffusion the sites are empty interstices in the organic matrix.

In crystalline inorganic solids electrons form delocalized states giving rise to band transport. The charge transport in these ordered solids is hindered by the lattice vibrations and since the vibrations are minimized at low temperatures, the mobility of the charge carriers, and so the conductivity, increases by decreasing the temperature. This charge transport mechanism is not valid for organic molecular solids. The electronic coupling between molecules is much weaker than intramolecular covalent bonds; this favors the localization of electrons on single molecules, localization that is helped by intra-molecular electron-phonon coupling effects, inter-electronic repulsion, disorder, or presence of impurities acting as electron or hole 'traps'. The resulting localization of the electrons on single molecules implies that in order to participate to conduction processes, these charges have to hop out from one molecule to the next. The lattice vibrations mediate for hopping charge transport, and thus, this type of conduction is phonon-assisted and the conductivity increases with increasing temperature.[36]

Most organic molecular solids behave as insulating or disordered semiconductors, with electrical conduction stemming mainly from the electrons/holes charge transport. In some cases, cations or protons, if present either as constituents or as impurities, can also contribute and even dominate the overall charge transport.[36,37] In some cases, proton conduction in molecular systems can be the result of the presence of water, for example in hydrates, aqueous mixtures and hygroscopic salts (see section 1.4).

In many organic or disordered materials, the direct-current electrical conductivity σ_{dc} due to hopping conduction follows at least approximately a thermally activated behavior similar to Eq, 1.1, but with a different activation energy (C_A):

$$\sigma_{dc} \propto e^{-\frac{C_A}{k_B T}} \quad [1.2]$$

The minus sign takes into account the fact that σ_{dc} increases with increasing temperature. In the case of electronic conduction, which is the main intrinsic conduction mechanism in molecular solids, σ_{dc} deviates from the Arrhenius behavior of Eq. 1.2 in that its plot as a function of the inverse temperature appears to have a slightly positive curvature. The direct-current (dc) conductivity due to electronic charge carriers follows a dependence of the form $\log(\sigma_{dc}) = A - \frac{B}{T^n}$ [38,39,40] (Figure 1.4 (a)). A value of the power n close to the value of ½ or ¼ is usually found, which corresponds to a particular case of hopping conductivity known as variable-range hopping electronic conductivity.[39] [The non-Arrhenius temperature dependence of the conductivity can be visualized from the plot of the "effective activation energy" defined as the first derivative of the dc conductivity plot.[41] (Figure 1.4 (b)) Ion conductors display a large variety of temperature-dependencies, from simply-activated Arrhenius behavior[35] to non-Arrhenius with negative curvature.[42]

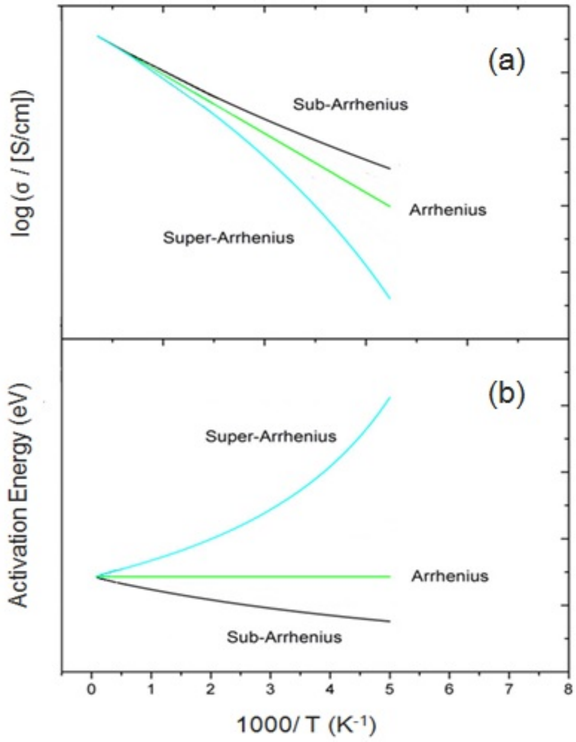

Figure 1.4 Schematic representation of the Arrhenius plot for the dc conductivity (σ_{dc}) (a) and its respective activation energy (b).

1.3 Water inside molecular solids

Water is the major component of life. Understanding the structure and the molecular dynamics of water in organic systems is of uttermost importance to the investigation of macromolecular function in cellular and other biochemical systems.[11] Confined and hydration water is also of importance for several other contexts, ranging from the study of food texture and quality,[4,7] to the stability of biotechnology products and pharmaceutical.[9]

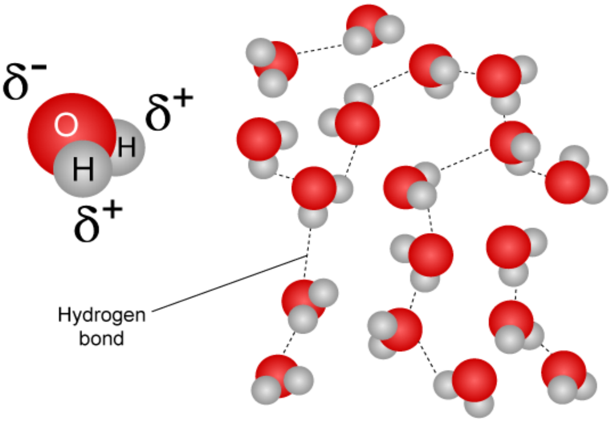

Figure 1.5 The water dipole and the (dynamically disordered) hydrogen bond network between water molecules.[43]

In the liquid phase of pure water, at a given time each water molecule is bonded to 3 or 4 other water molecules by means of directional hydrogen bonds (Figure 1.4). The molecules are constantly moving with respect to each other, and the hydrogen bonds are continually breaking and reforming.[44] Upon lowering the temperature, crystalline water is formed. Each oxygen atom is located at the center of a tetrahedron formed by four other oxygen atoms. Unlike the ordered oxygen atoms, the hydrogen atoms are randomly arranged within the crystal, a disorder that gives rise to a relaxation process.[45] In the solid state, water forms more than 15 crystalline phases as a function of pressure, among which the common hexagonal ice forming at ambient pressure.

While pure water undergoes crystallization into ice, which entails a halt to the translational and rotational motions of the H_2O molecules, water confined in micro- and nano-structured materials as well as many aqueous mixtures with hydrophilic solutes, polymers or biomolecules, can be supercooled into a state in which molecular motions persist and can be probed over a large temperature range well below the crystallization point of pure water. The dynamics of hydration water and of water confined inside porous or layered systems has been the subject of intense research in recent years.[46,47,48] Despite the differences between all studied systems (in terms of structure, topology etc), the relaxation times of water have always the same order of magnitude and similar activation energy. In particular, at low temperatures a simply activated relaxation (obeying Eq. 1.1) is observed in most hydrated systems, with activation energy of ~0.5 eV.[48]

Water molecules adsorbed onto the surfaces of insulating and semiconducting materials are able to interact strongly or weakly with the material. As mentioned in the preceding section, such hydration water can contribute to the charge transport mechanisms of the material by increasing the overall conductivity by several orders of magnitude,[49] even simply in the case of water vapor adsorbed onto the surface of the material from the surrounding atmosphere. The effect of adsorbed water has been be tested by measuring the conductivity as a function of the relative humidity.[50] Exposure of poorly conducting materials (insulating and semiconducting) to humid air introduces new mechanisms for charge generation and transport, which may result in an increase of the overall conductivity by several orders of magnitude.[51] The enhancement of the charge transport in these materials, which occurs at low-temperatures, is considered to be dominated by surface conduction, a mechanism which is the base of humidity sensors. The exact origin of the conductivity mechanism induced by water molecules is debated, but the most likely candidate is proton exchange in the hydrogen-bonded network.[52]

1.4 Outline of the thesis

This thesis focuses on the molecular dynamics and relaxation processes of small dipolar molecules hosted inside organic matrices or at their surfaces. Four different molecular systems are studied. Chapter 2 gives an introduction to the theoretical concepts of the dielectric relaxation processes, while chapter 3 provides information about the experimental techniques and the models used for the acquisition and analysis of experimental data. The presentation, analysis and discussion of the obtained results are presented in the following four chapters (one for each organic solid under scrutiny). Chapter 4 deals with the solid crystalline powder of an organic dye of the rhodamine family (Rh6G), which is slightly hygroscopic and has relatively low water content. The material displays several water-related relaxations, as well as an intrinsic relaxation due to an orientational molecular dynamic process of the Rh6G molecules themselves. The remaining three result chapters deal with fullerene systems. Chapter 5 deals with the well-known polyhydroxylated C_{60} derivative known as fullerenol. This material, which has a much higher water content than Rh6G, exhibits, beside some relaxations due to hydration water present on the surfaces of the fullerenol grains, also dynamic features typical of bulk ice. When hydrated, both Rh6G and fullerenol exhibit a direct-current conductivity dominated by water-induced (protonic) charge transport. Another polyfunctionalized C_{60} derivative, containing both hydroxyl and carbonyl side-adducts as well as epoxy oxygens, is described in chapter 6. Due to its variety of oxygen-containing groups, a strong hydrogen-bond network is formed leading to an ordered structure without molecular motions. Upon increasing temperature, the hydrogen-bond network is broken and interesting orientational phase transitions to more disordered phases occur. This behavior is reminiscent of order-disorder transitions in pure fullerite. The last chapter on experimental results (chapter 7) deals with the stoichiometric binary co-crystal of C_{60} with trichloroethane, in which both C_{60} and the guest-molecule appear to display dynamic disorder. The relaxation dynamics observed in this organic co-crystal are associated with the reorientational motions of the dipolar guest molecules. Due to the interference of the C_{60} cages acting as highly polarizable spacers, the molecular dynamics of the 1,1,2-trichloroethane guests are local, almost non-cooperative. In the last part the general conclusions of the thesis are presented.

Bibliography

[1] P.W. Anderson *Science*, vol. 267, p. 1615, 1995.

[2] P. Lunkenheimer, U. Schneider, R. Brand, A. Loidl *Contemporany Physics.,* vol. 41, p. 15, 2000.

[3] G. Niklasson. *Physics of disordered structures (Lecture notes)*. Uppsala University, Uppsala, 2011.

[4] J. Ubbink, A. Burbidge, R. Mezzenga *Soft Matter.*, vol. 4, p. 1569, 2008.

[5] G. Akovali, *Polymers in construction*. Rapra Technology Limited, Shawbury, UK, 2005.

[6] B. Zberg, P.J. Uggowitzer, J.F. Lo_er *Nature Mater.,* vol. 8, 2009.

[7] A. Hirte, C. Primo-Martína, M.B.J. Meinders, R.J. Hamer, *J. Cereal Sci.,* vol. 56, p. 289, 2012.

[8] J. Sjostrom, F. Kargl, F. Fernandez-Alonso, J. Swenson *J. Phys.: Condens. Matter.,* vol. 19, p. 415119, 2007.

[9] S.A. Luthra, E.Y. Shalaev, A. Medek, J. Hong, M.J. Pikal *J. Pharm. Sci.,* Vol. 101, p. 3110, 2012.

[10] P. Ball *Chem. Rev.,* vol. 108, p. 74, 2008.

[11] Y. Levy, J.N. Onuchic, *Annu. Rev. Biophys. Biomol. Struct*., vol. 35, p. 389, 2006.

[12] M. Zuriaga, L.C. Pardo, P. Lunkenheimer, J.L. Tamarit, N. Veglio, M. del Barrio, F.J. Bermejo, A. Loidl *Phys. Rev. Lett.,* vol. 103, p. 075701, 2009.

[13] A.I. Krivchikov, G.A. Vdovichenko, O.A. Korolyuk, F.J. Bermejo, L.C. Pardo, J.L. Tamarit, A. Jezowski, D. Szewczyk *J. Non-Cryst. Solids*., vol. 407, p. 141, 2015.

[14] M.J. Zuriaga, S.C. Perez, L.C. Pardo, J.L. Tamarit *J. Chem. Phys.,* vol. 137, p. 054506, 2012.

[15] I.V. Sharapova, A.I. Krivchikov, O.A. Korolyuk, A. Jezowski, M. Rovira-Esteva, J.L. Tamarit, L.C. Pardo, M.D. Ruiz-Martin, F.J. Bermejo *Phys. Rev. B.,* vol. 81, p. 094205, 2010.

[16] M. Zachariah, M. Romanini, P. Tripathi, J.L. Tamarit, R. Macovez *Phys. Chem. Chem. Phys.,* vol. 17, p. 16053, 2015.

[17] G.A. Vdovichenko, A.I. Krivchikov, O.A. Korolyuk, J.Ll. Tamarit, L.C. Pardo, M. Rovira-Esteva, F.J. Bermejo, M. Hassaine, M.A. Ramos *J. Chem. Phys.,* vol.143, p. 084510, 2015.

[18] S.C. Perez, M.J. Zuriaga, P. Serra, A. Wolfenson, P. Negrier, J.L. Tamarit, *J. Chem. Phys.,* vol.143, p. 134502, 2015.

[19] Ph. Negrier, M. del Barrio, J.L. Tamarit, D. Polymorphism *J. Phys. Chem. B.,* vol. 118, p. 9595, 2014.

[20] R. Tycko, G Dabbagh, R.M. Fleming, R.C. Haddon, A.V. Makhija, S.M. Zahurak *Phys. Rev. Lett.,* vol. 67, p. 1886, 1991.

[21] W.I.F. David, R.M. Ibberson, J.C. Matthewman, K. Prassides, T.J.S. Dennis, J.P. Hare, H.W. Kroto, R. Taylor, D.R.M. Walton *Nature* vol. 353, p. 147, 1991.

[22] R. Brand, P. Lunkenheimer, and A. Loidl *J. Chem. Phys.,* vol. 116, p. 10386, 2002.

[23] M. Mehring, K.F. Their, F. Rachdi, T. de Swiet *Carbon vol.* 38, p. 1625, 2000.

[24] I.S. Neretin, Y.L. Slovokhotov *Russ. Chem. Rev.,* vol.73, p. 455, 2004.

[25] C. Meingast, G. Roth, L. Pintschovius, R.H. Michel, C. Stoermer, M.M. Kappes *Phys. Rev. B.,* vol. 54, p.124, 1996.

[26] M. Romanini, J.C. Martinez-Garcia, J.L. Tamarit, S.J. Rzoska, M. del Barrio, L.C. Pardo *J. Chem. Phys.,* vol. 131, p. 184504, 2009.

[27] A. Criado, M. Jiménez-Ruiz, C. Cabrillo, F.J. Bermejo, R. Fernández-Perea, H.E. Fischer, F.R. Trouw *Phys. Rev. B.,* vol. 6, p. 12082, 2000.

[28] M. Zachariah, M. Romanini, P. Tripathi, J.L. Tamarit, R. Macovez *Phys. Chem. Chem. Phys.,* vol. 17, p. 16053, 2015.

[29] Ph. Negrier M. Barrio , J. Ll. Tamarit, D. Mondieig, M. J. Zuriaga, and S. C. Perez *Cryst. Growth Des*., vol. 13, p. 2143, 2013.

[30] R. Puertas, M.A. Rute, J. Salud, D.O. López, S. Diez, J.C. Van Miltenburg, L.C. Pardo, J.L. Tamarit, M. del Barrio, M.A. Pérez-Jubindo *Phys*. *Rev*. *B.,* vol. 69, p. 224202, 2004.

[31] D.A. Dunmur, M.R. de la Fuente, M.A. Perez Jubindo, S. Diez *Liq*. *Cryst.,* vol. 37, p. 723, 2010.

[32] C.M. Roland *Soft Matter.,* vol. 4, p. 2316, 2008.

[33] K.L. Ngai, M.J. Paluch *Chem. Phys.,* vol. 120, p. 246, 2004.

[34] F. Kremer, A. Schönhals *Broadband Dielectric Spectroscopy.* Berlin: Springer, 2002.

[35] C.J.F. Bottcher *Theory of electric polarization.,* vol. I. Dielectrics in static fields. Amsterdam, Oxford, New York: Elsevier, 1973.

[36] W. Brutting, Ch. Adachi *In Physics of Organic Semiconductors, 2nd ed*.; Wiley: Chichester, 2012.

[37] M. Riccò, M. Belli, M. Mazzani, D. Pontiroli, D. Quintavalle, A. Janossy, G. Csanyi *Phys*. *Rev*. *Lett*., vol.102, p. 145901, 2009.

[38] A.K. Jonscher *Nature vol.* 267, p. 673, 1977.

[39] M.P.J. van Staveren, H.B. Brom, L.J. de Jongh *Phys. Rep.,* vol. 208, p. 1, 1991.

[40] D. Yu, C. Wang, B.L. Wehrenberg, P. Guyot-Sionnest *Phys. Rev. Lett.,* vol. 92, p. 216802, 2004.

[41] H. Han, C. Davis, III, J.C. Nino *J. Phys. Chem. C.,* vol. 118, p. 9137, 2014.

[42] J. Kincs, S.W. Martin *Phys. Rev. Lett.*, vol. 76, p. 70, 1996.

[43] *http://www.lsbu.ac.uk/water/*

[44] J.D. Smith, C.D. Cappa, K.R. Wilson, R.C. Cohen, P.L. Geissler, R.J. SaykallyProc. *Natl. Acad. Sci.,* U. S. A. vol. 102, p.14171, 2005.

[45] Popov, A. Puzenko, A. Khamzinb, Y. Feldman *Phys. Chem. Chem. Phys.,* vol. 17, p. 1489, 2015.

[46] Y. Zhang, M. Lag, F. Ridi, E. Fratini, P. Baglioni, E. Mamontov S.H. Chen *J. Phys. Condens. Matter.,* vol. 20, p. 502101, 2008.

[47] S. Cerveny, F. Barroso-Bujans, Á. Alegría, J. Colmenero *J. Phys. Chem. C.,* vol. 114, p. 2604, 2010.

[48] J. Swenson, S. Cerveny *J. Phys.: Condens. Matter.,* vol. 27, p. 033102, 2015.

[49] J. Anderson, G.A. Parks *J. Phys. Chem.,* vol. 72, p. 3662, 1968.

[50] C. Cramer, S. De, M. Schönhoff *Phys. Rev. Lett.*, vol.107, p. 028301, 2011.

[51] H. Haspel, V. Bugris, Á. Kukovecz *J. Phys. Chem.,* vol. 117, p.16686, 2013.

[52] C. Knight, G.A. Voth *J. Phys. Chem.,* vol. 45, p. 101, 2012.

Chapter 2

DIELECTRIC RELAXATIONS AND CONDUCTIVITY CONTRIBUTIONS IN SOLIDS

2.1 Introduction

Dielectric phenomena are described by Maxwell's theory of electrodynamics, which depicts the interaction of electromagnetic fields with matter,[1,2] and by the contributive work of other scientists of his era, such as Faraday, Mossotti, and Debye. The term "dielectric" was introduced in the 19th century by Michael Faraday, who also introduced the concept of dielectric constant to describe the response of such materials to an applied electric field. There are various textbooks describing the connection between macroscopic dielectric phenomena with the microscopic nature of materials.[3,4,5] Faraday[6] argued that the storage capacity (*capacitance*) of a capacitor can be enhanced by inserting a medium between two parallel conducting plates. The intervening medium is a dielectric material, namely, an electrical insulator which can be *polarized* by the application of an electric field.

From a macroscopic point of view, when an electric field is applied across an empty capacitor it results the storage of positive charge in one plate and the storage of negative charge in the other one. By defining the empty capacitance $\mathrm{C_0}$ (capacitance of the empty capacitor) as:

$$C_0 = \frac{Q_0}{V} \qquad [2.1]$$

where $\mathrm{Q_0}$ is the stored charge of the empty capacitor and V is the applied voltage, it is found that by inserting a dielectric material into the capacitor the value of capacitance increases to a new value *C* due to the “neutralization” of some free charges on the metal plates due to the induced polarization charge in the dielectric, thus allowing the storage of additional charge. The ratio of capacitance between the filled and empty capacitor,

$$\varepsilon_r = \frac{C}{C_0} \qquad [2.2]$$

depends only on the dielectric material, and is known as the relative electric permittivity or dielectric constant of the material. The electric permittivity expresses how the dielectric affects and is affected by the applied electric field. An important characterization technique, which is used widely to study experimentally dielectric phenomena, is Broadband Dielectric Spectroscopy.[3] Dielectric measurements provide information about the static and frequency-dependent permittivity, as well as about relaxation phenomena related to molecular motions and fluctuations of the material’s dipoles, and also about the motion of charge carriers under an applied electric field.

In this chapter, we introduce the theoretical concepts of dielectrics and their response to external electric fields, both from a macroscopic and microscopic perspective. We deal also with conductivity contributions to the dielectric response due to the motion of charge carriers. Finally, we discuss the different relaxation processes taking place within dielectrics, such as the secondary relaxations or the cooperative relaxation process related with the glass transition in amorphous or disordered dielectrics.[7,8]

2.2 Dielectrics in electric fields

When a voltage is applied across a capacitor filled with a dielectric material, the material becomes *polarized*, which means that its constituent (bound) charges are displaced in the direction of the field, perturbing the neutral distribution within the material. For a low applied electric field (field strength < 10^6 $\mathrm{Vm^{-1}}$) and for an isotropic and homogeneous system, the polarization (P) of the dielectric material is linearly proportional to the macroscopic (average) electric field in the dielectric, E.

$$P = (\varepsilon_r - 1)\varepsilon_0 E = \chi_e \varepsilon_0 E \qquad [2.3]$$

where ε_0 is the vacuum electric permittivity $\varepsilon_0 = 8.854 \cdot 10^{-12}\ \mathrm{Fm^{-1}}$, and χ_e is the electric susceptibility of the dielectric, which expresses the degree of the dielectric polarization in response to an applied field.[9,10] The polarization P of the dielectric is defined as the average dipole moment per unit volume, and can be written as the product of the molecular (induced) dipole moment (μ) with the molecular density $(\frac{\mathrm{N}}{\mathrm{V}})$:[11]

$$P = \frac{N}{V}\mu \qquad [2.4]$$

While the polarization (P) is related to the charge density on the surface of the dielectric material (bound charge), another magnitude D is introduced to take into account the free charges in the dielectric and the charge on the capacitor´s plates. The vector magnitude D is called the electric displacement field and is defined as $D = \varepsilon_0 E + P$. Thus, for a linear dielectric medium one has:

$$D = \varepsilon_0 \, E + P = (1 + \chi_e) \, \varepsilon_0 \, E = \varepsilon_r \, \varepsilon_0 \, E \qquad [2.5]$$

where ε_r is the relative permittivity of the medium. Equations 2.3 and 2.5 are called linear constitutive equations of the dielectric.[12] The magnitudes ε_r and χ_e are related as $\chi_e = \varepsilon_r - 1$, and they are dimensionless and material dependent. It is useful to further develop the linear constitutive equations for the static[10] and time-dependent cases.[13] In static electric field the constitutive equation [2.5] becomes:

$$D = \varepsilon_s \varepsilon_0 E \quad [2.6]$$

where ε_s is the static relative permittivity. When a time-dependent field is applied, E(t), the material will respond linearly with the field obeying a more general equation, whose frequency dependence (Fourier transform) can be written as:

$$D(\omega) = \varepsilon^*(\omega) \varepsilon_0 E(\omega) \qquad [2.7]$$

$$P(\omega) = (\varepsilon^*(\omega) - 1) \varepsilon_0 E \quad [2.8]$$

where ω, is the angular frequency ($\omega = 2\pi f$) of the field. The response of the material is characterized by linearity[9] and causality, the latter imposing a temporal delay between the field and the material´s polarization (i.e., the displacement field, or equivalently the material´s polarization, arises after the application of the electric field). The delay in the polarization of the dielectric medium with respect the time-varying electric field gives the *dielectric relaxation*.[13,14] The factor $\varepsilon^*(\omega)$ is the complex dielectric permittivity or complex dielectric function, which contains information about the amplitudes and the phase difference between the electric field (disturbance) and the material´s displacement field and polarization (response). The frequency dependent complex dielectric permittivity $\varepsilon^*(\omega)$ is written as:

$$\varepsilon^*(\omega) = \varepsilon'(\omega) - i\varepsilon''(\omega) \quad [2.9]$$

The real part, $\varepsilon'(\omega)$, of the complex dielectric function is related to the electric energy stored in the material, and the imaginary part, $\varepsilon''(\omega)$, is associated with the dissipation (loss) of electric energy within the material due to the internal friction.[13] When plotted in logarithmic scale against log(ω), the graph of the imaginary part usually gives a peak whose maximum defines the characteristic relaxation time at a given temperature (Figure 2.1). From the loss peak it is possible to extract quantitative information about molecular dynamics and interactions. In correspondence with the loss peak, the real part displays a step like change whose height is related with the dielectric strength, $\Delta\varepsilon = \varepsilon_s - \varepsilon_\infty$, defined as the area under the loss peak. The term ε_∞ characterizes the high frequency response ($f > 10^9$ Hz) of the material, while the low frequency response ($\omega = 2\pi f \rightarrow 0$) is the static permittivity mentioned before.

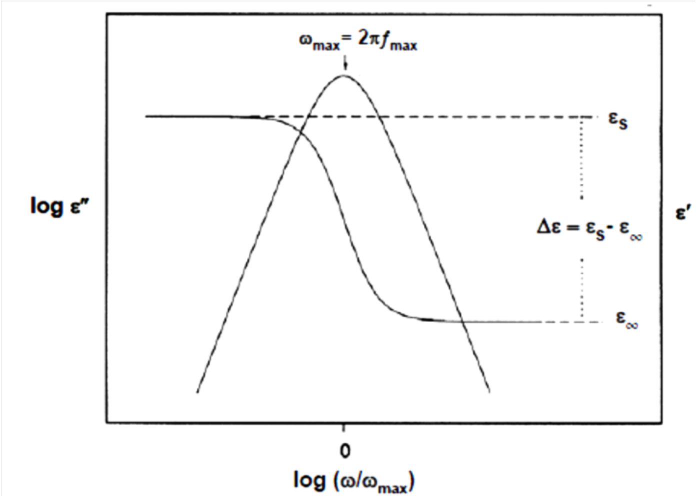

Figure 2.1 Real (right y-axis) and imaginary part (left y-axis) of the complex dielectric permittivity as a function of normalized angular frequency.

Causality leads to an inter-dependence between the real and the imaginary part of the complex function ε*(ω), which is described by the Kramers-Kronig relationships.[15,16]

$$\varepsilon'(\omega) = \varepsilon_\infty + \frac{2}{\pi}\int_0^\infty \varepsilon''(\omega') \frac{\omega'}{\omega'^2-\omega^2} d\omega' \quad [2.10]$$

$$\varepsilon''(\omega) = \frac{2}{\pi}\int_0^\infty \varepsilon'(\omega') \frac{\omega}{\omega'^2-\omega^2} d\omega' \quad [2.11]$$

The mutual dependence between both magnitudes can be useful for testing the existence of relaxation processes.

2.3 Polarization Mechanisms

A material can become polarized by different mechanisms depending on the type of the material and the moieties that undergo polarization.[17] (Figure 2.2)

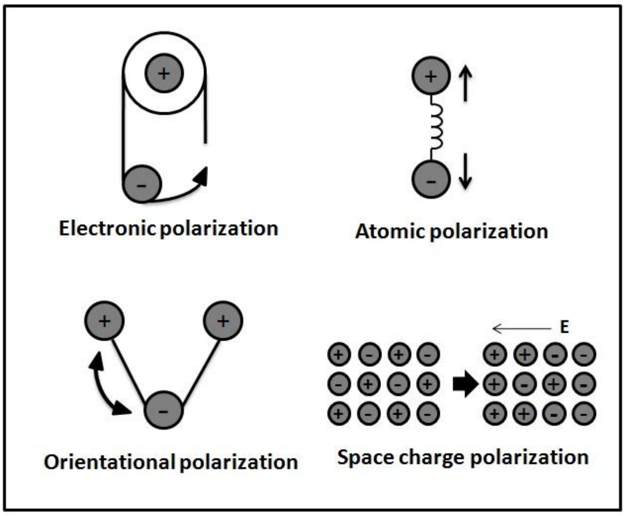

Figure 2.2 Representation of the four different mechanisms by which a dielectric material can become polarized under the application of an external electric field.

• Starting from the high frequency mechanisms, the most common type of polarization is the electronic polarization P_e; in a neutral atom or molecule the application of an electric field induces a displacement of the electronic cloud with respect to the atomic nucleus, resulting in an induced dipole moment due to electron displacement. It takes place on a time scale of 10^{-15} sec, i.e. in the visible part of the electromagnetic spectrum, because of the low mass of the electrons, which can readily move under the application of an electric field.

• At slightly lower frequencies (longer time scale), another type of polarization mechanism occurs; atomic polarization P_a is the displacement of different atoms/ions inside the molecule or solid. By the application of an electric field, oppositely charged atoms (ions or atoms participating in partially ionic covalent bonds) will move in opposite directions, resulting in a stretching of the inter-atomic bonds and in a distortion of the arrangement of the atoms within a molecule. Atomic polarization has a weaker contribution to the overall polarization of a material compared to the electronic one, except in ionic compounds. It takes place on a typical time scale of 10^{-12} sec, the timescale of atomic vibrations, i.e. in the IR range.

- The polarization mechanism which occurs at radiofrequencies is due to the motion of heavier moieties, namely permanent molecular dipoles. Orientational polarization P_o results from the rotational or rototranslational motion of the material´s permanent dipoles. This occurs because permanent dipole moments that can rotate tend to align themselves parallel to the applied field direction, giving a net polarization within the material; when this happens the dipoles are said to ´relax´ under the applied field.
- Another polarization mechanism, which takes place at yet lower frequencies than the previous one, is the space-charge (interfacial) polarization P_{sc} it originates from the macroscopic migration of charge carriers and their trapping at grain boundaries, interfacial sites and other material defects. This type of polarization is not intrinsic to a material but rather originates from the heterogeneity of each sample. Due to its low frequency and spectral shape, it can be misinterpreted as a dynamical behavior (orientational relaxation) intrinsic to the material.

The total polarization (Figure 2.2) of a dielectric sample is in general the sum of all four contributions:

$$P_{total} = P_e + P_a + P_o + P_{sc} \qquad [2.12]$$

When applying a static electric field, all the different polarization mechanisms can contribute to the total polarization. Upon turning on the applied field, the polarization contributions due to induced dipoles (electronic, atomic) take place almost instantaneously (short times), while the orientational one requires longer times, which means that it needs more time to respond to the external field. The different contributions to the total polarization can be distinguished by performing either time-resolved or frequency-dependent measurements, as each contribution is visible in different frequency ranges, as shown in Figure 2.3.

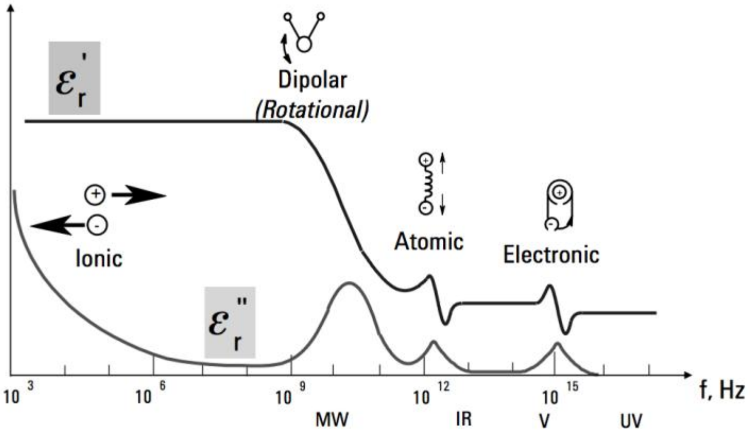

Figure 2.3 Representation of all the different polarization mechanisms in both real and imaginary part of the complex dielectric permittivity as a function of frequency. By “ionic” processes we indicate both the dc conductivity contribution from free carriers and space-charge relaxations.

In non-polar materials, where permanent dipoles are absent, the macroscopic polarization only results from the contribution of induced dipoles. The resulting polarization is described by the theory of Lorenz[18], Mossotti[19] and Clausius.[20] Mossotti and Clausius have correlated the macroscopic polarization with the induced microscopic dipoles, establishing the following relation:

$$\frac{\varepsilon_r - 1}{\varepsilon_r + 2} = \frac{N}{V}\frac{1}{3\varepsilon_0}\alpha_{ind} \quad [2.13]$$

Here, $\frac{N}{V}$ is the volume number density of the dipoles, α is the molecular polarizability, which represents the ability of a molecule (or atom) to become polarized under an applied field, and ε_r is the relative electric permittivity. At the beginning of 20th century Debye generalized this result by including also the case of permanent dipoles, i.e., the effect of orientational polarization. Since, as discussed above, the polarization due to induced (rather than permanent) dipoles (α_{ind}) is established much more rapidly than the orientational one, therefore we use for them the symbols of P_∞ and ε_∞ (corresponding to an "infinite" frequency; in reality the value ε_∞ of the permittivity, which includes the contribution of electronic and atomic polarization, is already reached at 10^{10} Hz). By using statistical physics, Debye established his formula for the static (low frequency) permittivity taking into account both induced and permanent dipoles of magnitude μ:

$$\frac{\varepsilon_s - 1}{\varepsilon_s + 2} = \frac{N}{V}\frac{1}{3\varepsilon_0}\left(\alpha_{ind} + \frac{\mu^2}{3\,k_B\,T}\right) \qquad [2.14]$$

By using equation 2.13 with the notation $\varepsilon_r = \varepsilon_\infty$, this gives:

$$\frac{\varepsilon_s - 1}{\varepsilon_s + 2} - \frac{\varepsilon_\infty - 1}{\varepsilon_\infty + 2} = \frac{N}{V}\frac{\mu^2}{9\varepsilon_0 k_B T} \qquad [2.15]$$

Debye's addition to the Clausius-Mossotti formula assumes non-interacting permanent dipoles, i.e., it is valid for systems where the interactions between dipoles are negligible, such as dipolar gases and some dipolar, non-associating, liquids. This theory is hardly applicable directly to real dipolar materials (i.e., materials containing permanent dipoles), since their permanent dipoles are expected to interact through dipolar interactions and also by steric hindrance between neighboring molecules. For this case, Debye´s formula needs to be generalized. A first modification in this sense was introduced by Onsager[21], according to whom:

$$\varepsilon_S - \varepsilon_\infty = \frac{1}{3\varepsilon_0} \frac{\varepsilon_S\,(\varepsilon_\infty + 2)^2}{3\,(2\,\varepsilon_S + \varepsilon_\infty)} \frac{\mu^2}{k_B\,T}\,\frac{N}{V} \qquad [2.16]$$

In this equation, μ^2 is the mean square dipole moment for non-interacting dipoles, ε_s is the static electric permittivity (including the contribution of the permanent dipoles) and the ε_∞ concerns only the induced dipoles, as discussed. The quantity $\varepsilon_s - \varepsilon_\infty$ is the dielectric strength of the dipolar relaxation, as we have mentioned in the previous section. The orientational polarization due to the motion of permanent dipoles usually decreases upon heating since the tendency of the dipoles to align themselves parallel to the applied field is disturbed by their thermal motions, fact which is in contrast to induced polarizations (electronic and atomic), which is a priori not temperature-dependent. Onsager's formula was later modified by Fröhlich[5] and Kirkwood[22,23,24], who introduced an extra factor in Onsager formula, namely the correlation factor g_K describing the degree of correlation between orientations and positions of neighboring dipoles:

$$\Delta\varepsilon = \varepsilon_S - \varepsilon_\infty = \frac{1}{3\varepsilon_0} \frac{\varepsilon_S\,(\varepsilon_\infty + 2)^2}{3\,(2\,\varepsilon_S + \varepsilon_\infty)}\, g_K \frac{\mu^2}{k_B\,T}\,\frac{N}{V} \; [2.17]$$

If only first neighbor dipoles are considered, g_K is given by:

$$g_K = 1 + z < cos\,\gamma > \qquad [2.18]$$

where z is the number of neighbors surrounding a given dipole, γ is the angle between two next-neighbor dipoles and brackets denote the time average. From the last formula we see that for non-interacting dipoles, g_K is equal to 1. In practice g_K is very difficult to calculate theoretically, but it can be estimated from the experimental value of the dielectric strength using equation 2.17.

2.4 Charge-Transport Mechanisms and related dielectric losses

In the molecular solids studied in this thesis, charge conduction can be either electronic or ionic in nature. While in crystalline inorganic solids electrons form delocalized states giving rise to band transport, in molecular solids electrons are localized on single molecules, and may only move by means of “hop” processes from one molecule to the next. Therefore, both in the case that the conduction takes place via electrons or ions, in molecular systems the microscopic mechanism by which it occurs is the hopping of charge carriers between one site to the next (in the case of electron hopping or proton shuttling, the sites are individual molecules, while for small-ion diffusion the sites are empty interstices in the organic matrix).

In a dielectric spectrum, besides the polarization processes, it is common to observe contributions stemming from charge transport within the material, especially at low frequency and high enough temperature. The most obvious contribution to the loss spectrum is the low-frequency increase originating from the long-range percolation conductivity (dc conductivity) through the sample. Additional conductivity contributions to the loss spectra originate from charge accumulation processes, which are due to the blocking of the charges at grain boundaries or at the electrode surfaces.

The motion of the free charges causes conduction currents; the current density, j, in a material undergoing a periodic field is given by Ohm´s law, $j = \sigma E$, where σ is the (real) dc conductivity. The Ampere-

Maxwell law shows that the time derivative of the displacement current, $\partial D/\partial t = i\omega\varepsilon_r\varepsilon_0 E$, is equivalent to a current density, in that it is a source of magnetic fields just as the latter. Hence one may write a total current density as $J = +j_{displacement} = \sigma E + i\omega\varepsilon_r\varepsilon_0 E$. By generalization of Ohm's law, then, a complex conductivity is defined, related to the complex permittivity as:[3]

$$\sigma^*(\omega) = \sigma'(\omega) + i\sigma''(\omega) = i\omega\varepsilon_0\varepsilon^*(\omega) \qquad [2.19]$$

The complex conductivity is composed by a real and an imaginary part, related to the real and imaginary parts of the complex permittivity as

$$\sigma'(\omega) = \omega\varepsilon_0\varepsilon''(\omega) \text{ and } \sigma''(\omega) = \omega\varepsilon_0\varepsilon'(\omega) \quad [2.20]$$

Correspondingly, to describe the contribution of the dc conductivity to the dielectric data, it is customary to add the following complex permittivity contribution to the total permittivity:

$$\varepsilon_{\sigma(dc)}{}^*(\omega) = -i\left(\frac{\sigma_0}{\varepsilon_0\omega}\right)^s \qquad [2.21]$$

where $\left(\frac{\sigma_0}{\varepsilon_0\omega}\right)^s$ is the additional loss term due to dc charge conduction (Joule effect).[25] If the conductivity is ohmic, the exponent s is equal to one, implying a linear increase, with slope≈1 in logarithmic representation, of the low frequency part of the loss spectra upon decreasing frequency. There is no contribution due to the dc conductivity to the real part of permittivity (see Figure 2.4 (a)). In practice the slope is not equal to one due to non-ohmic contributions to the conductivity. In such case, σ_0 is not the dc limit of the conductivity but only a fit parameter (not shown).

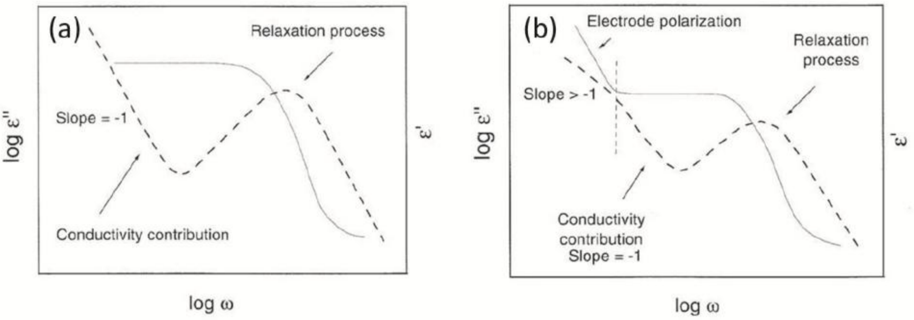

Figure 2.4 Typical dielectric spectra of the logarithm of the real ε'(ω) (solid line) and imaginary ε''(ω) (dashed line) part of the complex permittivity for a relaxation process and an ohmic conductivity contribution (a). In panel (b), a typical spectrum displaying the effect of electrode polarization is described.

The other contributions to the dielectric response are interfacial polarization/space-charge mechanisms. The interfacial polarization mechanism is the result of the blocking of charge carriers either at the electrode-dielectric interface, i.e. at a macroscopic level (electrode polarization effect), or at grain boundaries inside an inhomogeneous material i.e. at the mesoscopic level (Maxwell-Wagner-Sillars polarization). Their signature is a steep increase of the real part of the permittivity as the frequency is lowered, while in the dielectric loss there is a bending in the conductivity contribution which in some cases resembles a dipolar loss feature.

Electrode polarization (EP)[3,26] is caused by the mobile charge carriers that cannot cross the electrodes, and thus build up a charge layer at the electrode-sample interface when a slowly varying electric field is applied. As a result, the conductivity becomes lower and lower at low frequency, and the low-frequency imaginary part of the permittivity deviates from its initial slope (Figure 2.4(b)). In order to describe the EP effect, one can use a simple model of a double layer arrangement to characterize the blocking of charges at the interface. According to the model each layer characterizes a surface with different dielectric properties. From this model the time dependence of electrode polarization effect can be calculated, which originates from the continuous charging and discharging of the double layer, as:

$$\tau_{EP} \approx \frac{\varepsilon_S\, \varepsilon_0}{\sigma_0} \frac{D}{2\, L_D} \text{, for } D >> L_D \qquad [2.22]$$

Here L_D is the Debye length characterizing the effective spacing between the electrodes and the sample, and D is the thickness of the sample. From equation 2.22, one can understand that, by increasing the dc conductivity of the sample, the EP effect shifts to higher frequencies. On the other hand by measuring thicker samples, the EP contribution shifts to lower frequencies. Hence by modifying the experimental geometry (e.g. by changing electrodes´ material, sample temperature, or sample thickness), the EP contribution can be identified in the frequency dependent dielectric response. In general, correcting the EP effect from the dielectric data it is not an easy process.[27]

In order to visualize and describe these contributions, a different representation from the complex permittivity can be used. We will employ the real conductivity representation (Figure 2.5), where the long-range percolation (dc) conductivity is visible as a horizontal plateau at low frequency, and the electrode polarization is seen as a characteristic bending at yet lower frequencies (Figure 2.6(a)). Another useful representation is the complex electric modulus, defined as $M(\omega) = \frac{1}{\varepsilon(\omega)}$, which is not employed in this thesis.

As mentioned before, charge conduction in disordered solids (whether electronic or ionic) occurs via a hopping mechanism. In all these systems the real part of the complex conductivity (σ´) exhibits at least two regimes, one at low frequency, and the other at higher frequency. At low frequencies, σ´ is approximately constant, i.e. a horizontal plateau is seen. As mentioned, this plateau corresponds to charge carriers able to move across a percolation network that extends across the whole sample (correlated dc hopping).

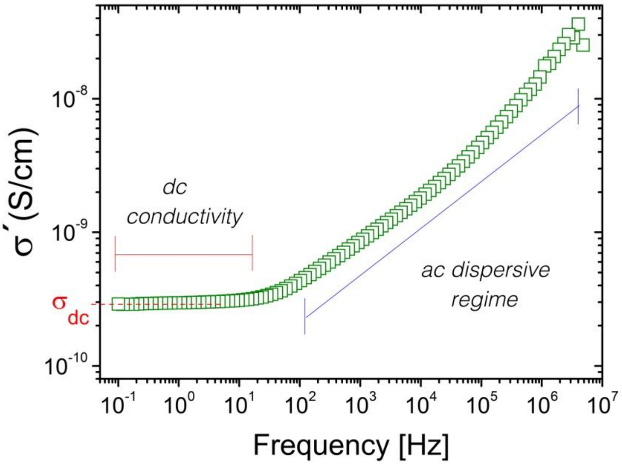

Figure 2.5 Logarithmic spectrum of the real part of the conductivity, displaying a dc conductivity plateau at low frequencies and the dispersive regime at higher frequencies.

As it can be seen in Figure 2.5, the σ_{dc} value can be obtained readily by the low frequency plateau. In the case of a divergence of the low-frequency plateau due to the pronounced electrode polarization effect, the minimum of the first derivative $(\frac{d\sigma'}{df})$ can be used to define the frequency f_0 where the value of σ_{dc} should be determined as $\sigma_{dc} = \sigma'(f_0)$. The high-frequency regime is instead dispersive, with σ´

increasing with increasing frequency (Figure 2.5). This behavior is called "universal dielectric response" and it was introduced first by Jonscher, who demonstrated that the ac conductivity response of disordered systems increase with increasing frequency, following a ´universal´ power-law; $\sigma'(\omega) \propto \omega^{n}$, with n between 0.6 and 1.0.[28]

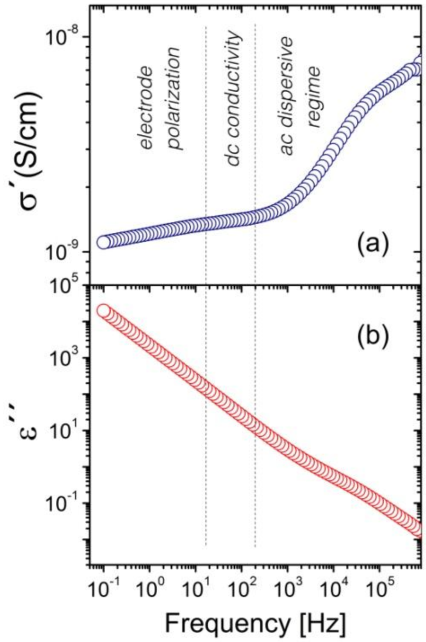

Figure 2.6 The real part of the conductivity (a) and the dielectric loss (b), displaying, from low to high frequency, an electrode polarization effect, a dc conductivity plateau and a dispersive regime. The onset of the ac dispersion regime is here associated with a loss peak in the dielectric loss spectrum.

While in some disordered conductors the universal response is visible as a smooth increase resulting in a simple power law, other materials exhibits a bump-like feature, visible as a broad loss feature in the imaginary part of permittivity (Figure 2.6 (b)). The origin of such loss feature is that the dispersive region in the σ´ of disordered solids comes from charges moving in a restricted percolation range (e.g., within a single crystalline grain). The restricted hopping entails accumulation of charges (e.g. at grain boundaries) and thus polarization losses, known as space-charge relaxations. While a power law dispersive σ´ means a wide variety of restricted percolation ranges (and thus of characteristic relaxation times), the observation of a bump-like feature indicates the existence of a well-defined space-charge relaxation time, and therefore of a well-defined restricted percolation range. Such relaxation feature is called space-charge relaxation or sometimes Maxwell-Wagner-Sillars (MWS) relaxation, although the simple theory developed by these authors is not able to capture the features of all space-charge relaxations.

The MWS[29,30] or space-charge relaxation occurs in inhomogeneous systems like biological materials, phase-separated polymers, blends, crystalline or liquid crystalline polymers, polycrystalline materials.[31,32] It is due to the accumulation of the charge carriers at the grain boundaries, and it is more pronounced in more conductive materials. In order to describe this contribution in an inhomogeneous material, the model of the double layer arrangement can be used. Molecular models to describe interfacial conductivity effects were developed by Maxwell[33]and improved by Wagner[34] and Sillars.[35] For the MW relaxation, the model predicts a Debye-like frequency dependent feature in the dielectric function:

$$\tilde{\varepsilon}^*(\omega) = \varepsilon_\infty + \frac{\Delta\tilde{\varepsilon}}{1 + i\omega\tau_{MW}} \quad [2.23]$$

Space-charge relaxations do not, however, have to display a Debye profile. A more general relation has been shown to apply to many space-charge processes, known as Barton-Nakajima-Namikawa (BNN) condition. According to the BNN relation, the frequency position (f_{max}) of the loss features appearing at the onset of the ac dispersive region (Figure 2.6), fulfills the following equation:

$$\sigma_{dc} = p\,\Delta\varepsilon\,\varepsilon_0\,f_{max} \quad [2.24]$$

where p is a numerical constant of the order of unity, and $\Delta\varepsilon$ is the dielectric strength of the space-charge feature.[36] Because $\Delta\varepsilon$ is basically a constant quantity, the BNN relation implies a direct proportionality between f_{max} and the dc value of the conductivity.[37] The BNN relation holds if the same charge conduction process dominates both the dispersive regime and the long-range (dc) conductivity.

A useful quantity which stems from the BNN relationship is the characteristic relaxation frequency (f_σ) of spatial charge fluctuations in conducting media:

$$f_\sigma = \frac{\sigma_{dc}}{2\pi\varepsilon_0\Delta\varepsilon} \qquad [2.25]$$

Such space-charge frequency is a scaling frequency which is constructed from aspects of both dc conductivity (σ_{dc}) and the permittivity change ($\Delta\varepsilon$), and corresponds to the characteristic frequency of oscillation of charges in their restricted hopping range.[38]

2.5 Dielectric relaxation processes

Molecular solids display in general a wide range of structural phases, some of which are partially or fully disordered. The fully disordered phases are the isotropic liquid and the structural glass; among partially disordered phases, examples are liquid crystal phases, semi-crystalline polymer phases, plastic crystals, and orientationally disordered phases. The disorder can be static (as in a structural glass), or dynamic (as in a liquid). The transition from dynamic to static disorder, as a dynamically disordered phase is cooled down, is called glass transition, and it has similar features regardless of whether the initial disorder is complete, as in an isotropic liquid, or partial as in a plastic crystalline phase. In particular, just as structural glass-forming materials, molecular solids can display a cooperative ("primary") relaxation due to collective molecular motions, and less cooperative ("secondary") relaxation processes due to quasi-single-molecule motions or even to the motion of individual polar groups of the molecules.[3] In plastic-crystal phases[39,40] and in supercooled liquids[41,42] the former relaxation due to quasi-single-molecule motions is intrinsically associated with the glass transition process: the primary relaxation displays a continuous, dramatic slow-down (by several decades in a short temperature interval) upon approaching the glass transition temperature, which is defined as the temperature at which the primary relaxation reaches a characteristic time of 100 or 1000 seconds.[3,13] The slowing down of the orientational motions in a plastic crystal or an orientationally disordered crystal can lead to a glass-like transition, and the resulting phase is called "orientational glass".[43,44]

A typical spectrum of a material displaying both a primary (cooperative) and a secondary (local) relaxation is shown in Figure 2.7. The primary relaxation, called α relaxation process, is visible at lower frequency. The temperature dependence of the characteristic relaxation time of the α process usually deviates from a thermally activated behavior (Arrhenius), and follows instead a Vogel-Fulcher-Tammann (VFT) temperature dependence.[41,45]

$$\tau_\alpha\,(T) = \tau_0 e^{\frac{D\,T_{VF}}{T-T_{VF}}}\ [2.25]$$

Here, τ_0 is the high temperature limit of the relaxation times, describing the local orientational fluctuations occurring at very high thermal energies (usually $\tau_0 \approx 10^{-13}$ sec), T_{VF} is the Vogel-Fulcher temperature, which is lower than the glass transition temperature (T_g), and finally, D is the strength parameter.[46]

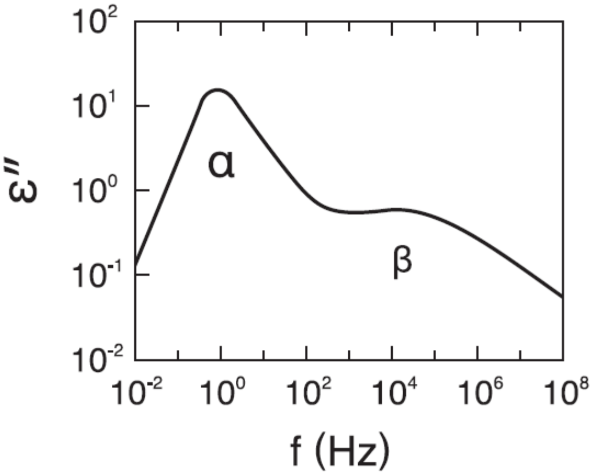

Figure 2.7 Representative spectrum of the frequency dependent dielectric loss of a typical dynamically disordered material. Two distinct dielectric features are depicted, namely a primary (α) relaxation and a secondary relaxation. Conductivity contributions are avoided for clarity.

The temperature dependence of the intensity and the broadening of the prominent loss peak are of importance. Normally, for typical glass formers, the intensity of the peak (dielectric strength) decreases upon heating, because dipolar interactions dominate its response. The additional thermal energy induces collisions between the molecules, resulting their deviation from their collective relaxation behavior temporally.

Weakly cooperative relaxation processes, called secondary relaxations, are also commonly present (at higher frequency) in the imaginary part of permittivity (Figure 2.7). The temperature dependence of secondary processes usually follows the Arrhenius equation:

$$\tau_\beta\,(T) = \tau_0 e^{\frac{E_A}{k_B T}} \quad [2.26]$$

where $\mathrm{E_A}$ is the activation energy and $\mathrm{k_B}$ is the Boltzmann constant. Equation 2.26 is typical for a thermally activated process, where the energy barrier $\mathrm{E_A}$ that the molecules need to overcome to relax, is temperature independent.[44,47] The dielectric strength of a relaxation process is defined as the area under the relaxation peak (or equivalently, as the height of the step in the real part of the permittivity, according to the Kramers-Kronig relations), and, as it can be gathered from Eq. 2.16 or 2.17, it is proportional with the number of the relaxing entities and to the square of their dipole moments. In general, secondary relaxation peaks are much less intense than the α-peak, which is visible, e.g. in figure 2.7, from the fact that the height of the secondary process in the loss spectrum is lower than that of α process.

Secondary relaxations are of two types: they are either intramolecular processes, which involve the motion of only a part of a larger molecule (e.g. a moiety containing polar groups), or they are whole-molecule processes (for example, they are observed in rigid molecules that have no moving subparts). This second, more controversial type of secondary relaxation, called Johari-Goldstein (JG) relaxation,[48,49] appears to be a whole-molecule dynamic process that, unlike the α process, is non-cooperative. It has been observed in many glass-forming materials,[50] in plastic crystals[51] and also in aqueous mixtures.[52] The width of the secondary Johari-Goldstein relaxation is usually significantly broader than that of the α peak.

A possible explanation of the origin of JG relaxation are so-called ´islands of mobility´, i.e. local regions in which the molecules have higher mobility than the surrounding molecules thus giving rise to a “local” relaxation process.[53] Another interpretation of the JG relaxation is given by the so-called Coupling Model, which considers the JG relaxation as a single-molecule precursor of the collective α process.[54,55]. According to this model, the relaxation times of the α and JG process are related as:

$$\tau_{JG} = t_c^n (\tau_\alpha)^{1-n} \qquad [2.27]$$

Here t_c is the crossover time (determined by the intermolecular interactions and insensitive to temperature, commonly ≈2 ps) and n is equal to $1-\beta_{KWW}$, where β_{KWW} is the exponent of the stretched Kohlrausch correlation function describing the α loss feature in the time domain (see section 3.5.1).

It should be finally pointed out that secondary relaxation processes can also correspond, in heterogeneous samples, to the motion of individual molecules or small clusters surrounded by heterogenous neighbors. In such case the non-cooperativity of the process stems from the lack of a sufficiently large number of molecules to achieve a cooperative relaxation.

Bibliography

[1] J.C. Maxwell, *Phil. Trans,* vol.155, p. 459, 1865.

[2] J.C. Maxwell, *Phil. Trans,* vol. 158, p.643, 1868.

[3] F. Kremer, A. Schönhals *Broadband Dielectric Spectroscopy.* Berlin: Springer, 2002.

[4] J. McConnell, *Rotational Brownian motion and Dielectric Theory*. London: AcademicPress, 1980.

[5] H. Fröhlich ,*Theory of Dielectrics*. Oxford: Clarendon Press, 1958.

[6] Faraday, M. *Phil. Trans*, vol.128, p.79, 1837.

[7] P. W. Anderson, *Science*, vol. 267, p.1615, 1995.

[8] M. D. Ediger, S. A. Angell, S. R. Nagel, *J. Phys.Chem.*, vol.100, p. 13200, 1996.

[9] L. Landau, E. M. Lifschitz. *Textbook of theoretical physics, vol.II. Classical field theory*, Berlin: Akademie-Verlag, 1977.

[10] C. J. F. Böttcher, O. C. Belle, P. Bordewijk, Rip A. *Theory of electric polarization, vol. I (2nd edition). Dielectrics in static fields.* Amsterdam, Oxford, New York: Elsevier.

[11] O. Exner. *Dipole moments in organic chemistry*. Georg Thieme Publishers Stuttgart: Germany 1975.

[12] D. J. Griffiths. *Introduction to Electrodynamics.* New Jersey: Prentice Hall 1999.

[13] C. J. F. Böttcher, P. Bordewijk *Theory of electric polarization, vol. II (2nd edition). Dielectrics in time-dependent fields.* Elsevier Amsterdam, Oxford, New York: Elsevier, 1978.

[14] V.V. Daniel. *Dielectric relaxation.* London and New York: *Academic Press*, 1967.

[15] H. A. Kramers. *Atti. Congr. Int.* Fisci, Como. vol2, p. 545,1927.

[16] R. Kronig *J. Opt. Soc. Amer.* vol.12, p. 547, 1926.

[17] William, D. Callister, Jr. *Materials science and engineering*. New York: John Wiley & Sons 2000.

[18] H. A. Lorentz *Ann Phys*, vol. 9, p. 614,1879.

[19] P. F. Mossotti. *Bibl Univ Modena* vol.6, p.193, 1847.

[20] R. *Die mechanische Wärmelehre, Vol. II* Braunschweig. 1879.

[21] L. Onsager. *J. Am. Chem. Soc.*, vol. 58 p. 1486, 1938.

[22] J. G. Kirkwood. *J. Chem. Phys,.* vol. 58, p. 911, 1939.

[23] J. G. Kirkwood. *Ann NY Acad. Sci.*, vol. 40, p. 315, 1940.

[24] J. G. Kirkwood. , *J. Chem. Phys.*, vol. 4, p. 592,1936.

[25] E. Barsoukov, J. R. Macdonald *Impedance Spectroscopy: Theory, Experiment, and Applications*. Wiley 2005.

[26] E. Warburg *Ann. Phys.*, vol. 6, p.125. 1901.

[27] H. P. Schwan, *Ann NY Acad. Sci.* vol. 148, p.191,1968.

[28] A.K. Jonscher *Nature, vol.* 267, p. 673, 1977.

[29] R.W. Wagner. *Arch Elektrotech*. vol. 2, p. 371, 1914.

[30] R.W. Sillars *J. Inst Elect Eng*, vol. 80, p. 378, 1937.

[31] T. Hannai In: Sherman P (ed) *Emulsion science*. New York: Academic Press, 1968.

[32] S. Takashima *Electrical properties of biopolymers and membranes.* Bristol: Adam Hilger 1989.

[33] J. C. Maxwell *Treatise on electricity and magnetism*. Oxford: Clarendon. 1982.

[34] RW. Wagner *Arch Elektrotech.*, vol. 2, p. 371, 1914.

[35] RW. Sillars *J. Inst Elect Eng.*, vol. 80, p. 378, 1937.

[36] (a) J. L. Barton. *Verres Refract* vol. 220, p.328, 1966. (b) T. Nakajima *Annual Report. Conference of electric Insulation and Dielectric Phenomena.* National Academy of Sciences Washington DC. 1971. (c) H. Namikawa *Non-Cryst Solids*, vol. 8, p.173, 1975 (1975).

[37] J. C. Dyre, T. B. Schroder. *Reviews of Modern Physics,* vol. 72, p. 3, 2000.

[38] D. L. Sidebottom *Phys. Rev.*, vol. 82, 1999.

[39] R. Brad, P. Lunkenheimer, A. Loidl *Phys. Rev. B*, vol. 56, p. R5713, 1997.

[40] R. Brand, P. Lunkenheimer, A. Loidl. *J. Chem. Phys.*, vol. 116, p.10386, 2002.

[41] E. Donth *The Glass transition. Relaxation Dynamics in Liquids and Disordered Materials*, *Springer Series in Material Science II.,* vol. 48. Berlin: Springer Verlag, 1998.

[42] J. Ll. Tamarit, M. A. Perez-Jubindo, M. R. de la Fuente *J. Phys.: Condensed Matter*, vol. 9, p. 5469, 1997.

[43] M. Romanini, J. C. Martinez-Garcia, J. Ll. Tamarit, S. J. Rzoska, M. Barrio, L. C. Pardo, A. Drozd-Rzoska. *J. Chem. Phys.*, vol. 131, p. 184504, 2009.

[44] M. Zachariah, M. Romanini, P. Tripathi, J. Ll. Tamarit, R. Macovez, *Phys. Chem. Chem. Phys.,* vol. 17, p. 16053, 2015.

[45] (a) H. Vogel, *Phys. Z* vol. 22 p. 645, 1921. (b) G.S. Fulcher, *J. Am. Ceram Soc*. vol. 8, p. 339, 1925. (c) G. Tammann, W. Hesse *Z. Anorg. Allg. Chem*, vol.156, p. 245, 1926.

[46] C. A. Angell, K. L. Ngai, G. B. McKenna, P. F. McMillan, S. W. Martin. *J. Appl. Phys.*, vol. 88, p. 3113, 2000.

[47] K. L. Ngai, M. Paluch *J. Chem. Phys.*, vol 120, p. 246, 2004.

[48] G. P. Johari, M. J. Goldstein *Chem. Phys.* vol. 53, p. 2372, 1970.

[49] P. Lunkenheimer, L. C. Pardo, M. Köhler, A. Loidl *Phys. Rev. E,* vol. 77, p. 031506, 2008.

[50] S. Pawlus, M. Paluch, M. Sekula, K. L. Ngai, S. J. Rzoska, J. Ziolo *Phys. Rev. E*, vol. 68, p. 021503, 2003.

[51] T. Bauer, M. Kohler, P. Lunkenheimer, A. Loidl, C. A. Angell

J. Chem. Phys., vol. 133, p. 144509, 2010.

[52] S. Capaccioli, K. L. Ngai, N. Shinyashiki *J. Phys. Chem. B*, vol. 111, p. 8197, 2007.

[53] G. P. Johari, M. Goldstein *J. Chem. Phys.*, vol. 53, p. 2372, 1970.

[54] K. L. Ngai *Solid State Phys.,* vol. 9, p. 141, 1979.

[55] K. Y. Tsang, K. L. Ngai *Phys. Rev. E*, vol. 54, p. 3067, 1997.

Chapter 3

EXPERIMENTAL TECHNIQUES

3.1 Thermal Analysis Methods

3.1.1 Thermogravimetric Analysis

Thermogravimetric analysis (TGA) is a thermal analysis tool used to study changes in the mass of materials containing reactive or volatile molecular species, the mass change being measured as a function of increasing temperature (or time). Phenomena such as absorption and desorption (of physi- and chemi-sorbed moieties), vaporization and sublimation, desolvation (or in general separation of components in mixed samples), oxidation and chemical decomposition can be studied.[1,2] In the TGA measurements employed in this thesis, the decreasing weight of the sample was determined as a function of the (increasing) temperature. Weight loss can occur through various processes: decomposition, evaporation of water or other volatile species, desorption of adsorbed molecules, etc. In organic chemistry, TGA is commonly employed to study decomposition and dehydration, as the breaking of chemical or hydrogen bonds can release small volatile molecules (carbon dioxide, carbon monoxide, water vapor etc.). TGA is also useful for composition analysis of multi-component materials as each component can be individually separated (due to the different decomposition or sublimation pressure vapor) in a stepwise fashion to quantitatively determine the amount of each component in the material.[3]

TGA experiments described in this thesis were performed by means of a Q50 thermo-balance from TA instruments. For this purpose, the samples, with masses between 0.5 and 10 mg, were placed into aluminum pans (TA instrument) and measurements were performed in a temperature range between room temperature (300 K) and 650 K. Heating rates between 2 and 10 K/min were employed. Nitrogen gas was used to control the sample atmosphere and the flow rate of the gas was regulated by a mass flow controller.

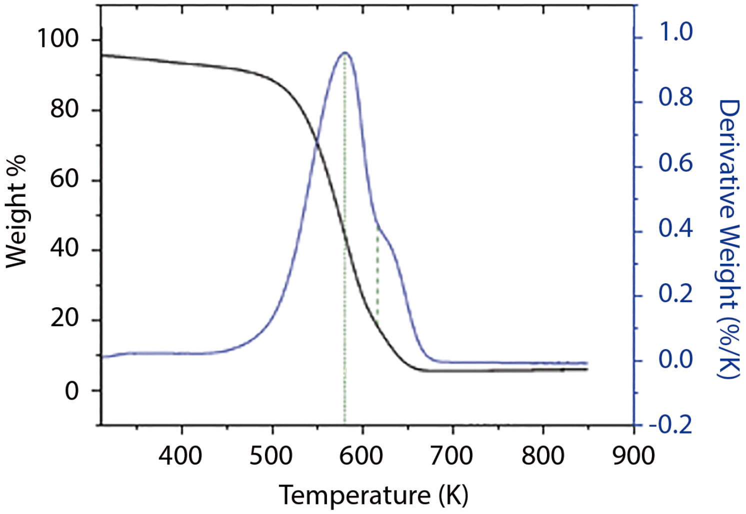

Figure 3.1 Example of a TGA thermograph (black) and its first derivative (dm/dT), where two mass loss steps are visible.

The mass of the samples is recorded and plotted as a function of temperature. A typical TGA graph (left y-axis) and the first derivative of the mass loss (right y-axis) are displayed in Figure 3.1. The mass loss is visible as a step-like decrease (in this example, a high percentage of the initial mass is lost (sublimates) by the end of the process. Looking in more detail, it is seen that this change can be deconvoluted into two smaller steps, not visible by eye in the TGA graph of Figure 3.1, but clearly resolved in the temperature derivative of the mass loss.

3.1.2 Differential Scanning Calorimetry

In conjunction with TGA measurements, Differential Scanning Calorimetry (DSC) was used for the thermal analysis. DSC is a physico-chemical method of thermal analysis, which can be used to determine the transition temperatures of phase transformations, such as melting or crystallization, as well as the thermal energy (enthalpy) changes during the phase transitions. The enthalpy of transition can be determined by comparing the difference in the amount of heat that is provided to the sample under investigation with that provided to a reference material in the same temperature interval.[1,4] The reference used for DSC has a well-known heat capacity which varies slowly over the measurement. For the calibration of the temperature and enthalpy scales, the most commonly used substance is indium due to its well-identified melting point and heat of fusion. During a phase transition, the amount of heat supplied to the sample depends on whether the transformation process is endothermic or exothermic. Endothermic processes require a positive heat flow in order to occur; for example, to melt a solid into the liquid state, an incoming heat flow is required, corresponding to the latent heat of transformation. Conversely, exothermic processes release heat; this occurs in the reverse process, namely crystallization.

In this thesis, DSC experiments were conducted by means of a Q100 thermal analyzer from TA instruments equipped with a chiller device which enables operation in a wide temperature range between 183 and 823 K. Heating-cooling rates between 2 and 10 K/min were commonly employed. Purge gases (nitrogen or helium) were used to control the sample atmosphere and the flow rates of the gases was regulated by a mass flow controller. The samples, with masses between 0.5 and 20 mg, were placed in aluminum pans (TA instrument) or in high-pressure stainless steel pans with gold covers (Perkin Elmer). The latter were used in order to prevent reactions between the sample and the container or for samples with high vapor pressure.

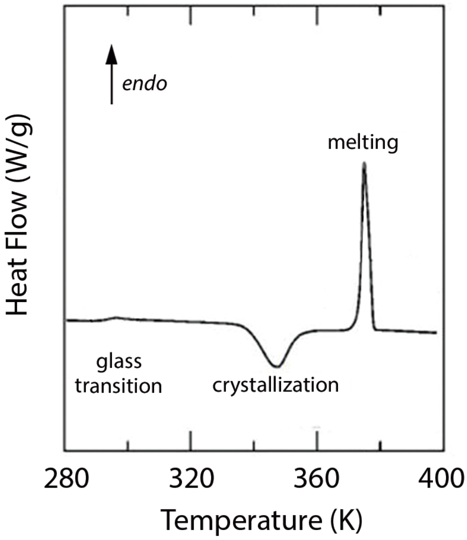

Figure 3.2 Example of a DSC thermograph in which a glass transition, a crystallization and a melting peak are shown.

An example of a DSC thermograph is shown in Figure 3.2, acquired on a glass-forming material upon heating. At low temperatures, a small bump signals the glass transition temperature (T_g), associated with a low enthalpy relaxation related with aging effects on the glass. Above this temperature, the material is in the metastable supercooled liquid state. Upon further heating, the mobility in the material is high enough for recrystallization to occur. Since the entropy decreases, heat is released in the crystallization (exothermic process), as visible from the corresponding downward peak. As the crystal is further heated, an intense endothermic peak (upwards) signals the melting process.

3.2 Vibrational Spectroscopy Techniques (FTIR, RAMAN)

3.2.1 Fourier-transform Infrared Spectroscopy

Fourier-transform Infrared Spectroscopy (FTIR) technique is an optical absorption spectroscopy tool which detects the dipolar inter-atomic vibrations of the constituent molecules of a sample. When infrared radiation passes through a sample, part of the radiation is absorbed by the molecules and the rest is transmitted through the material. This energy absorption results in vibrations of the inter-atomic bonds about their equilibrium distance. In order for a vibration to be visible (“active”) in infrared spectroscopy there must be a change in the dipole moment during the vibrations of the involved atoms. The infrared spectrum consists of absorption bands at definite frequencies (wavenumbers), corresponding to the characteristic frequency of vibration of specific intramolecular bonds. Each molecule has a characteristic vibrational spectrum, which can be used as a fingerprint for their identification in composite substances. Hence FTIR is employed to study chemical composition. Quantitative information can be obtained on the amount of the different molecular species within a substance, which can be extracted from the relative intensity of the absorption peaks.[5,6] In this thesis we acquired infrared spectra with a Thermo Scientific Nicolet 6700 spectrometer in the mid-infrared range (4000 - 400 cm^{-1}). The spectrophotometer was equipped with a He/Ne laser source, a CsI beamsplitter and a DTGS-CsI detector. The wavenumber resolution was of 1 cm^{-1}. To measure powder samples, pellets were made by mixing the sample with the IR-transparent KBr powder.

3.2.2 Raman Spectroscopy

Another important type of vibrational analysis tool is Raman spectroscopy, which is complementary to FTIR spectroscopy. The Raman scattering is not based on the absorption of radiation as in FTIR; in fact, the excitation wavelength for Raman is commonly in the visible (and not IR range). Instead, the radiation induces the excitation of the system to a higher energy, by inelastic, nonlinear light scattering. The Raman spectrum records the intensity of the scattered light as a function of the “Raman shift”, which is the difference between the source radiation and the observed one after scattering. The intensity gives information analogous to the band intensities in FTIR.[7] The main difference between Raman and FTIR is the selection rule that the microscopic light-matter interaction must fulfill; this leads to a different sensitivity of the two techniques (whence the complementarity) to specific molecular vibrations. For a vibration to be detected (“active”) in Raman spectroscopy there should be a change in the bond polarizability (deformation of the electron cloud).

In this thesis we employed a Raman spectromicroscopy setup, namely the LABRAM HR 800 system with a laser excitation wavelength of 532 nm (green). A silicon wafer was used as a reference for calibration. Spectra were recorded in the wavenumber range between 50 cm^{-1} and 3700 cm^{-1}. Unlike for FTIR, there was no need of sample preparation in the form of a pellet for Raman measurements. In fact, Raman spectra were also collected on liquid samples, by depositing a drop of sample onto a glass substrate.

3.3 X-ray powder diffraction

The identification of the crystalline structure of solids synthesized as polycrystalline powders can be carried out using the X-ray powder diffraction (XRPD) characterization technique. In such an experiment, the X-ray radiation generated by a cathode ray tube, is diffracted by a single crystal to achieve monochromaticity and directed toward the sample, placed in a capillary or onto a substrate. After the diffraction of the X-ray radiation by the sample, constructive interference rings will appear whenever the Bragg´s law condition is satisfied: $n\lambda=2d\sin\theta$. Bragg’s law gives the correlation between the diffraction angle and the distance between crystallographic planes for a given wavelength of the X-ray radiation, which is fixed as it depends on the material of which the anode of the X-ray tube is made of. Unlike diffraction by a single crystal, a powder sample consists of randomly oriented crystalline domains, so that instead of a diffraction spot a whole diffraction ring is formed, corresponding to all the possible orientation directions of the lattice. From the conversion of the angular position of the diffraction peaks to d-spacings and their analysis, it is possible to identify the material's lattice symmetry as well as the lattice parameters.

For this thesis, high-resolution X-ray powder diffraction (XRPD) profiles were recorded by means of a vertically mounted INEL cylindrical position-sensitive detector (CPS120). The generator voltage and current was commonly set to 35 kV and 35 mA, respectively, and monochromatic Cu Kα1 radiation (λ=1.54059 Å) was selected with an asymmetric focusing curved quartz monochromator. The detector was used in the Debye-Scherrer geometry (transmission mode), yielding diffraction profiles over a 2θ range between 4° and 120° with an angular step of 0.029° (2θ). External calibration by means of cubic phase $Na_2Ca_2Al_2F_4$ was performed for channels to be converted into 2θ-degrees by means of cubic spline fittings.[8] The powder sample was inserted in a Lindemann capillary tube (commonly of 0.5 mm diameter) which was continuously rotated perpendicularly to the X-ray beam direction during data collection, to minimize possible effects of preferred orientations. Temperature control was achieved with a liquid-nitrogen 700 series Cryosystem Cooler from Oxford Cryosystems operating from 500 K to 90 K with a temperature accuracy of 0.1 K. Peak positions are determined by fits with pseudo-Voigt functions performed with a dedicated software and in some cases Rietveld refinement was applied.

3.4 Broadband Dielectric Spectroscopy

The main experimental tool used in this thesis to investigate the microscopic dynamic behavior of the materials is dielectric spectroscopy, which can be carried out in an extremely wide spectral range, in principle between 10^{-3} and 10^{12} Hz. Dielectric spectroscopy enables for example the study of the molecular dynamics across the glass transition from a supercooled liquid to a glass state; in dipolar substances, such dynamics are visible as a dielectric loss feature known as α relaxation[9,10] (see chapter 2). Another important application of dielectric spectroscopy is the study of the molecular dynamics of molecules in a confined geometry. By measuring the dynamics of the guest molecules enclosed in host systems, the effect of confinement on the orientational or diffusional dynamics can be investigated[11,12] (as well as the interactions between the guest molecules and the host matrices in heterogeneous systems.[13]

Dielectric spectroscopy allows the experimental determination of the complex dielectric function in the frequency and the time domain.[14] In this thesis, we determined the dielectric response of organic samples to a frequency-varying electric field, and we will consequently focus on frequency-domain measurements.[10]

All the measurements of this thesis were acquired on the frequency range between 10^{-2} and 10^{7} Hz by means of a Novocontrol Alpha-Analyzer. Within this setup, the material to be studied is sandwiched between two metallic plates in a parallel-plate capacitor configuration. The filled capacitor is subjected to an alternate (a.c.) electric field oscillating at a variable frequency ω and the response of the material is determined by its complex impedance $Z^*(\omega)$. The analysis is usually carried out in terms of the complex dielectric permittivity $\varepsilon^*(\omega)$, obtained from the complex impedance ($Z^*(\omega)$) as:

$$\varepsilon^*(\omega) = \frac{1}{i\omega Z^*(\omega) C_0} \quad [3.1]$$

where C_0 is the vacuum capacitance of the capacitor where the sample is placed. The dielectric data are acquired as isothermal frequency scans.

In order to measure a powder sample, a capacitor is built by sandwiching the powder material between two metal discs (stainless steel) and pressing it with a hydraulic press to achieve a pellet as homogeneous as possible. A Teflon ring is placed around the sample capacitor to prevent stray electric fields at the exterior edge of the capacitor (Figure 3.3 (a)). The separation between the discs gives the thickness of the pellet, which is related to the vacuum capacitance in eq. 3.1. The capacitor is then placed in the sample holder between the two electrodes of the holder (Figure 3.3 (b)), and the whole setup is then inserted inside the cryostat for temperature control.

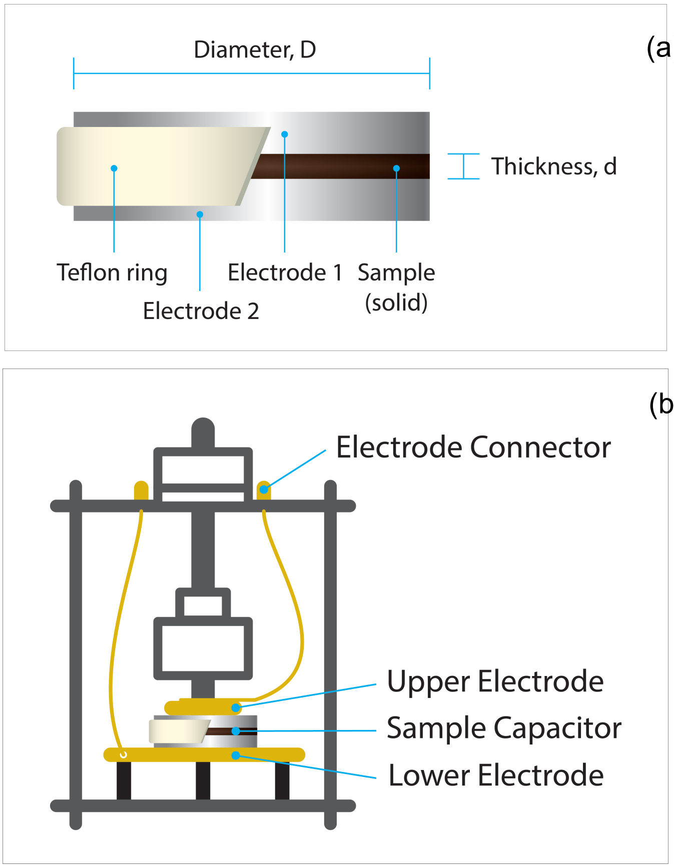

Figure 3.3 (a) Typical scheme of a parallel plate capacitor configuration for solid samples, prepared with two round stainless steel discs (electrodes). (b) Schematic representation of the sample holder configuration with the sample capacitor between the holder electrodes.[15]

The variation of the dielectric spectra with temperature is studied with the help of a Novocontrol Quatro Cryosystem, which controls the sample´s temperature during isothermal frequency scans (Figure 3.4). It consists of a cryostat, where the sample holder is placed, a liquid nitrogen Dewar with pressure sensor, two heating units (Dewar and gas heaters), three temperature controllers (for the Dewar, gas and sample temperatures) and a vacuum pump. The sample temperature is measured by using a Platinum resistor sensor (PT-100 Ω), which is in thermal contact with one of the capacitor plates. The temperature range of this system can vary between 116 K and 773 K with a precision of 0.1 K.

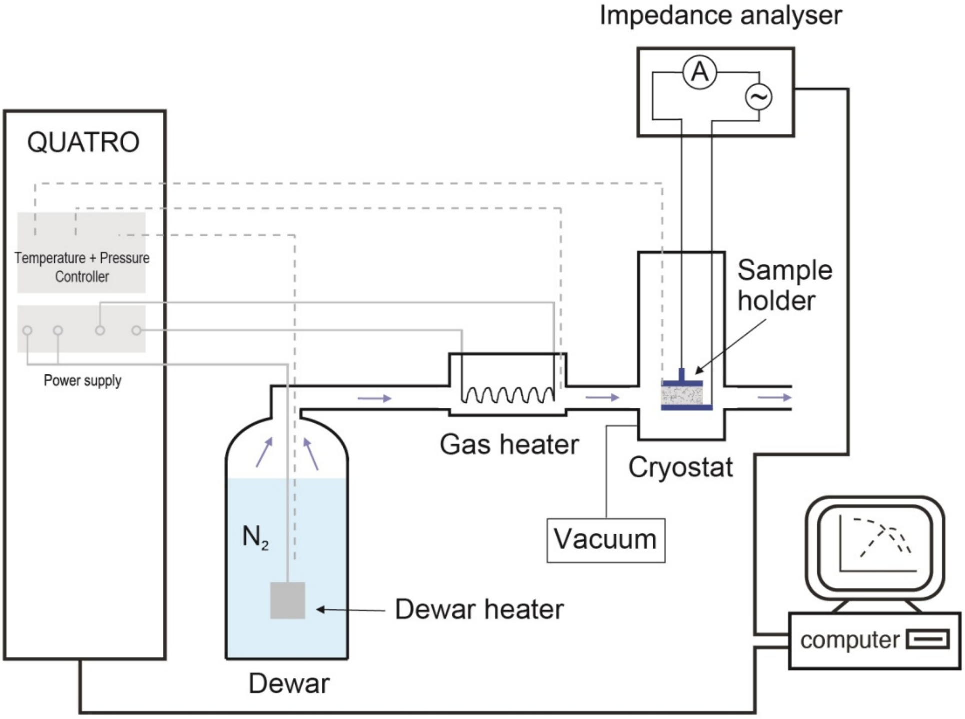

Figure 3.4 Schematic representation of the experimental setup of a temperature-dependent broadband dielectric measurement.[14,16]

3.5 Analysis of Dielectric Data

As discussed above, dielectric spectroscopy yields the complex dielectric permittivity of a sample, ε*(ω). The typical frequency dependence of the real and imaginary parts of the complex permittivity is illustrated in Figure 3.5, which depicts the typical real and imaginary permittivity spectra obtained in a dielectric spectroscopy measurement. The spectrum of the real part of the permittivity ε'(ω) (continuous line) displays a step-like decrease with increasing frequency. The imaginary part ε''(ω), plotted in logarithmic scale (dashed line), displays a peak (called "dielectric loss") in correspondence with the step-like decrease in the real part. At low frequencies, the imaginary part displays a linear background proportional to inverse frequency, which is due to the dc electrical conductivity contribution. Both the real and the imaginary part of the complex permittivity convey the same information, due to their inter-dependence (see chapter 2).[10] Information on the dynamics of the studied systems are extracted from the modeling of the imaginary part by means of various fitting functions.

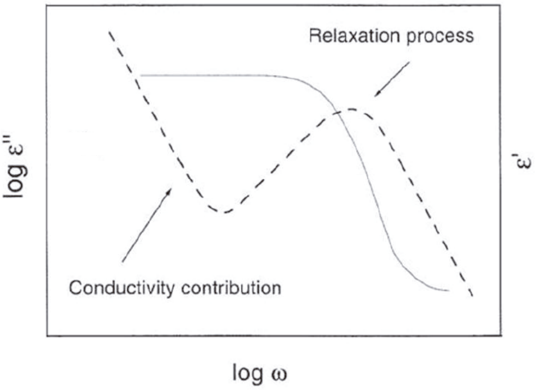

Figure 3.5 Typical spectrum of the real (solid line) and the imaginary part (dashed line) of the complex dielectric permittivity, as measured with broadband dielectric spectroscopy.[10]

In practice the analysis of a dielectric loss spectrum serves for the determination of the relaxation times of the processes that are present in the spectrum. Different phenomenological models are employed due to the fact that each process (loss feature) is actually characterized by a complex distribution of relaxation times, rather than a single one, leading to different possible forms (shapes) of loss peaks. The characteristic relaxation time (τ) and the dielectric strength ($\Delta\varepsilon$) are two of the most important parameters that can be obtained from the fitting procedures described in the next subsection. Moreover, from the slopes in low and high frequency region of the loss peak shape parameters can be extracted, which give information about the distribution of the relaxation times and depend on the extent of the interactions that take place between dipoles.[10]

3.5.1 Relaxations Models

Debye was the first to establish a microscopic model of the frequency dependence of the complex dielectric function. The basic idea is the following: under a time-varying applied electric field, the material´s dipoles will tend to re-orient to become aligned with the field. Debye´s function is a simple model to describe such a reorientational process, which is based on the assumption that all the dipoles inside the material reorient with the same characteristic time, τ_D, called Debye relaxation time. This is justified if one considers the sample to be a viscous medium containing otherwise non-interacting dipoles. For such a system, under the application of a time-varying electric field, the rate of change of material´s polarization will be proportional to the instantaneous value of the polarization, and will be given by[17]

$$\frac{dP(t)}{dt} = -\frac{1}{\tau_D}P(t). \quad [3.2]$$

The solution to the previous equation (first order differential equation) is:

$$P(t) = P_0 e^{-\frac{t}{\tau_D}} \qquad [3.3]$$

By taking the Fourier transform, we get:

$$P(t) = \int_0^{\infty} dt P_0 e^{-\frac{t}{\tau_D}+i\omega t} = \frac{P_0\tau_D}{1 + i\omega\tau_D} \qquad [3.4]$$

With the help of the equation $\mathrm{P}(\omega) = (\varepsilon * (\omega) - 1)\mathrm{E}(\omega)$ [3.5], we obtain the complex dielectric function according to Debye´s model as:

$$\varepsilon^*(\omega) = \varepsilon_\infty + \frac{\Delta\varepsilon}{1 + i\omega\tau_D} \qquad [3.6]$$

where $\Delta\varepsilon = \varepsilon_s - \varepsilon_\infty$ is the dielectric strength of the process, with $\varepsilon_s = \lim_{\omega \to 0} \varepsilon'(\omega)$ and $\varepsilon_\infty = \lim_{\omega \to \infty} \varepsilon'(\omega)$. The real and imaginary parts of equation [3.6] are shown in Figure 3.5 (a conductivity term was added to ε''(ω)). The Debye relaxation time τ_D coincides with the position of the maximum of the dielectric loss peak $\left(\omega_{peak} = 2\pi f = \frac{1}{\tau_D}\right)$. Such loss peak is symmetric with a full width at half maximum of 1.14 decades.[18]

In real systems, the dielectric loss peak is broader and/or less symmetric than in the ideal (non-interacting) Debye case.[19] As mentioned, the broadening of the relaxation peak is caused by the existence of a distribution of distinct relaxation times, arising from strong dipolar interactions, high association degree and steric hindrance between the constituent molecules. The non-Debye behavior of a material´s dynamical response is generally described by functions which lack the detailed theoretical basis that supports the Debye model function. These phenomenological models include, in the frequency domain, the Havriliak-Negami function[20] ,Jonscher’s theory[21] and the Kohlrausch-Williams-Watts (KWW)[22] function in the time domain. A common characteristic of all frequency-domain models is the power law dependencies at high and low frequencies, while the KWW function is characterized by power law dependence only at short times (high frequencies).[10]

Havriliak and Negami (HN) introduced a generalized loss function, which reads:

$$\varepsilon^*{}_{HN}(\omega) = \varepsilon_\infty + \frac{\Delta\varepsilon}{[1+(i\omega\tau_{HN})^{\alpha}]^{\beta}} \quad [3.7]$$

Here α and β ($0<\alpha,\ \beta \leq 1$) are the slopes of the loss peak at low ($\square<\square_{\text{peak}}$) and high ($\square>\square_{\text{peak}}$) frequencies, respectively, which depend on the distribution of the relaxation times. The exponent α describes a symmetric broadening of the peak, while β describes an asymmetric one. It should be noticed that for $\alpha = \beta = 1$, the Debye function is obtained. The inverse of τ_{HN} is not the frequency of maximal loss (characteristic relaxation frequency); rather, the latter is obtained from the Havriliak-Negami parameter (τ_{HN}) as[23]

$$\omega_{max} = \frac{1}{\tau_{HN}}\left[sin\frac{\alpha\pi}{2+2\beta}\right]^{\frac{1}{\alpha}}\left[sin\frac{\alpha\beta\pi}{2+2\beta}\right]^{-\frac{1}{\alpha}} \quad [3.8]$$

For polymeric materials, a symmetric broadening of the peak is usually observed, which is described by a special case of the HN function, called Cole-Cole (CC) model function:[24]

$$\varepsilon^*{}_{CC}(\omega) = \varepsilon_\infty + \frac{\Delta\varepsilon}{1+(i\omega\tau_{CC})^{\alpha}} \qquad [3.9]$$

In the last equation, τ_{CC} is the Cole-Cole relaxation time and coincides with the maximal loss ($\omega_{peak}=2\pi f=\frac{1}{\tau_{CC}}$), and α is a shape parameter. In the case of liquids and molecular glass-forming materials, an asymmetric profile of the loss peak is often observed, described sometimes by another special case of HN function, namely the Cole-Davidson:[25,26]

$$\varepsilon^*{}_{CD}(\omega) = \varepsilon_\infty + \frac{\Delta\varepsilon}{[1+i\omega\tau_{CD}]^{\beta}} \qquad [3.10]$$

Here τ_{CD} is the Cole-Davidson relaxation time[23] , which is correlated with the maximal loss by

$$\omega_{max} = \frac{1}{\tau_{CD}}\tan\left[\frac{\pi}{2+2\beta}\right] \qquad [3.11]$$

Dielectric characterization is mostly carried out in the frequency domain, which explains why the above-mentioned model functions and especially the Havriliak-Negami model are widely used in the related scientific literature.

In the time domain, a non-Debye relaxation behavior can be represented by the Kohlrausch-Williams-Watts model function[27] (KWW) which reads:

$$\varepsilon(t) - \varepsilon_\infty = \Delta\varepsilon\left(1 - e^{\left(-\frac{t}{\tau_{KWW}}\right)^{\beta_{KWW}}}\right) \qquad [3.12]$$

Here τ_{KWW} is the characteristic relaxation time and β_{KWW} ($0<\beta_{KWW}\leq 1$) is the stretched exponential parameter, which leads to an asymmetric broadening of $\varepsilon(t)$ at short times (high frequencies) compared to an exponential decay ($\beta_{KWW}=1$).

It is known that the dielectric properties measured in frequency and time domain are related to each other by a Fourier transform. Although, the KWW function has no analytic Fourier transform in the frequency domain. There exists however an approximate connection between the HN functions and the KWW expression. Based on the fact that CD function (equation 3.10) and KWW model (equation 3.12) have only one shape parameter, Patterson and Lindsay derived a relationship between the two expressions.[28] Colmenero et al extended this work to find the inter-correlation between the HN exponents and the KWW stretched parameters,[29] obtaining the following approximate relations:

$$log \frac{\tau_{HN}}{\tau_{KWW}} = 2.6(1 - \beta_{KWW})^{0.5} e^{(-3\beta_{KWW})} \qquad [3.13]$$

$$\alpha\beta = {\beta_{KWW}}^{1.23} \qquad [3.14]$$

Because the HN function has two shape parameters and the KWW only one, the HN function is not exactly the Fourier transform of KWW in time domain nor vice versa. Since the dielectric studies of this work are carried out in frequency domain, we use exclusively the frequency-dependent model functions for the analysis of the experimental data, and rely on Eq. 3.14 to estimate the stretched β_{KWW} exponent, when needed.

Bibliography

[1] M. E. Brown *Introduction to thermal analysis: techniques and applications.* London, New York: Chapman and Hall, 1988.

[2] F. Carrasco, P. Pagès, J. Gámez-Pérez , O.O. Santana, M.L. Maspoch *Polym. Degrad. Stab.*, vol. 95, p. 116, 2010.

[3] *http://home.engineering.iastate.edu*

[4] E. Pungor, *A practical guide to instrumental analysis.* Florida: Boca Raton, 1995.

[5] J. Coates *Interpretation of Infrared Spectra, A Practical Approach.* Encyclopedia of Analytical Chemistry, 2006.

[6] B. Stuart. *Infrared Spectroscopy: Fundamental and Applications.* New York: Wiley. 2004.

[7] *http://serc.carleton.edu/NAGTWorkshops/mineralogy/mineral_physics/raman_ir.html*

[8] M. Evain, P. Deniard, A. Jouanneaux, R. Brec *J. Appl. Cryst.*, vol. 26, p. 563, 1993.

[9] P. Lunkenheimer, U. Schneider, R. Brand, A. Loidl *Contemporany Physics.,* vol. 41, p. 15, 2000.

[10] F. Kremer, A. Schönhals *Broadband Dielectric Spectroscopy.* Berlin: Springer, 2002.

[11] J. Leys, G. Sinha, C. Glorieux, J. Thoen *Phys. Rev. E.,* vol. 71, p. 051709, 2005.

[12] E. Mitsari, M. Romanini, N. Qureshi, J.L. Tamarit, M. del Barrio, R. Macovez *J. Phys. Chem. C.*, Article ASAP, 2016.

[13] R. Macovez, E. Mitsari, M. Zachariah†, M. Romanini, P. Zygouri, D. Gournis, J.L. Tamarit *J. Phys. Chem. C.*, vol. 118, p. 4941, 2014.

[14] M. F. García-Sánchez, J-C. M'Peko, A. Rabdel Ruiz-Salvador, Geonel Rodríguez-Gattorno, Yuri Echevarría, Floiran Fernández-Gutierrez, A.Delgado *J. Chem. Educ.*, vol. 80, p. 1062, 2003.

[15] *http://www.novocontrol.de/*

[16] P. Frubing *Dielectric spectroscopy (Laboratory Lectures notes)* University of Potsdam, Institute of Physics, Germany, 2011.

[17] P. Debye *Polar molecules. Chemical catalog,* reprinted by Dover, New York, 1929.

[18] O. Exner, *Dipole moments in organic chemistry*; Germany: Georg Thieme Publishers Stuttgart, 1975.

[19] J. C. Maxwell *Phil. Trans.*, vol. 155, p.459, 1865; *Ibid*, vol. 158, p. 643, 1868; *Treatise on Electricity and Magnetism*; New York: Dover, 1954.

[20] S. Havriliak, S. Negami *Polymer*, vol. 8, p. 161, 1967.

[21] A.K. Jonscher *Dielectric Relaxation in solids.* London: Chelsea Dielectrics Press, 1983.

[22] R. Kohlrausch *Ann Phys*, vol.12, p. 393, 1847.

[23] R. Diaz-Calleja *Macromolecules,* vol. 33, p. 8924, 2000.

[24] K.S. Cole, R.H. Cole *J. Chem. Phys.*, vol. 9, p. 341, 1941.

[25] D.W. Davidson, R.H. Cole *J. Chem. Phys.*, vol. 18, 1417, 1950.

[26] D.W. Davidson, R.H. Cole *J. Chem. Phys.*, vol. 19, p. 1484, 1951.

[27] G. Williams, D.C. Watts *J. Chem. Soc*. *Faraday Trans II.*, vol. 68, 1045, 1970.

[28] C.P. Lindsay, G.D. Patterson *J. Chem. Phys.*, Vol. 73, p. 3348, 1980.

[29] F. Álvarez, A. Alegría, J. Colmenero *Phys. Rev. B*, vol. 44, 7306, 1991.

Chapter 4

DYNAMICS OF WATER INSIDE SOLID RHODAMINE 6G.

4.1 Introduction

Fluorophore molecules are fluorescent chemical compounds, which typically consist of aromatic groups in various combinations, or plane or cyclic molecules with several π-bonds. These molecules absorb light in a specific range of wavelengths and re-emit it at longer wavelengths (lower energy). They can be used as dyes for staining tissues or cells for analytical methods (fluorescent imaging and spectroscopy). Moreover, they can be covalently bonded to macromolecules as markers for affine or bioactive reagents (antibodies, nucleic acids, etc).[1]

Rhodamines and fluoresceins are two fluorophore families of the xanthene type, which encompasses a large number of organic dyes. The backbone of these dyes consists of the typical xanthene structure, which is illustrated in Figure 4.1.

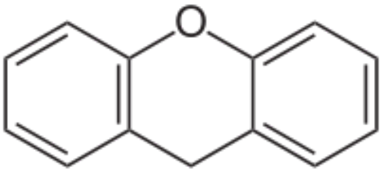

Figure 4.1 Molecular structure of the xanthene ring.

Rhodamines have high chemical stability and they are relatively easy to manufacture, without the need of complicated purifications, unlike most other dyes. They can be detected easily and inexpensively with the use of fluorometers. Rhodamine 6G, of chemical formula $C_{28}H_{31}N_2O_3Cl$ (MW = 479.02 g/mol), is a highly fluorescent molecule of this family. Besides its use as a tracer dye within water in order to determine the rate and the direction of the flow and transport, it is used as a laser dye.

While the xanthene backbone is not by itself a planar moiety, the addition of external functional groups attached to it changes its structure. It is accepted that in Rhodamine 6G (hereafter Rh6G) the xanthene moiety is planar and lies in the same plane with the amino groups. On the other hand, the external phenyl group is twisted nearly perpendicular to the xanthene plane,[2] as it can be seen in Figure 4.2.

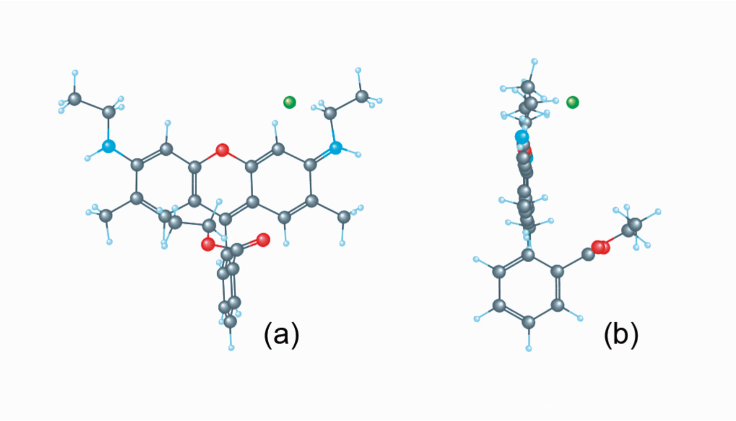

Figure 4.2 Molecular structure of Rh6G molecule in front (a) and side (b) view.

Due to its non-symmetric charge distribution the Rh6G cation possesses a whole-molecule dipole moment. It should be noted that the material (Rhodamine chloride) also possesses dipole moments due to the presence of the counter-ions, namely pointing from the chlorine ion to the positively charged nitrogen of the Rh6G cation.

At room temperature, Rh6G is a polycrystalline molecular powder. As a salt, it readily dissolves in polar solvents like methanol, ethanol, or water. This also emerges from the polar nature of the functional groups of the anion, which facilitates the interaction between the dye and the alcohol or aqueous solvent:[3] although as an ester it lacks hydroxyl groups, the Rh6G anion can participate in electrostatic interactions with polar molecules due to the presence of the electronegative oxygen. The polarity of the side groups and the fact that Rh6G is a chloride salt lead not only to hydrophilic character, but also to hygroscopic behavior. The pure Rh6G powder thus captures water vapor from the surrounding atmosphere.

4.2 Experimental methods

Rh6G chloride was purchased as a dark red polycrystalline powder from Sigma Aldrich with ≥ 95 % purity and it was used as received. Rh6G samples were kept in ambient atmosphere.

As thermal probes, we employed thermogravimetric analysis (TGA) and differential scanning calorimetry (DSC). In TGA experiments, the samples were heated from room temperature (300 K) to 553 K at a heating rate of 2 K per minute. During DSC measurement, heating/cooling cycles were performed with the same rate. The samples were weighed before and after the measurement.

Fourier transform infrared spectroscopy (FT-IR) was performed at room temperature in the mid-infrared wavelength range (4000 cm^{-1} - 400 cm^{-1}). The samples were prepared in pellet forms with the addition of potassium bromide (KBr). Due to the hygroscopic nature of KBr, we were keeping the powder to the furnace (373-383 K) for 20 hours prior to the measurement. The pellets have a diameter of ~13 mm. FT-IR characterization was carried out at the centre for research in nanoengineering (CRnE) and at the department of materials science and metallurgical engineering in Terrassa.

Dielectric measurements were acquired on Rh6G samples with a Novocontrol Alpha-analyzer equipped with a Quatro temperature controller using a nitrogen-gas cryostat. The measurements were performed in a frequency range of 10^{-2} to 10^{7} Hz and in a temperature interval from 168 to 440 K upon heating, while upon cooling measurement the interval was set from 440 to 200 K. The spectra were acquired every 5 K, with a temperature stability of ~0.5 K. The samples were prepared in a pellet form, sandwiched between two stainless steel disks using hydraulic press (20 kN). In the parallel-plate capacitor, the thickness of the samples was varying between 0.2 and 0.3 mm and the diameter of the disks was 2.2 mm.

4.3 Thermal Analysis of hydrated Rh6G

The thermal behavior of the hydrated Rh6G sample was determined by thermogravimetric analysis (TGA) and differential scanning calorimetry (DSC). Similar experimental procedures were followed for both characterization techniques. The TGA and its derivative thermogravimetric (DTG) curves are shown in Figure 4.3.

As mentioned, Rh6G behaves as a hygroscopic salt. Thus, the first mass loss of the TGA scan upon heating corresponds to the desorption of the water molecules from the Rh6G sample. The dehydration starts at ~350 K and continues up to 440 K, where the anhydrous sample is obtained. For the given experimental conditions, the maximum loss rate was observed at 393 K (see inset of Figure 4.3).

As visible in the same inset, the mass loss is structured, indicating that more than one water environments exist within Rh6G. Moreover, the desorption continues up to relatively high temperatures (440 K). Such extended temperature range of the dehydration process suggests that relatively strong adsorption interactions are present between the Rh6G matrix and the water molecules (so that a large thermal energy is needed in order to set the water molecules free). Weakly bound secondary water is instead generally lost already below the boiling point of pure water (373 K) when heating in nitrogen atmosphere[4] (see also chapters 5 and 6). Dehydration leads to a mass loss of about 2-3 % of the whole mass, which corresponds to the presence of about one H_2O molecule per Rh6G moiety.[5]

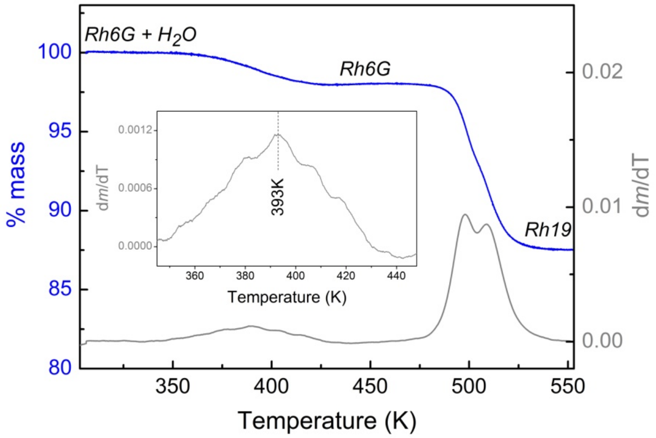

Figure 4.3 TGA thermograph (thick blue line) of the hydrated Rh6G sample and its first derivative (thin grey curve). For each plateau of the TGA curve, the corresponding chemical composition of the sample is indicated. The heating rate was 2 K/min. Inset: The derivative of the TGA curve in the temperature range of the dehydration (350 - 440 K).

The observed temperature range of the dehydration corresponds to physisorbed or intercalated water molecules, as chemisorption leads to yet higher water-desorption temperatures.[6] Different types of water environments and water-matrix interactions were reported for several systems such as different zeolites[7]and biological proteins.[8]

A second, prominent mass loss is observed around 473 K, temperature at which the sample is already anhydrous. This mass loss corresponds to the beginning of the Rh6G decomposition. It is known that the Rh6G disintegrates to a different rhodamine molecule, the neutral zwitterionic Rhodamine 19 (hereafter, Rh19); this process takes place above 473 K.[9] The thermal event corresponds thus to the disintegration of Rh6G (Figure 4.4), which involves in particular the transformation of the ester into an acid group. Such decomposition process is characterized by a double mass loss, as it can be seen easily from the derivative of the TGA curve (Figure 4.3). At the end of the decomposition all Rh6G has transformed into Rh19 with a loss of ~11 % of the total mass. This reduction in mass is compatible with the loss of a chlorine ion (Cl^-) and an ethyl group ($-CH_2CH_3$) per Rh6G moiety, which would indeed give the expected chemical structure of Rh19, as it can be seen in Figure 4.4. The disintegration reaction could be described by the following scheme:

$$2\ \mathrm{Rh6G} \rightarrow 2\ \mathrm{Rh19} + \mathrm{Cl_2}\uparrow + \mathrm{C_4H_{10}}\uparrow$$

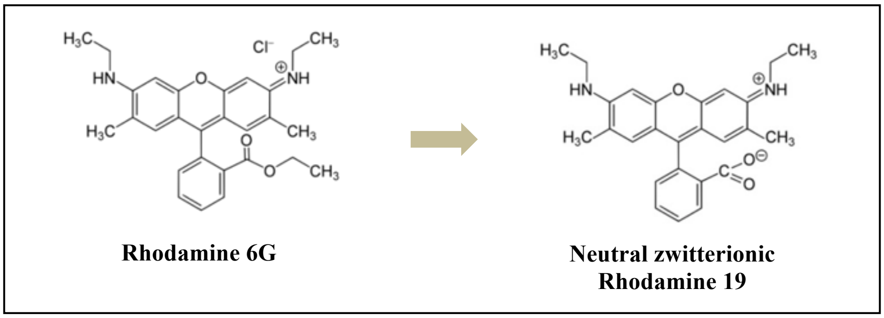

Figure 4.4 Structure of the Rhodamine 6G molecule (left) and its disintegrated form, neutral zwitterionic Rhodamine 19 (right).

During the transformation, the initial negative charge of the chlorine ion is conserved and reflected in the negative charge of the oxygen left from the transformation of the ester functional group. The neutral zwitterionic Rh19 is an inner salt, as it is called, hence maintaining the dipolar character of the initial Rh6G molecule.

These two thermal processes (dehydration and decomposition) are also confirmed by the DSC measurements displayed in Figure 4.5. Both processes are endothermic and non-reversible as was determined from full heating-cooling cycles (for better clarity, the cooling process is not shown in the figure).

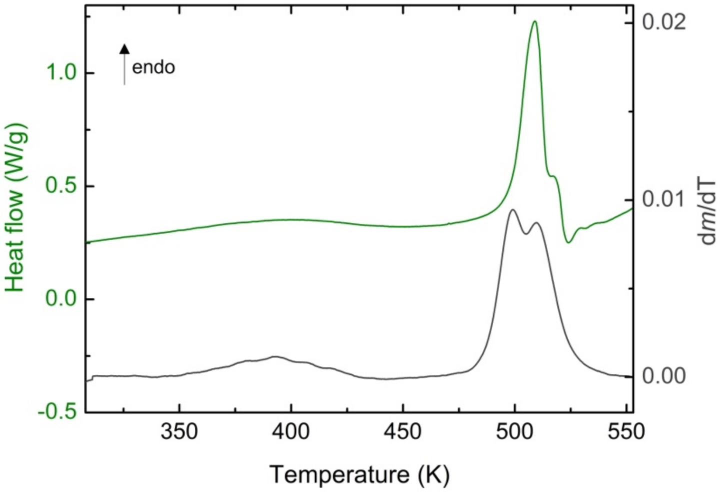

Figure 4.5 DSC thermograph (green curve, left axis) of the hydrated Rh6G sample and the first derivative of the TGA (grey curve, right axis). The temperature range is between room temperature and 550 K. The heating rate is 2 K/min.

The onset temperatures of the two endothermic features match the starting temperatures of each mass loss as measured by TGA. The first endothermic peak is rather broad and spans the whole temperature range of the first mass loss observed by TGA, thus corresponding to the dehydration process of Rh6G. A broad feature in DSC is typical for water desorption processes. Similarly, the second DSC feature (double peak) corresponds to the disintegration of Rh6G to Rh19. Both endothermic peaks have similar line shape and relative intensity of the corresponding features in the derivative TGA curve (Figure 4.5). By cooling from room temperature down to lower temperatures (230 K), we did not observe any sign of crystallization of water. This can be attributed to the lack of bulk-like water: in other words, the concentration of water is too low or water-substrate interactions and confinement within the Rh6G matrix are too strong, so that this hydration water is supercooled instead of crystallizing.

As mentioned previously, the broad and structured shape of the TGA dehydration peak is an indication of the existence of water molecules occupying distinct environments within Rh6G matrix (more or less strongly bound to the matrix) that desorb at different temperatures. Due to the small water content, the thermographs cannot give extra information about the different species. An infrared spectroscopic analysis is carried out to confirm the presence of water and the existence of distinct water environments (differently bound water is expected to display different vibrational features).

4.4 FT-IR characterization of Rhodamine 6G

The IR absorption spectrum of the Rh6G salt was measured by Fourier-transform infrared spectroscopy. The bond vibrations of the molecule absorb in the mid-infrared region (4000 ÷ 400 cm^{-1}). We have acquired two room temperature spectra: a first one on the as-stored powder (Figure 4.6), and a second one (Figure 4.7) after heating the powder above the temperature of dehydration (~440 K) according to the thermal analysis presented in the preceding section). After heating, neither the positions nor the intensities of the bond vibration peaks of the Rh6G molecule undergo any change. However, as one may expect, the characteristic bands of water vibrations display changes. Figure 4.6 depicts the mid-infrared spectrum of the hydrated sample. Different absorption peaks are visible, due both to vibrations of the xanthene backbone and of the functional groups, and to water contributions.

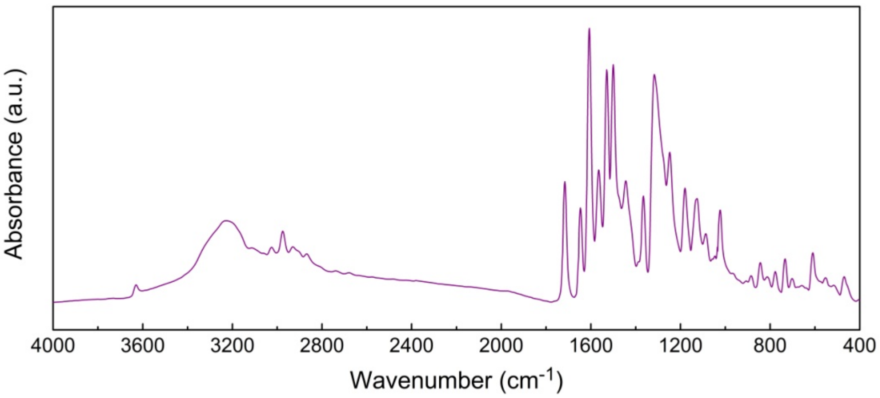

Figure 4.6 FT-IR spectrum of Rh6G at room temperature.

Above 3000 cm^{-1}, the stretching vibrations due to the amino groups of Rh6G (N-H) and the hydroxyl groups of water (O-H) overlap forming a broad band which extends from 3500 to 3100 cm^{-1}. The detection of O-H vibrations indicates the presence of water in the solid, as Rh6G does not contain any hydroxyl group. Four narrower peaks are observed at lower frequencies, namely at 3022, 2975, 2931 and at 2868 cm^{-1}. These bands correspond either to the C-H stretching vibrations of the xanthene backbone and of the phenyl, ethyl and methyl groups, or else are overtones and combination modes of the fundamental bond vibrations. Below 1800 cm^{-1} the spectrum exhibits yet narrower bands which are characteristic of the Rh6G unit. These absorption peaks give the ´´fingerprint´´ of the compound, as they correspond to the bond vibrations of the backbone and the functional groups of Rh6G, as previously reported.[2]

In order to confirm the presence of water inside the solid, in Figure 4.7 we zoom in on the broad FT-IR band between 3700 and 3100 cm^{-1}.

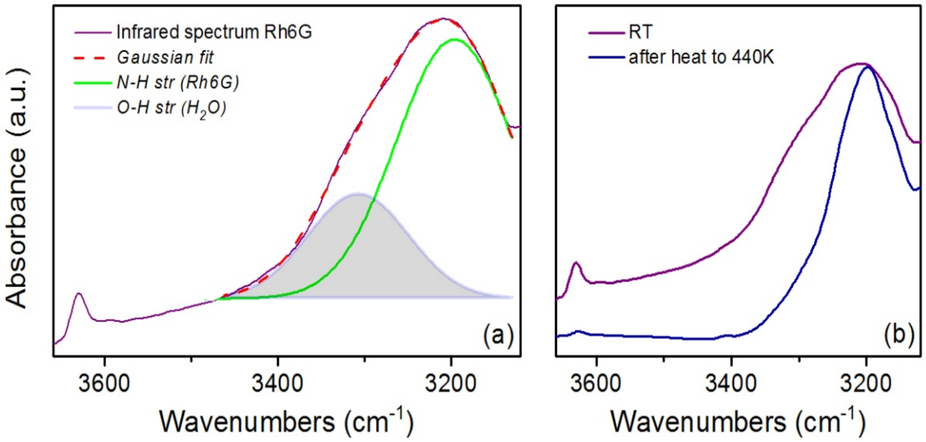

Figure 4.7 (a) FT-IR spectra in the 3700 – 3100 cm^{-1} spectral range, characteristic of O-H and N-H stretching vibrations. The peak at 3628 cm^{-1} corresponds to water vibrations (see the text). The experimental data (purple curve) between the frequencies 3450 - 3100 cm^{-1} were fitted (red dashed curve) as the sum of two Gaussian components corresponding to the characteristic bands of O-H (grey-filled area) and N-H (green curve) vibrations, respectively. (b) Comparison between the room-temperature FT-IR spectra of the as-stored powder (purple curve) and after heating it to 440 K (blue curve). The spectral range is the same as in panel (a).

Figure 4.7 (a) shows a Gaussian[a] fit of the spectrum of the hydrated powder with two components:[10] the first component (grey filled area) is centered about 3330 cm^{-1} while the second one (green curve) has a maximum at roughly 3200 cm^{-1}. The latter corresponds to the characteristic stretching vibration of the N-H bond[11] of the rhodamine unit. Instead, the grey-shaded area corresponds to the (covalent bond) O-H stretching vibrations of hydration water molecules in the powder.[12] This

---

[a] A Gaussian function (normal distribution curve) has the following analytical expression: $G(v) = \frac{A}{\gamma_0}\sqrt{\frac{4\ln 2}{\pi}}\, e^{\left[-4\ln 2\left(\frac{v-v_0}{\gamma_0}\right)^2\right]}$, where γ_0 is the full width at half maximum (FWHM), A is the area under the peak and v_0 is the wavenumber of the peak position.

is confirmed by comparison with the spectrum of the annealed powder, where this contribution is far less important (Figure 4.7 (b)). The large width of the O-H stretching vibration suggests a possible overlap of different sub-peaks, as it is for example known for the case of pure liquid water[12] and also for water inside different systems[13,14] (see also the next chapters). The substructures of O-H stretching vibration peak are normally three and are situated at the frequencies ~3600 cm^{-1}, ~3400 cm^{-1} and ~3200 cm^{-1}. Each one of these sub-peaks corresponds to O-H stretching vibrations of water molecules with different mean numbers of hydrogen bonds (i.e., different coordination numbers). Hydration water molecules can be hydrogen-bonded to different extents, hence leading to O-H vibrations at distinct frequencies and to band broadening. Different water environments may correspond to distinct hydration sites and/or to the presence of more than one hydration layer around the Rh6G crystallites. It is also important to note the existence of a relatively sharp peak at 3628 cm^{-1} in the IR spectrum. This component of well-defined frequency corresponds to the O-H stretching vibration of water molecules in a well-defined environment. Judging from the relatively high wavenumber of the vibration, these water molecules are poorly hydrogen-bonded to other molecules, thus forming small aggregates that are independent of the Rh6G matrix[13].

We point out that even a qualitative interpretation of the O-H stretching vibration peaks of neat liquid water and of water inside different systems, like porous materials,[15] clays[16] and water intercalated in graphite oxide[13] is in general quite complicated. Our data indicate that the hydrated Rh6G powder contains several types of water contributions. The main one is surface hydration water vibrating at relatively lower frequencies (~3330 cm^{-1}) and with a very wide distribution of environments (*e.g.* due to the presence of more than one hydration layers). The other one has a characteristic vibration at 3628 cm^{-1} and corresponds to water in a well-defined environment. It is observed that both components do not disappear completely upon heating to 440 K, although they undergo a significant reduction of intensity.

Given that all characterization techniques have confirmed the presence of water species inside Rh6G matrix, which moreover occupy non-equivalent sites, we performed an experimental study of the dynamic behavior of such water molecules by means of dielectric spectroscopy.

4.5 Broadband Dielectric Spectroscopy study

In this section, we study the dynamics of water inside Rh6G. Our goal is to identify common signatures of the dynamics of water molecules present in this molecular powder, as well as possible features that could differentiate the behavior of water in different molecular environments. Additionally, we report on two relaxation processes intrinsic to the Rh6G molecule. One of these relaxations is associated with interfacial polarization mechanisms (space-charge) within the material.

As a hygroscopic compound, Rh6G can capture and retain water molecules from the surrounding atmosphere, as it has been proven from the thermal and infrared analysis (see the previous sections), which also showed the existence of different water environments. Due to the dipolar nature of water molecules, their dynamic signature can be tracked by temperature-dependent broadband dielectric spectroscopy.

The dynamics of hydration water and of water confined inside porous or layered systems has been the subject of intense research in recent years. Several BDS studies have been carried out on aqueous mixtures, hydrated proteins and fibers[17,18] as well as on water inside nanoporous materials[15,19] and between adjacent sheets of layered materials[13]. In aqueous systems, the water molecules are involved in two types of relaxations, namely a collective (α-relaxation) process which corresponds to the cooperative re-orientation of the water-solute complexes, and a secondary (β) relaxation, whose exact origin is debated but which is thought to be due to local re-orientational motions of the water molecules. Instead, the water molecules inside porous materials and in-between the planes of layered materials relax without a direct involvement of the static matrix. In our system the water content is very small compared with aqueous solutions or fully hydrated systems, hence, we expect more local (rather than cooperative) motions of water molecules to take place. Moreover, we show that slow water-related relaxations can also have a conductivity origin.

We have performed dielectric studies on various Rh6G samples both upon heating and cooling. We found that the spectra of the as-prepared pellets at room temperature (RT) showed certain variability (in terms of the dc conductivity and of the position and dielectric strength of the loss features), due to the not fully controllable moisture content condensed onto the samples (Figure 4.8). Measurements carried out on various samples have proven that BDS shows extreme sensitivity to water, thus, even a small quantity of moist air condensed on the pellet can be detectable.

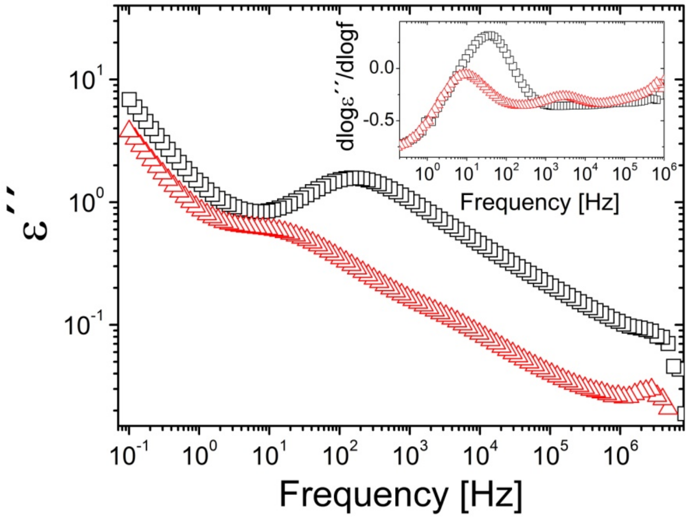

Figure 4.8 Dielectric loss spectra at room temperature (298 K) of Rh6G samples as-prepared directly from the bottle (red triangles) and after keeping a sample in humid atmosphere for 3 days (black squares). The inset shows the derivative spectra of the dielectric losses, in which the visibility of the peaks is enhanced.

We have chosen two spectra acquired at RT on two different Rh6G samples as examples showing how the preparation conditions (humidity) of the samples can affect the BDS signal (Figure 4.8). The spectrum with red markers was acquired on a pellet prepared directly with powder taken out from its storage bottle and characterized at room temperature (298 K) without any thermal treatment. The spectrum is characterized by two relaxation peaks lying on top of a conductivity-like background, one around 10 Hz and another one at a frequency a couple of orders of magnitude higher. Instead, when we prepared a pellet using a powder initially kept under humid atmosphere saturated with water vapor, the corresponding RT spectrum (black markers) displayed a single broad peak whose width covered three orders of magnitude. It may be seen that the position of the peak of the humid sample lies between the two peaks of the first studied sample, and its intensity is significantly higher than either peak. Water-saturated samples can indeed be expected to show a wider distribution of different relaxation times, as well as a higher signal level. It is interesting to point out that the humid sample shows higher dc conductivity values than the sample measured straight out of the bottle. A similar behavior was observed also in hydrated fullerene systems[5] (see also Chapter 5). An increase of the overall conductivity by exposure to humid air is in fact rather common in semi-conducting and insulating materials.[20]

Given that the samples are stored and prepared under normal atmospheric conditions with partial humidity, moisture adsorption cannot be avoided. As visible in Figure 4.8, the signal from secondary adsorbed water covers that of the water molecules that are incorporated in Rh6G under normal humidity, leading to a loss of information (for example, the existence of two different relaxations in the red curve is totally masked by the very broad feature in the black one, which has an extremely broad distribution of relaxation times). According to our thermogravimetric characterization, the first mass loss has an onset around 350 K and a maximum slightly below 400 K. As mentioned, this temperature is higher than the typical desorption temperature of condensed moisture (usually below 350 K), which indicates that the mass loss in Rh6G originates mainly from the loss of water molecules either within the organic matrix (interstitial water) or more tightly bound to it (what could be termed “interfacial” water). In the samples taken directly out of the bottle and measured without any previous thermal treatment nor exposure to humidity, we were able to identify three water-related relaxations, as shown below, two of which displayed reproducible characteristic times and temperature variation in different measured samples. The water content was generally calculated from thermogravimetric analysis on a minor portion of the sample, prior to dielectric measurements.

Figures 4.9 and 4.10 depict the typical temperature-dependent behavior of the hydrated Rh6G sample. The sample was initially cooled down to 168 K and spectra were then acquired isothermally by heating up to 440 K.

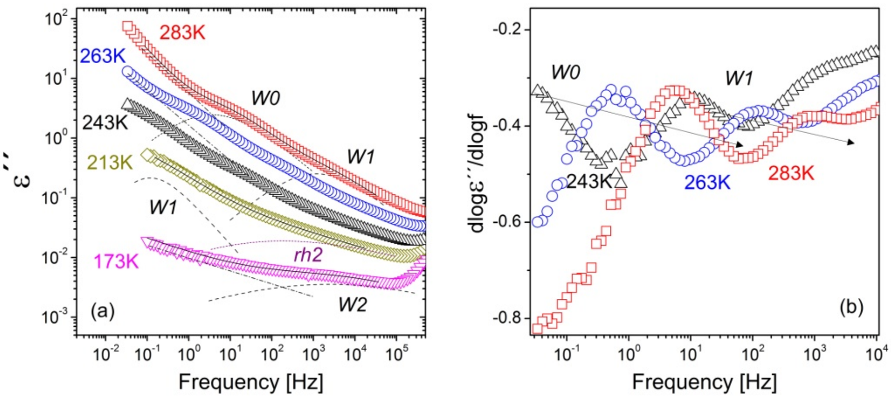

Figure 4.9 Dielectric loss spectra of hydrated Rh6G samples for selected temperatures between 173 and 283 K. The relaxations due to water molecules (labeled as W0, W1 and W2) and the intrinsic relaxation of Rh6G molecule (rh2) are shown. (a) Heat-up spectra from 173 K to room temperature. The solid lines through the data points of 173 K, 213 K and 283 K are fits of the loss peaks with Cole-Cole (dashed lines) and Havriliak-Negami (dotted lines) functions. The rh2 relaxation process (purple dotted line) at 173 K spectrum is displayed with a different color to distinguish it from the water-related relaxations. The loss peaks lie on a conductivity-like background depicted with a dashed-dotted line. (b) Derivative spectra of the dielectric loss for data at 243 K, 263 K and 283 K in order to better visualize the temperature evolution of the peaks.[21]

Figure 4.9 (a) shows the experimental data between 173 K and room temperature. At the lowest measured temperatures, a weak relaxation feature (labeled as W2) is observed at very high frequencies, accompanied at lower frequency by another relaxation, labeled as rh2, which as shown below is intrinsic to the rhodamine molecules. At higher temperatures (T > 200 K), one more peak enters the experimental window upon heating from the low frequency side. This peak, labeled as W1, is due to water. We label the processes intrinsic to Rh6G molecules with "rh" and those due to water with "W". Above 240 K, another feature, W0, enters the spectrum from the low-frequency side. The W0 feature is more than two orders of magnitude slower than the W1 one, and much more intense. Upon heating to room temperature, both W0 and W1 processes shift to higher frequencies as it is expected for normal dipolar relaxation peaks (Figure 4.9 (b)).

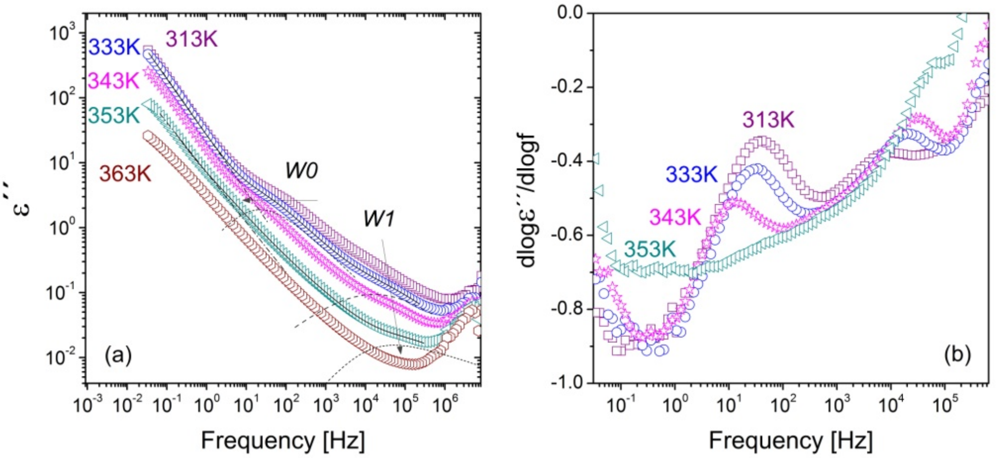

Figure 4.10 (a) Dielectric loss curves of hydrated Rh6G samples for selected temperatures between 313 K and 363 K. Two relaxations due to water molecules (W0 and W1) are visible, both of which display atypical temperature dependence. The solid lines that pass through the data at temperatures 333 K and 353 K are fits of the loss peaks with Cole-Cole (dashed lines) and Havriliak-Negami (dotted lines) functions. A low-frequency background proportional to inverse frequency is also added (dashed-dotted lines). (b) Derivative representation of the dielectric spectra at temperatures 313 K, 333 K, 343 K and 353 K, to enhance the visibility of the peaks.

However, this normal behavior is no longer observed above RT. Figure 4.10 (a) displays the dielectric spectra above 300 K, where it is seen that both features apparently stop shifting with increasing temperature, while at the same time their intensity undergoes a decrease. The W1 relaxation actually continues to shift slightly towards higher frequencies, but at a much slower rate than that below room temperature. Instead, the W0 feature is observed to shift to lower frequencies as the temperature increases, which is totally unexpected for a dipolar loss. While the W0 loss peak is no longer visible in the spectra above 350 K, W1 is detected up to 368 K. Figure 4.10 (b) depicts the derivatives of the dielectric losses to better visualize such anomalous behavior, which continues till 370 K.

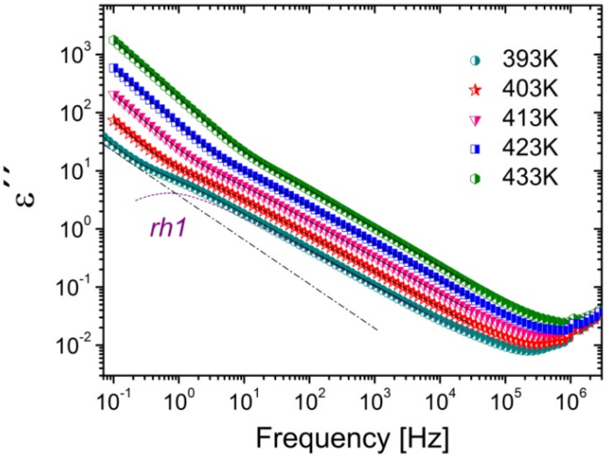

Figure 4.11 Dielectric loss spectra of Rh6G samples from 393 to 433 K, every 10 K. A new relaxation feature, rh1, intrinsic to the water-less rhodamine powder, enters the experimental window at higher temperatures. The black lines though the data are fits assuming a single loss feature (Havriliak-Negami) on top of a conductivity background. The loss peak (purple dotted line) and the conductivity background (black dashed-dotted line) are shown for the spectrum at 393 K.

Above 370 K, the W0 and W1 processes are no longer observed in our experimental range. However, another feature enters the spectrum above 390 K, as it is depicted in Figure 4.11. The new feature, called rh1, shifts normally with temperature in the studied range. The rh1 relaxation is an intrinsic dynamic process of the Rh6G molecules, as it will be discussed in the next section of this chapter.

In Figure 4.12, we present a relaxation map (Arrhenius plot) of all five dielectric losses measured upon heating and discussed so far, namely the rh1 and rh2 features that are intrinsic dynamic processes of the Rh6G molecules, and the W0, W1 and W2 features related to water moieties. It is uncommon to observe so many relaxations in a relatively simple system and small temperature range. In what follows, we deepen our analysis of such rich dynamic behavior.

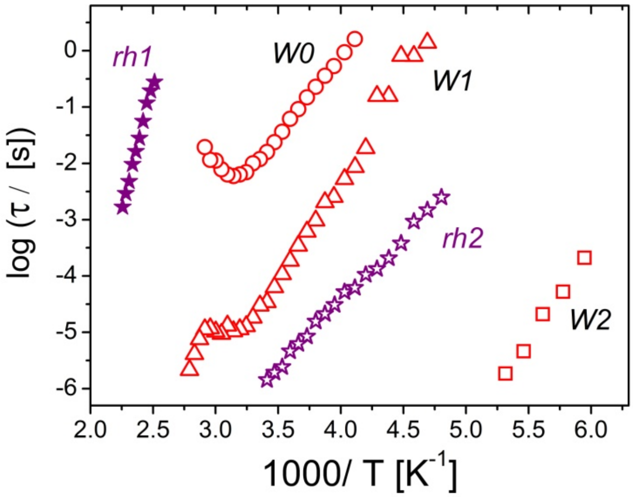

Figure 4.12 Relaxation times of the water-related processes (W0, W1, W2) in hydrated Rh6G and the intrinsic processes to Rh6G molecule (rh1, rh2) as a function of reciprocal temperature. The temperature interval is between 168 and 440 K. Rh6G-inherent relaxation processes are depicted in purple and water-related ones in red.

4.6 Dielectric Relaxations intrinsic of Rhodamine 6G

As discussed in Section 4.1, Rh6G possesses a dipole moment and may therefore display relaxations of its own. Indeed, we detected two relaxation processes that can be considered intrinsic to the Rh6G powder: one of them is due to the reorientational motions of Rh6G molecules (rh2) and is visible in between W1 and W2 water processes (Figure 4.12), while the other one is visible only at high temperatures (rh1) and, as we will show below, is related with the accumulation of charges at the sample´s heterogeneities within the material. These two relaxations are present at dielectric spectra of Rh6G in both heating and cooling processes, which shows that they are indeed intrinsic to rhodamine. Since Rh6G is a polycrystalline powder, the rh2 process must be a purely orientational relaxation dynamics (such as those found in some orientationally disordered molecular crystals (see Chapter 1)). Figures 4.9 and 4.11 depict dielectric loss data of Rh6G upon heating, where both relaxations are present. Both rh1 and rh2 features are characterized by Havriliak-Negaki line shapes, with shape parameters $0.75 < \alpha_{HN} < 0.81$ and $0.65 < \beta_{HN} < 0.83$ for rh1 and $0.82 < \alpha_{HN} < 1$ and $0.26 < \beta_{HN} < 0.62$ for the rh2 loss peak. The dielectric strength of both relaxations tends to increase slightly upon heating. We show here that rh1 is a space-charge loss, while rh2 appears to be a dipolar process intrinsic to the Rh6G molecule.

The fact that rh1 and rh2 relaxations are intrinsic of the water-less Rh6G sample was also proven by a BDS study on Rh6G thin films.[22] The authors of reference 28 deposited water-free Rh6G films on a silicon substrate by two different methods: film grown from ethanol solution (film thickness ~ 130 nm) and vacuum-deposited films by thermal deposition (film thickness ~ 300 nm). Two relaxations were observed in such Rh6G films, which, as visible in both panels of Figure 4.13, show some similarities to the relaxations rh1 and rh2 of the pellets. The low temperature (rh2) relaxation is absent from the dielectric loss spectra in the case of the vacuum deposited films. This was ascribed to the absence of the chlorine ions due to the elevated temperatures used in the thermal deposition. In fact, we have shown in Section 4.3 that at temperatures higher than 483 K the Rh6G compound disintegrates into another molecule of the rhodamine family, namely the neutral zwitterionic Rhodamine 19. The Rh6G disintegration is accompanied by the loss of the chloride ion (see section 4.3), while the dipolar nature is preserved. It is therefore natural to assign the low temperature rh2 relaxation to a dipolar dynamics involving the nitrogen atom and the chlorine counter-ion. It is not known whether Rh6G has any orientationally disordered phase in the studied temperature interval, hence the extent of the cooperativity of the rh2 relaxation cannot be ascertained.

The low temperature (rh2) relaxations of Rh6G from our study of the bulk form are compared with those of the Rh6G chloride films in Figure 4.13 (b). It is seen that the low temperature rh2 relaxation is affected not only by the sample characteristics, but also by the presence of water. The activation energy (slope) of rh2 in the hydrated bulk sample (0.5 eV) is higher than that of the water-less bulk sample (0.4 eV) obtained by heating the former to 440 K. Both activation energies are larger than that in the film. The sensitivity of the fast rh2 dynamics to the water content can be rationalized remembering that it stems from a local motion involving the charged nitrogen and chlorine species, which are prone to interact with water molecules. The activation energy of the rh2 process is lowest in the thin films, which may be ascribed to both the absence of water and to the looser intermolecular environment of the film (due e.g. to a more disordered structure, or to strain induced by interaction with the substrate). Both a looser local environment and the lack of water in the films would in fact lead to weaker intermolecular interactions and thus to a lower activation barrier for the dipolar process rh2 to occur.

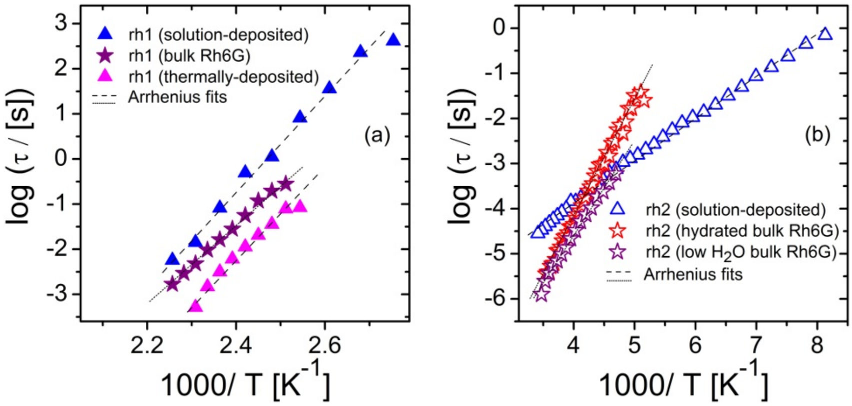

Figure 4.13 Relaxation times of rh1 (a) and rh2 (b) processes due to Rh6G molecules both in the bulk sample (pellet) and in thin films, as a function of reciprocal temperature. In panel (a), purple stars correspond to data acquired on a pellet, pink triangles to a thermally-deposited film and blue triangles to a solution-deposited film[22]. In panel (b), purple empty stars correspond to water-less pellet while red empty stars to a hydrated sample. The dashed and dotted lines through the linear part of the data are the Arrhenius fits of the rh2 relaxation in Rh6G thin film and bulk form relaxations, respectively.

The Arrhenius plot of the high temperature (rh1) dielectric process of the bulk sample deviates slightly from the linear behavior. The curvature of rh1 relaxation time is slightly negative, as it can be observed in Figure 4.13 (a) (see also below). An Arrhenius plot with such curvature cannot correspond to a dipolar relaxation.[23] The rh1 dielectric relaxation is instead associated with the charge transport process within the (pure) rhodamine salt. In order to show such correlation, we first analyze the temperature dependence of dc-conductivity of the anhydrous Rh6G sample (water on the sample's surface can introduce new (non-intrinsic) mechanisms for charge transport, as we will see later). Figure 4.14 (a) shows the real part of the complex ac conductivity spectra of Rh6G at high temperature, where the sample is basically anhydrous. We extracted the dc-conductivity (σ_{dc}) values from the low frequency ($f \rightarrow 0$) plateau of the ac spectra (see chapter 2). The temperature dependence of σ_{dc} is depicted in Figure 4.14 (b).

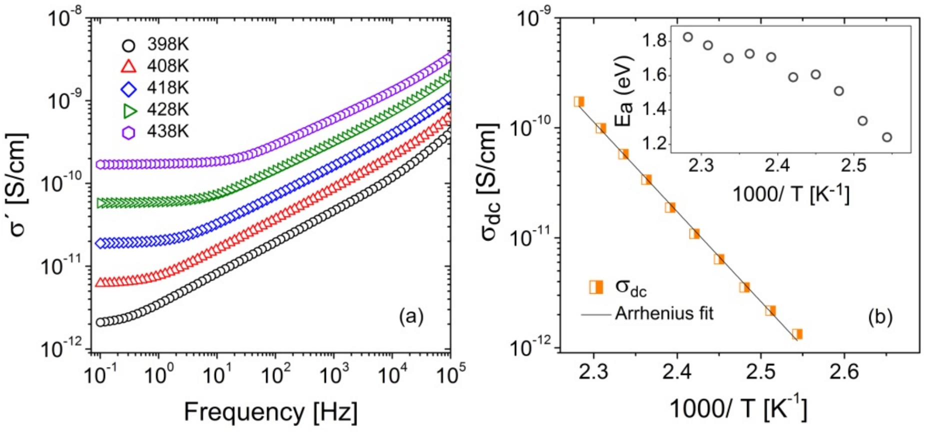

Figure 4.14 (a) Logarithmic plot of ac conductivity (σ´) at various temperatures upon heating from 398 to 438 K. (b) Arrhenius (semi-logarithmic) plot of the σ_{dc} conductivity, extracted from the data of the (a) plot. Inset: Activation energy of σ_{dc} as a function of the inverse temperature.

The σ_{dc} value increases with increasing temperature, implying that the conductivity is thermal-assisted, as it is commonly the case in semiconducting materials. The dc-conductivity plot appears to have a slightly positive curvature (Figure 4.14 (b)). This is visible from the fact that it cannot be fitted perfectly with an Arrhenius function, or, in a visually more compelling way, from the plot of its effective activation energy[24] of the dc conductivity (inset of Figure 4.14 (b)). The activation energy is defined as the first derivative of the σ_{dc} plot, namely as $E_a(\sigma_{dc}) = -\frac{d\,(\ln\sigma_{dc})}{d(1/k_BT)}$, where k_B is the Boltzmann constant. E_a is seen to increase upon heating, which shows that the temperature dependence of σ_{dc} is not simply activated but it is actually sub-Arrhenius. This is consistent with a hopping electronic conduction mechanism. Hopping conduction of electronic charge carriers is the most common conduction mechanism in disordered organic semi-conductors.[25] A study of another dye of the rhodamine family (Rhodamine B) has reported the existence of a similar (electronic) hopping-mediated conduction in pellets made with this dye.[26]

Figure 4.15 (a) shows the comparison, in the same Arrhenius plot, between the frequency (f_{max}) of maximal loss of the rh1 process ($f_{max}(rh1) = 1/2\pi\tau_{rh1}$) and σ_{dc} (both vertical scales in Figure 4.15 (a) span the same number of decades). The experimental curves of both quantities are virtually the same, and both display positive curvature, although the profile of the frequency relaxation process is a bit nosier.

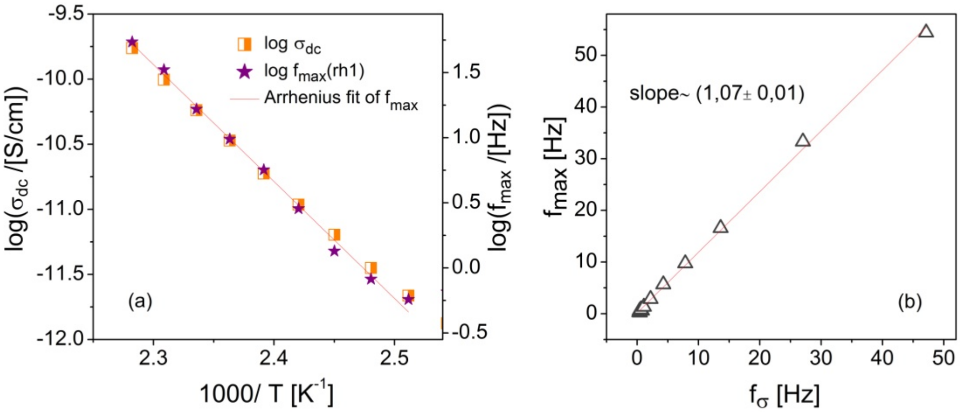

Figure 4.15 (a) Arrhenius plot of the dc conductivity (σ_{dc}) compared with the relaxation frequency (f_{max}) of the rh1 process, in the temperature range between 398 and 438 K upon heating. (b) Linear plot of the relaxation frequency of rh1 process (f_{max}) versus the characteristic relaxation frequency (f_σ) of spatial charge fluctuations (see text) for the same temperature interval.

To substantiate our analysis, we introduce another characteristic frequency, f_σ, which is defined, for each temperature, as

$f_\sigma = \sigma_{dc}/2\pi\varepsilon_0\Delta\varepsilon(\mathrm{rh1})$, where ε_0 is the vacuum permittivity and σ_{dc} and $\Delta\varepsilon$(rh1) are respectively the dc conductivity value and the dielectric strength of the rh1 dielectric loss at that temperature. The frequency f_σ is the characteristic relaxation frequency of spatial charge fluctuations in a weakly conducting medium.[27] A linear dependence is found between the characteristic frequencies of process rh1 (f_{max}) and that of space-charge fluctuations (f_σ), with a slope of almost unity (slope ~ 1.07, see Figure 4.15 (b)). This entails that f_{max} is directly proportional to f_σ, which confirms the correlation of the rh1 dielectric loss with the long-range conductivity. The simplest explanation of the conductivity-induced loss feature rh1 is the accumulation of electronic charges on the interfaces of grain boundaries, where the dc conductivity changes abruptly. Indeed, the powder nature of the sample and the loss of water molecules from the solid above 393 K are expected to result in spatial heterogeneities, where electronic charge carriers are blocked leading to free-charge polarization effects.

4.7 Analysis of the H_2O dynamics inside Rh6G

All three water relaxations are non-Debye, entailing the existence of a distribution of distinct relaxation times, as it may be expected in a hydrated organic matrix. The faster W2 relaxation has the lowest dielectric strength, and due to its low signal and its relatively high frequency it can only be followed in a small temperature window. It is modeled with a Cole-Cole function with an exponent in the range $0.26 < \alpha_{CC} < 0.29$. The W1 relaxation was also modeled with a Cole-Cole function with a value of the exponent between $0.45 < \alpha_{CC} < 0.73$, except for temperatures T > 338 K (deviations are observed especially approaching water desorption). Conversely, the W0 process is characterized by a Havriliak-

Negami line shape with exponents ranging between $0.70 < \alpha_{HN} < 0.98$ and $0.82 < \beta_{HN} < 1.00$. The shape parameters of all three features do not depend strongly on temperature and only deviate for temperatures around 350 K, where the relaxations W0 and W1 start to disappear gradually.

	Fit function	$\Delta\varepsilon$	α	β
W2	Cole-Cole	0.029-0.032	0.26-0.29	—
W1	Cole-Cole	0.62 -0.07	0.45-0.73	—
W0	Havriliak-Negami	10.17-1.27	0.70-0.98	0.82-1.00

Table 4.1 Fitting parameters for the three water relaxations W2, W1, W0.

The values and temperature dependence of the fit parameters (dielectric strength, exponents) of the relaxations can shed light on their origin. Secondary relaxations of glass-forming systems[28] and water relaxations in aqueous and hydrated systems[17,29] are commonly fitted with symmetrical Cole-Cole functions, while Debye line shapes are usually observed for Maxwell-Wagner or space-charge relaxations.[28] The modeling parameters of the three water-related processes in Rh6G are summarized in Table 4.1. The W2 relaxation process is characterized by the smallest dielectric strength ($\Delta\varepsilon$) (see Figure 4.16 (a)) of all three water-related relaxations. W0 shows the highest $\Delta\varepsilon$ values, which are in fact almost a decade higher than that of W1, as it can be observed in Figure 4.16 (b). The large dielectric strength of the W0 process suggests that it is not a truly dipolar process of water molecules in Rh6G, as it will be shown in more detail later.

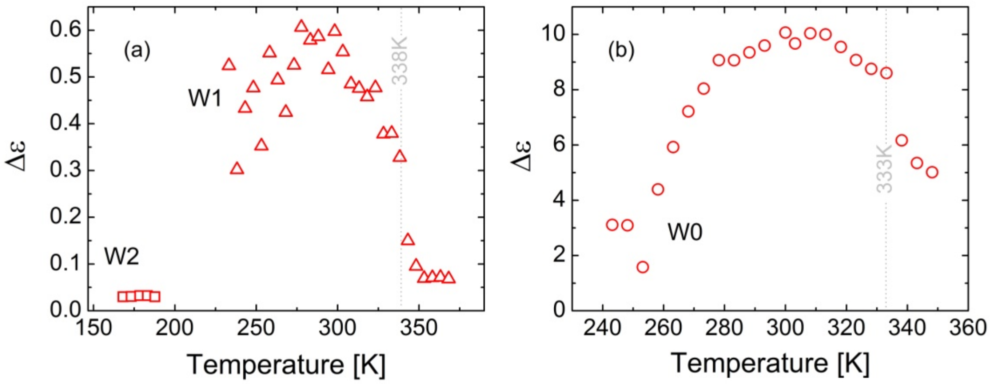

Figure 4.16 Temperature dependence of the dielectric strength ($\Delta\varepsilon$) of the W2 and W1 (panel (a)) and W0 (panel (b)) relaxation peaks, upon heating from 168 K to 360 K.

For T < 300 K, the $\Delta\varepsilon$ value of W0 displays more pronounced temperature dependence than those of the W2 and W1 relaxations. The dielectric strengths of W1 and W0 display a maximum around 300 K, as visible especially for the latter in Figure 4.16 (b). Above 313 K, the dielectric strengths of W1 and W0 start to decrease slightly. At approximately 350 K, the $\Delta\varepsilon$ of the W1 relaxation reaches an almost constant value ($\Delta\varepsilon \approx 0.070$), and maintains a constant intensity at least until exiting the experimental window. The vanishing intensity of the W1 and W0 peaks above the main dehydration process clearly indicates that their origin is associated with the presence of water molecules.

The relaxation times as a function of the reciprocal temperature (Arrhenius plot) are presented in Figure 4.17 for the W2, W1 and W0 relaxations. The dashed lines that pass through the (roughly) linear parts of the three plots correspond to the Arrhenius fits for each loss feature. From the slopes of these fits, one can determine the activation energy (E_α), which is the energy barrier associated to a given process.

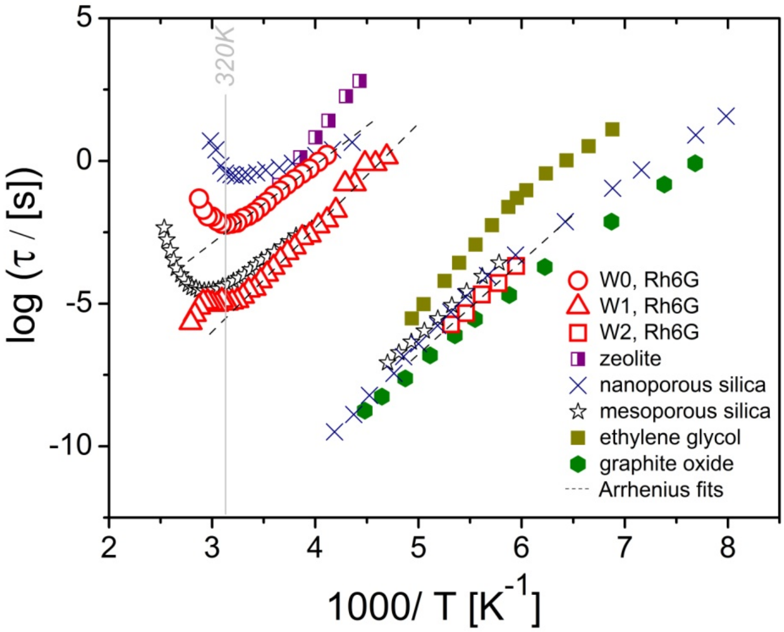

Figure 4.17 Relaxation times of W2 (red squares), W1 (red triangles) and W0 (red circles) processes in hydrated Rh6G as a function of reciprocal temperature. The dashed lines are Arrhenius fits of a portion of each data set. For comparison, we plot also the data for other hydrated systems, namely water confined inside mesoporous silica with a pore size of 50-70 nm,[15] water inside nanoporous silica MCM-41 with pore size 2.1 nm,[19] water inside zeolite,[30] an aqueous solution of ethylene glycol[31] and water intercalated between graphite oxide layers.[13]

The activation energies for the simply-activated portions of the W2, W1 and W0 processes are respectively E_α (W2) = 0.65 ± 0.15 eV (62.2 kJ/mol), E_α (W1) = 0.73 ± 0.12 eV (69.8 kJ/mol), and E_α (W0) = 0.49 ± 0.10 eV. These values are in line with the reported activation energy of dipolar losses in other water-containing systems.[32,33] In particular, they are close to the value of 50 kJ/mol (0.53 eV) which represents the energy needed for the cleavage of two hydrogen bonds per water molecule (which supposedly allows for translation or rotation motions of the water molecules to occur). Also the activation energy of the dipolar relaxation in bulk ice, which is related to the diffusion of orientational defects throughout the hydrogen-bond network, has been found to be around 53 kJ/mol above 230 K.[34,35,36,37] The similar activation energy values compared to the water-related relaxations in other water-containing systems is another indication that these dielectric processes involve water species. We will show in what follows that the W0 process is indeed affected by water, but that its origin is a space-charge effect. It is worth noticing that the W1 and W2 relaxations are observed also at temperatures lower than 238 K (T_{cryst} of water), in the supercooled region of water, and that the W0 feature is visible above 240 K. This confirms that the water molecules present in Rh6G do not undergo any crystallization.

In Figure 4.17, we compare directly the Arrhenius plots of the W2, W1 and W0 relaxations with those of other hydrated systems. The values of the activation energy and the high temperature limit of the relaxation times are summarized in Table 4.2 for all the water-related processes in Rh6G. As it can be gathered from Figure 4.17, the fastest (W2) relaxation lies in the neighborhood of the single-water-molecule relaxation found in all water-containing systems and commonly known as the “secondary relaxation” or “β relaxation” of water.

The broad and symmetric shape (Cole-Cole) of the W2 relaxation is also characteristic of the β relaxation of water, as is the slight increase of the dielectric strength with temperature.[32] Because the water molecule does not have intra-molecular relaxation modes, this β water-relaxation is a whole molecule relaxation. Based on the similarity of relaxation behavior, we extend the same interpretation to the W2 relaxation in Rh6G. The extrapolation value of the W2 relaxation time at infinite temperatures

($\log(\tau_\infty$ (s)) ≈ -23) gives an attempt time that is incompatible with a reorientational dynamic process, as $\log(\tau_\infty)$ should, in such case, be close to ≈ -15 – -14. This discrepancy, which is a common feature of the β relaxation of water also in other hydrated systems, suggests the existence of a change in the temperature dependence of the relaxation time at higher temperatures. Many interpretations of this “cross-over” have been proposed.[13,32,38] We cannot observe a similar cross-over in our data due to the smaller frequency range of our experiments, but we argue that, at higher frequencies than studied here, a similar dynamical cross-over should be visible at high temperature for the W2 relaxation.

Especially in the case of aqueous solutions, some authors have argued that the single-molecule β relaxation of water is a “precursor” of a collective water-solute (α) relaxation in several water-containing systems.[32] In the case of Rh6G, this does not appear to be the case: we show below that the W0 relaxation has a space-charge origin, and the W1 relaxation is unlikely to be a simultaneous relaxation of water and Rh6G molecules, given that the Rh6G molecules themselves display two other relaxations. Moreover, we have checked that the so-called Coupling Model,[28] often used to identify precursor relaxations, does not hold for the W1 and W2 relaxation (not shown).

	E_α (eV)	$\log(\tau_\infty$ / sec)	Interpretation
W2	0.65 ± 0.15	-23.1 ± 0.8	“β-relaxation” of the hydration water
W1	0.73 ± 0.12	-16.9 ± 0.3	Dipolar relaxation of the boundary water molecules (restricted mobility)
W0	0.49 ± 0.10	-9.9 ± 0.2	Space-charge effect due to the proton carriers at sample’s boundaries

Table 4.2 Fitting parameters of the Arrhenius plots of the three water relaxations, and their interpretation.

We now turn to the W1 and W0 relaxations. As it can be seen in Figure 4.17, the W1 and W0 processes have significantly longer relaxation times than all β relaxations of water in hydrated systems. Instead, the comparison with water confined inside silica nanopores[15,19] in the same figure shows that the latter systems exhibit relaxations with characteristic times and temperature behavior that are quite similar to those of the W0 and W1 relaxations in Rh6G. These similarities suggest that the relaxations of these systems could share a common origin. It is found that, in water-containing porous silica, two main relaxations are observed, one corresponding to the W2 process (β relaxation of water), and the other displaying non-monotonic temperature dependence as both W0 and W1. The authors of reference 15, for example, have identified two relaxations which they assign to water re-orientational motions inside silica pores (with pore diameter of 20-50 nm). The faster one, which according to this study corresponds to single water molecule re-orientation at the center of the pore, is observed to lie next to W2 relaxation. Instead, the slower relaxation inside the pores lies near W1 relaxation and would be associated with water molecules forming clusters onto the pore surface. Both the faster and slower processes appear to be affected by the proximity of the pore surface. Inside silica pores with smaller pore diameter (~2.1 nm) two water relaxation process are also observed (at low hydration levels).[19] While the fast relaxation overlaps with the W2 feature in Rh6G, the slow process is this time closer to the W0 relaxation, as it is seen in Figure 4.17. This latter relaxation is due to charge accumulation on the surface of the pores, according to reference 19.

Similar relaxation dynamics are observed for water confined in other inorganic porous materials,[39] albeit with different relaxation times. Pore size and confinement geometry appear to play important roles for the dynamic properties of water inside the pores.

The similar activation energy of both W2 and W1 relaxations despite their very different relaxation times suggests that the rotators responsible for the W2 and W1 features have similar environments. While the W2 process (water β-relaxation) corresponds to single-molecule dynamics, the W1 might have a more cooperative character and involve more water molecules at once. The value of τ_∞ that we obtained for the W1 relaxation would be consistent with a dipolar molecular origin (see Table 4.2). This is not the case for the W0 relaxation, whose origin is likely a space-charge effect, in agreement with reference 19.

Another possible interpretation for the existence of two dipolar relaxations (W2 and W1) associated with water species is that the molecules that participate in the (slower) W1 process are located closer to the Rh6G grains while those that participate to the (faster) W2 process belong to higher hydration layers. Water inside Vycor glass shows for example a double relaxation behavior.[40] The two processes, at lower and higher frequency, are reported to correspond to water molecules onto the surface of the pores (restricted mobility) and closer to the pore center, respectively. A similar behavior of confined water has been found in a molecular dynamics simulation study.[41] Based on this comparison between hydrated Rh6G and other porous materials, we assign the W1 relaxation process to the re-orientational motion of hydration water molecules interacting directly with the Rh6G grains, *i.e.*, in the first or second hydration layers. The strong binding to the organic matrix helps explaining the longer relaxation times of the W1 relaxation, unlike the faster times of W2 process.

The Cole-Cole fitting of W1 relaxation feature yields the characteristic exponent α_{CC} of the process, whose value is related to the spectral width and is known to depend on the structure, the composition and the physical parameters of the sample.[42] The interdependence between the Cole-Cole exponent and the relaxation times can give information about the interactions between the relaxing dipoles with their surroundings.[43] In particular, two opposite trends (increasing and decreasing) of the α_{CC} exponent have been reported as a function of the characteristic time τ, for example for water inside porous silica[15] and for mixtures of polymer and water.[44] The plot of α_{CC} against the natural logarithm of τ is displayed in Figure 4.18 for the W1 relaxation. The positive slope of the plot supports the idea of a direct interaction of water with the organic matrix, confirming an interpretation of the W1 feature as arising from the interfacial water molecules (first hydration layer).

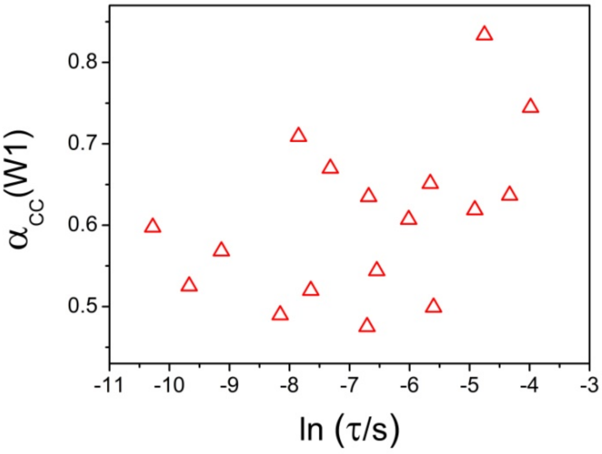

Figure 4.18 Dependence of the Cole-Cole α_{CC} exponent on ln(τ) for the W1 water relaxation in Rh6G, in the temperature range between 238 and 288 K.

In order to further confirm the origin of both relaxations (W2 and W1), we acquired dielectric spectra on another Rh6G pellet, this time made from powder pre-heated to ~343 K (near the onset temperature of dehydration, see Figure 4.3) during 6 hours. The water molecules that remain within the sample after the annealing must be strongly bound to the organic matrix. Dielectric spectra were then acquired isothermally upon cooling to 160 K and upon reheating to high temperature (not shown). The W0 and W2 relaxations were absent, and only the W1 relaxation was detected. Furthermore, we observed that the W1 relaxation had significantly lower intensity with respect to the non-annealed samples. This shows that by heating the sample close to the dehydration point we can get rid of the weakly bound water (which apparently gives rise to the W0 and W2 features) and of some of the water molecules more strongly bound to the grain surface (W1), thus corroborating the origin of the relaxations.

4.7.1 Atypical temperature-dependence of water-related dynamics

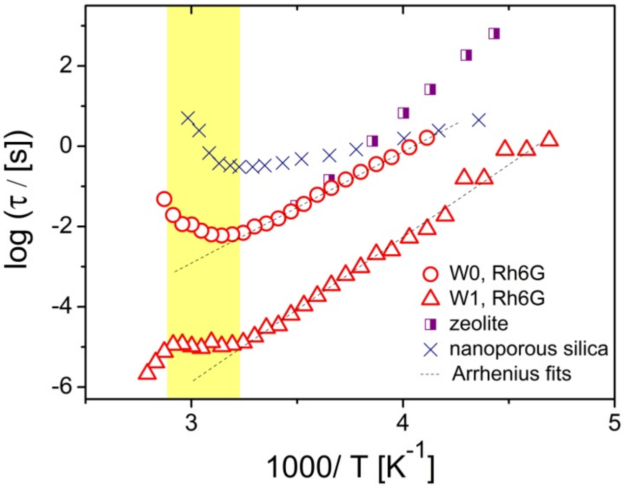

Figure 4.19 Arrhenius plot of the relaxation processes W0 (red circles) and W1 (red triangles) in hydrated Rh6G. The atypical shift of W0 at longer times upon heating is compared with the saddle-like Arrhenius plot reported for water confined in nanoporous silica[19] and inside a zeolite.[30] The black dashed lines, which pass through only a portion of our data, are Arrhenius fits.

Figure 4.19 shows in more detail the atypical Arrhenius behavior of W0 and W1 relaxations. As directly visible also from the loss spectra (see Figure 4.10), but more clearly in the Arrhenius plot, the W1 relaxation does not follow the normal temperature dependence expected for the characteristic relaxation time of a dipolar process, but actually shows a “deceleration” between approximately 313 and 348 K. During such “decelaration”, its dielectric strength drops down abruptly indicating the loss of water molecules participating in W1 process. The decelaration in its relaxation rate can be seen clearly from the almost horizontal slope of the Arrhenius plot between 313 and 343 K (Figure

4.19). The deceleration and simultaneous reduction in strength may be rationalized in the following way. Since the dielectric loss feature of the W1 relaxation has a non-Debye profile, it can be thought to contain various components at slightly different relaxation times, as depicted in the schematic representation of Figure 4.20 (a). Such (Debye-like) components correspond to the slightly lower or higher relaxation frequencies of water molecules attached more or less strongly onto the surface of Rh6G grains (the stronger the bond, the lower the frequency). Upon heating, the more weakly bound water moieties, which are more labile, will desorb first, resulting the loss of the high-frequency peak components entailing a narrower and less intense peak. The remaining peak components would correspond to water moieties more strongly bound on the material´s grains and thus displaying lower relaxation frequency than the former species (Figure 4.20 (b)). This mechanism, if true, would explain why the average relaxation time of the W1 feature does not vary upon water desorption (between 313 and 348 K). After the loss of the W0 relaxation, the W1 relaxation times occur to shift normally by further heating until exiting the experimental window (~ 368 K).

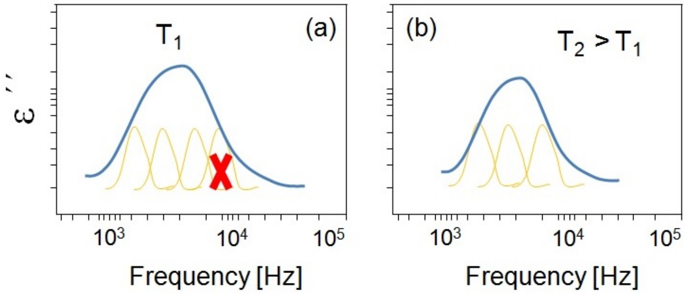

Figure 4.20 Scheme of the dielectric loss components contributing to the W1 relaxation at two different temperatures (a) T_1, and (b) $T_2 > T_1$, in the temperature interval from 313 to 348 K.

Figure 4.19 also shows the atypical Arrhenius behavior of the W0 relaxation. The anomalous slowing down of the W0 process occurs at a temperature around ~313 K and it lasts till 348 K, temperature at which its intensity shows a sudden decrease (see Figure 4.16 (b)). The relatively low temperature of desorption (330 K) of the water moieties associated with this W0 feature, indicates weak physisorption onto Rh6G. The anomalous shift of the W0 feature cannot be explained only from the loss of the physisorbed water as we have done for the W1 feature. Moreover, the high dielectric strength, the slow characteristic time and attempt time of the W0 process are, as already mentioned, inconsistent with a molecular reorientation process. In fact, a saddle-like atypical behaviour of a water-related loss feature was observed also in other hydrated porous systems.[15,19] The origin of this effect has been the object of controversy: it has been related either to a reduction of the available free volume per defect in the hydrogen-bond network of interstitial water upon heating[45] or to a Maxwell-Wagner-Sillars polarization effect due to the strong decrease of the static permittivity of a porous sample when water desorbs from its inner surfaces.[19] The scenario of the reduction of free volume does not appear to apply to the case of W0 relaxation process, due to the coincidence of this atypical behavior with the decrease of its dielectric strength upon water desorption (moreover, by pre-heating the samples at 343 K for 6 hours the W0 relaxation process does not appear in the measured spectra, as already mentioned). Instead, a strong modification of the Maxwell-Wagner Sillars polarization can result from water loss, because water not only has a high dielectric constant, but also because its presence introduces the possibility of new conduction paths and mechanisms. In Figure 4.19 a striking similarity is observed between the W0 characteristic times and those of water in hydrated nanopores[19] and inside zeolite.[30] The latter relaxations are both caused by charge accumulations at grain boundaries or pore surfaces. A recent study on a hydrated fullerene derivative has shown a similar situation[4]: these authors have found an anomalous shift of the delectric loss, which matches perfectly the strong decrease of the sample´s conductivity upon desorption of surface hydration water.

In order to study the exact origin of the W0 relaxation, we compare the temperature dependence of the W0 relaxation frequency ($f_{max}(W0) = 1/2\pi\tau_{W0}$) with that of the long-range conductivity (σ_{dc}) upon heating a hydrated sample between 280 and 350 K. Such comparison is shown in Figure 4.21 in the same Arrhenius plot (both vertical scales span the same number of decades). The conductivity values were extracted from the low frequency plateau of the complex conductivity spectra, as explained in relation with the rh1 loss in anhydrous Rh6G (see section 4.6). Although the value of σ_{dc} is not truly reliable, as at the relatively low temperatures where the W0 process is observed the low frequency plateau of the conductivity spectra of hydrated Rh6G is not really measurable, the temperature dependence of σ_{dc} should be reliably mimicked by that of the σ' curve at the lowest measured frequency (0.1 Hz). It is seen in figure 4.21 that the dc conductivity shows, upon heating, first an increase at low temperatures, and then an anomalous decrease above 323 K. The behavior of σ_{dc} is almost identical to that of the W0 feature. An identical correlation of conductivity and relaxation times has been reported in reference 5 for a fullerene derivative. The origin of this behavior is the well-known conductivity enhancement generated by adsorption of water on semi-conducting and insulating materials. Exposure of poorly conducting materials to humid air introduces new mechanisms for charge generation and transport, which may result in an increase of the overall conductivity by several orders of magnitude.[20,46] The conductivity mechanism induced by water molecules is debated, but the most likely candidate is proton exchange in the hydrogen-bonded network.[47] Hence, we ascribe the W0 relaxation to a space-charge effect due to proton carriers accumulating at sample's heterogeneities such as grain boundaries (protons can shuttle through hydration layers but not through the rhodamine grains). In other words, the W0 is analogous to the rh1 dielectric loss in the anhyndrous material, which is also a space-charge relaxation, only due to electronic charge carriers and not protonic as in the W0 process. The saddle-like behavior upon desorption of water is due to the strong decrease (and finally disappearance) of proton conduction through the physisorbed water.

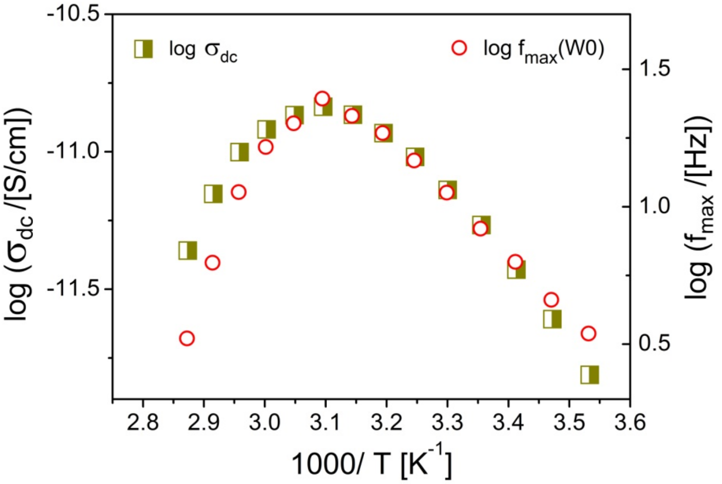

Figure 4.21 Arrhenius plot of the dc conductivity (σ_{dc}) compared with the characteristic frequency (f_{max}) of the W0 process, in the temperature range between 283 and 348 K upon heating.

4.7.2 Space-charge relaxation in quasi-anhydrous Rh6G

After the characterization of the Rh6G pellet upon heating to 440 K, we carried out BDS measurements on the same sample (which is, in principle, fully dehydrated) upon cooling down from 440 K. The spectra measured upon cooling are shown in Figure 4.22 (a). Two loss features are observed at high temperatures, and another one enters the experimental window below 290 K. Since the high temperature peaks are masked by the conductivity background, in the inset to Figure 4.22 (a) we have plotted the ε''_{rel} spectra defined as $\varepsilon''_{rel} = -\frac{\pi}{2}\frac{\partial \varepsilon'(f)}{\partial \ln f}$ (the definition is based on the Kramers-Kronig relationships). This procedure enhances the visibility of the peak.[21]

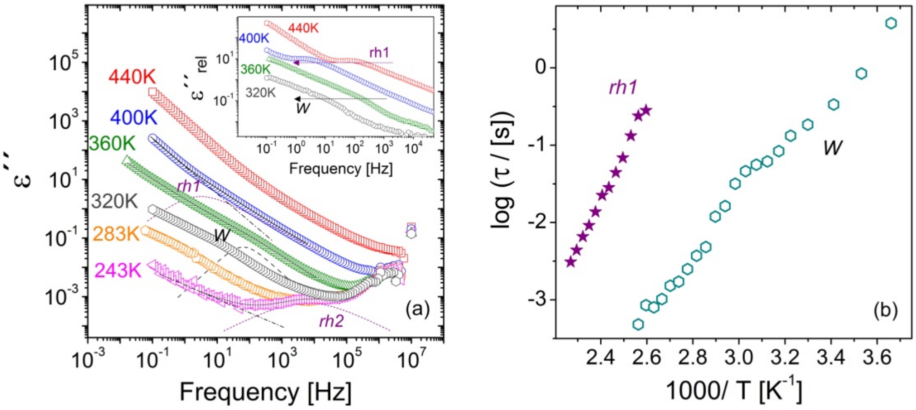

Figure 4.22 (a) Dielectric loss spectra of Rh6G at selected temperatures, upon cooling from 440 to 200 K. Solid lines through the data are fits. The two relaxation processes intrinsic to the anhydrous Rh6G sample (labeled as rh1 and rh2, dotted purple lines) are fitted with Havriliak-Negami functions and the intermediate one, labeled as W (dashed black line), is fitted with a Debye function. Inset: ε'_{rel} spectra at 440, 400, 360 and 320 K, where the visibility of the peaks is enhanced[21] (see text). (b) Arrhenius plot of the relaxation times of the rh1 (stars) and W (empty hexagons) features upon cooling from 440 to 200 K.

The loss at lower frequencies was fitted with a Havriliak-Negami function. Its position matches that of the rh1 relaxation measured upon heating the pellet (see section 4.6). Instead, the loss at higher frequencies displays, at least at high temperatures, a Debye profile.

The W feature cannot be correlated with the W0 loss upon heating due to the fact that the water molecules responsible for the W0 relaxation desorb at much lower temperatures, and indeed, the W0 feature is absent from the dielectric spectra of a pre-heated Rh6G sample. The Debye lineshape of the W relaxation implies that this relaxation could arise from a space-charge effect. This is surprising because the rh1 relaxation is itself a space-charge loss. Interestingly, the lineshape of the W loss changes from a Debye to a Cole-Cole one below 360 - 350 K. The fact that this relaxation process becomes more intense upon cooling and that it changes shape below the condensation point of water vapor (373 K) indicate that such possible space-charge relaxation can be affected by water molecules in way similar to the W1 relaxation discussed in the preceding section. In other words, the W process is interfacial in nature, as the rh1 and W1 relaxations. Since the measurements are done under nitrogen gas flow, the water moieties that condense on the sample must be still present in the pellet at 440 K, that is, they must remain trapped within the Rh6G matrix even above the desorption of hydration water likely as water vapor trapped inside pores. At the present time, the exact origins of the W relaxation upon cooling and of the W1 upon heating are not known. In what follows we display some of the features of the W relaxation and compare them with the parameters of W1 feature. Figure 4.23 (a) shows the comparison between the characteristic times of the W relaxation (upon cooling) and those of the W1 feature (upon heating).

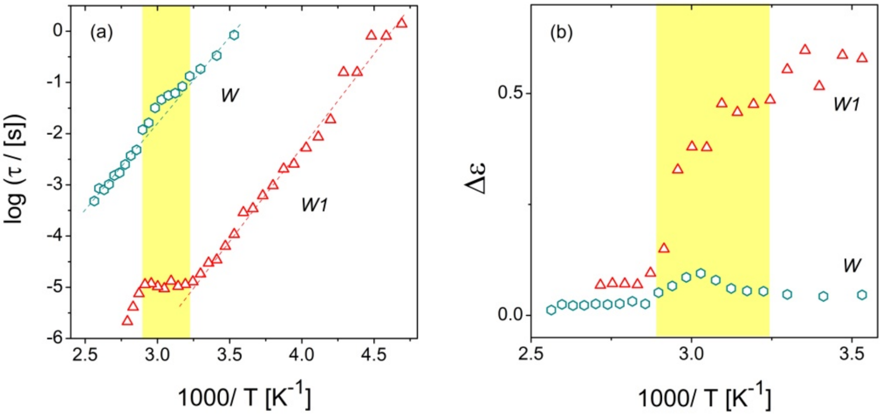

Figure 4.23 (a) Arrhenius plots of the relaxation times of the W (hexagons) and W1 (triangles). The W feature is measured upon cooling, while the W1 is detected upon heating. Discontinuous lines through the data are Arrhenius fits. (b) Temperature dependence of the dielectric strength (Δε) of the W (hexagons) and W1 (triangles) processes. The yellow bands indicate the temperature region where the main changes in the temperature-dependence of the parameters occur (350 K - 310 K).

It is seen that, although occurring at very distinct times and with distinct strengths, both processes have similar activation energy (E_α) values. The value of E_α of the W process is about 0.70 ± 0.12 eV, which is very close to the E_α of the W1 process (0.73 eV). This is in line with the idea that the water molecules responsible for W and W1 features are found in similar (interfacial) enviroments.[5]

Figure 4.23 (b) displays a comparison of the dielectric strength parameters of both W (upon cooling) and W1 (upon heating) features as function of reciprocal temperature. We observe that Δε of W appears constant upon cooling until it reaches ~360 K, when it starts to increase slightly. This change coincides with the abrupt decrease in Δε of W1 upon heating, which is attributed to the dehydration process. Hence, the change of $\Delta\varepsilon$ of W process at ~360 K may indeed be associated with the condensation of adjacent water molecules onto Rh6G grains upon cooling. The change of the dielectric strength of W feature at ~360 K accompanies a small anomaly of its characteristic time (Figure 4.23 (a)). At temperatures higher than this change, the water molecules trapped in the Rh6G pores would not affect the W relaxation (nor can their very fast dynamics be observed in our experimental range). Instead, below this temperature, the residual water starts condensing onto the inner surfaces of the pellet, thus contributing to the overall loss. Finally, a decrease of $\Delta\varepsilon$ occurs at ~330 K, possibly due to condensation of more water.

The very observation of the W relaxation at high temperature, and the initial Debye lineshape of this same relaxation imply that its origin is an electronic space-charge effect, just as for the rh1 relaxation. Since one can expect that binding of water vapour onto the Rh6G surface can affect the properties of the space-charge relaxation of electronic charge carrier, we argue that the W loss is the (electronic) space-charge relaxation at Rh6G pores containing trapped water molecules, while the rh1 relaxation is the (electronic) space-charge relaxation of water-free Rh6G. This assignment confirms that the W1 relaxation has a dipolar origin: the characteristic times of the rh1 and W processes are too long compared to the W1 process for the latter to share the same electronic space-charge origin.

To summarize, Figure 4.24 shows a schematic representation of a hydrated Rh6G grain, and the proposed reorientational and space-charge losses. The W2 and W1 relaxations processes are caused by the orientational motions of water moieties in different hydration levels (although W1 might also have a partial conductivity origin). The rh1 and rh2 features are intrinsic to pure Rh6G: the former is a space-charge relaxation of electronic charge carriers at grain boundaries, while the latter is a true reorientational relaxation of the Rh6G molecules. Finally, the W0 relaxation is the space-charge relaxation of protons at the boundaries of the hydration water layers.

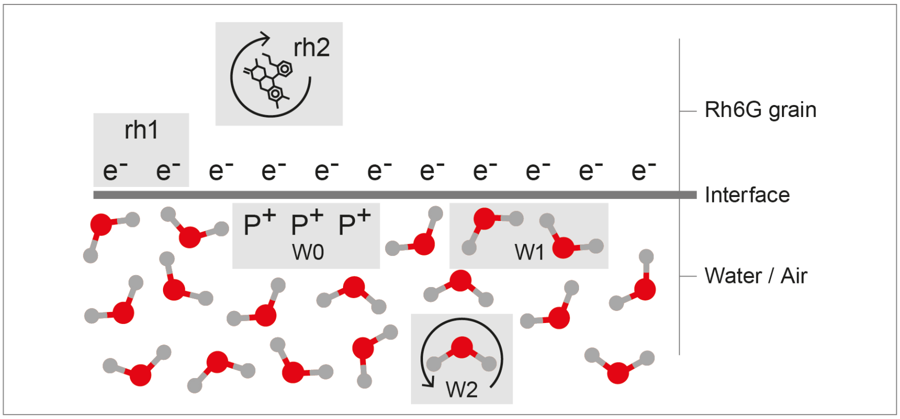

Figure 4.24 Microscopic representation of the different water types within the Rh6G matrix. The W2 relaxation is attributed to single-molecule dynamics of water molecules having only weak interaction with the Rh6G matrix. Conversely, W1 is associated with water molecules attached directly onto the surface of the grains, leading to a lower mobility at longer characteristic times. W0 relaxation is related to the protons at the boundaries of the hydration water layers. The rh1 and rh2 relaxations, intrinsic of Rh6G, are also shown.

4.8 Conclusions

We have investigated the intrinsic and water-related dynamics of the organic molecular solid Rh6G. The water molecules occupy different sites in between the material´s grains. Thermal analysis techniques have shown the dehydration and disintegration endothermic processes of the Rh6G compound. Both thermal and vibrational spectroscopy analysis of the hydrated samples have proven the hygroscopic nature of the molecular solid and have shown the existence of different water environments within Rh6G.

A total of five dielectric relaxation processes are detected. Of these, two relaxations (rh1, rh2) are intrinsic to the (water-free) Rh6G sample. Both match approximately the relaxation dynamics observed in Rh6G thin films. The faster one (rh2), which is significantly affected by the presence of water, is assigned to a local dipolar motion involving the charged nitrogen atom of the Rh6G cation and the chlorine counter-ion, while the slower (rh1) is related with a space-charge relaxation of electronic charge carriers (accumulation of electrons/holes at the grain boundaries of the pure material). Three relaxations (W0, W1 and W2) were ascribed to water inside Rh6G. Two of them (W1 and W2) stem from reorientational motions of water molecules within Rh6G matrix, while the other one (W0) is the space-charge relaxation associated with protonic species, which are responsible for a water-induced charge transport mechanisms occurring through the hydration layers (i.e., in between Rh6G grains or at their surfaces). The lowest temperature relaxation (W2) has the characteristic traits of the single-water-molecule (β) relaxation. The parameters of the W2 relaxation are in agreement with the β-water relaxation in various water-containing systems. While both the W1 and W2 relaxations have reproducible characteristic times in different samples, the W0 relaxation shows more variability. Upon heating to higher temperatures, few water molecules remain within Rh6G matrix, which give another relaxation (W) visible only upon cooling, whose origin is an electronic space-charge effect in the presence of surface water molecules.

Bibliography

[1] https://en.wikipedia.org/wiki/Fluorophore.

[2] M. Majoube, M. Henry. *Spectrochim. Acta A*, vol.47, p.1459, 1991.

[3] D. K. Das, T. Mondal, A. K. Mandal, K. Bhattacharyya, doi: 10.1002/asia.201100272.

[4] M. Zachariah, E. Mitsari, M. Romanini, P. Zygouri, D. Gournis, M. del Barrio, J.L.Tamarit, R. Macovez *J. Phys. Chem. C.*, vol. 119, p. 685, 2015.

[5] R. Macovez, E. Mitsari, M. Zachariah, M. Romanini, P. Zygouri, D. Gournis, J.L.Tamarit, *J. Phys. Chem. C.*, vol. 118, p. 4941, 2014.

[6] F. Gallego-Gómez, A. Blanco, D. Golmayo, C. Lopez *Langmuir*, vol. 27, p. 13992, 2011.

[7] G. D. Knowlton, T. R. White, H. L. Mckague, Clays and Clay Minerals vol. 29 p. 403, 1981.

[8] K. R. Heys, M. G. Friedrich, R. J. Truscott *Invest Ophthalmol Vis Sci.*, vol. 49, p. 1991, 2008.

[9] H. Weininger, J. Schmidt, A. Penzkofer *Chem. Phys.* vol. 130, p. 379, 1989.

[10] S. Le Caer, S. Pin, S. Esnouf, Q. Raffy, J. Ph. Renault, J.-B Brubach, G Creff, P.Roy *Phys. Chem. Chem. Phys.*, vol. 13, p.17658, 2011.

[11] E. Pretsch, P. Bühlmann, C. Affolter, A. Herrera, R. Martínez *Structural determination of organic compounds.* Barcelona: Masson, 2002.

[12] B. Brubach, A. Mermet, A. Filabozzi, A. Gerschel, P. Roy *J. Chem. Phys.*, vol. 122, p. 184509, 2005.

[13] S. Cerveny, F. Barroso-Bujans, Á. Alegría, J. Colmenero *J. Phys. Chem. C.*, vol 114, p. 2604, 2010.

[14] L. P. Singh, S. Cerveny, A. Alegria, J. Colmenero *Chem. Phys. Chem.*, vol. 12, p. 3624, 2011.

[15] Y. E. Ryabov, A. Gutina, V. Arkhipov Y. Feldman *Phys. Chem. B,* vol. 105, p. 1845, 2001.

[16] S. Le Caër, M. Lima, D. Gosset, D. Simeone, F. Bergaya, S. Pommer-et,J-Ph. Renault, R. Righini *J. Phys. Chem. C*, vol. 116, p. 12916, 2012.

[17] J. Einfeldt, A. Kwasniewski *Cellulose,* vol. 9 p. 225, 2002.

[18] K. L. Ngai, S. Capaccioli, S. Ancherbak, N. Shinyashiki *Philos. Mag.*, vol. 91, p. 1809, 2011.

[19] J. Sjöström, J. Swenson, R. Bergman, S. Kittaka *J. Chem Phys.*, vol. 128, p. 154503, 2008.

[20] H. Haspel, V. Bugris, A. Kukocecz *J. Phys. Chem. C*, vol. 117, p. 16686, 2013.

[21] M. Wübbenhorst, J. van Turnhout *J. Non-Crist. Solids.*, vol. 305, p. 40, 2002.

[22] P. Tripathi, J. G. Ruiz, E. Mitsari, M. Zachariah, M. Romanini, Josep Ll. Tamarit, F. X. Munoz, Roberto Macovez *J. Phys. Chem. Lett.* vol. 5, p. 2796, 2014.

[23] R. Macovez, M. Zachariah, M. Romanini, P. Zygouri, D. Gournis, J.L.Tamarit *J. Phys. Chem. C.,* vol. 118, p. 12170, 2014.

[24] H. Han, C. Davis, III, J. C. Nino *J. Phys. Chem.,* vol. 118, p. 9137, 2014.

[25] W. Brutting, Ch. Adachi *In Physics of organic Semiconductors, 2nd ed*. Chichester: Wiley, 2012.

[26] Sh. A. Mansour, I. S. Yahia, F. Yakuphanoglou *Dyes and Pigments* vol. 87, p. 144, 2010.

[27] D. L. Sidebottom *Phys. Rev. Lett.,* vol. 82, p. 3653, 1999.

[28] F. Kremer, A. Schönhals *Broadband Dielectric Spectroscopy.* Berlin: Springer, 2002.

[29] K. Grzybowska, A. Grzybowski, S. Pawlus, S. Hensel-Bielowka, M. Paluch *J. Chem. Phys.* vol. 123, p. 204506, 2005.

[30] L. Frunza, H. Kosslick, S. Frunza, A. Schonhals, *J. Phys. Chem B*, vol. 106, p. 9191, 2002.

[31] S. Sudo, N. Shinyashiki, S. Yagihara, *J. Mol. Liq.*, vol. 90, p. 113, 2001.

[32] S. Capaccioli, K. L. Ngai, N. Shinyashiki *J. Phys. Chem B*, vol. 111, p. 8197, 2007.

[33] S. Cerveny, G. Schwartz, R. Bergman, J. Swenson, *Phys. Rev. Lett.*, vol. 93, p. 245702, 2004.

[34] R. K. Chan, D. W. Davidson, E. J. Whalley *J. Chem. Phys*., vol. 43, p. 2376, 1965.

[35] I. Popov, A. Puzenko, A. Khamzin, Y. Feldman *Phys. Chem. Chem. Phys.,* vol. 17, p. 1489, 2015.

[36] G. P. Johari, E. Whalley, *J. Chem. Phys.*, vol. 75, p. 1333, 1981.

[37] N. Shinyashiki, W. Yamamoto, A. Yokoyama, T. Yoshinary, S. Yagihara, R. Kita, K. L. Ngai, S. Capaccioli *J. Phys. Chem. B* vol. 113, p. 14448, 2009.

[38] J. Hedstrom, J. Swenson, R. Bergman, H. Jansson, S. Kittaka *Eur. Phys. J-Spec. Top.*, vol. 141, p. 53, 2007.

[39] L. Frunza, H. Kosslick, I. Pitsch, S. Frunza, A. Schonhals *J. Phys. Chem. B*, vol. 109, p.9154, 2005.

[40] P. Pissis, J. Laudat, A. Kyritsis *J. Non-Cryst. Solids*, vol. 171, p. 201, 1994.

[41] A. A. Milischu, B. M. Ladanyi *J. Chem. Phys.*, vol. 135, p. 174709, 2011.

[42] Jonscher, *Dielectric Relaxation in Solids*. London: Chelsea Dielectric Press 1983.

[43] A. Puzenko, P. B. Ishai, Y. Feldman *Phys. Rev. Lett.*, vol. 105, p. 037601, 2010.

[44] Y. E. Ryabov, Y. Feldman, N. Shinyashiki, S. Yagihara *J. Chem. Phys.* vol.116, p. 8610, 2002.

[45] Y. E. Ryabov, A. Puzenko, Y. Feldman *Phys. Rev. B*, vol. 69, p. 014204, 2004.

[46] H. Anderson, G. A. Parks *J. Phys. Chem*., vol. 72, p. 3662, 1968.

[47] C. Knight, G. A Voth, *Acc. Chem. Res.*, vol. 45, p. 101, 2012.

Chapter 5

DYNAMICS OF H_2O IN SOLID FULLERENOL.

5.1 Introduction

Fullerenes, which represent the fourth known allotrope of carbon after diamond, graphite and amorphous carbon, were considered for some time promising materials for a wide range of applications. However, the utilization of these remarkable all-carbon molecules for applications in biochemistry and medicine or low-cost device fabrication is hindered by their insolubility in a large number of solvents[1] (besides organic ones including especially water, where clustering of the molecules is reported.[2] Enhanced water solubility can be achieved through synthetic methods by addition of hydrophilic side-groups (hydroxyl, amine, etc.) to the carbon cage. Large number of water-soluble fullerene derivatives has been synthesized when these side-groups are covalently attached on carbon atoms of the fullerene cage.[3] Polyhydroxylated fullerene (also known as fullerenol or fullerol, of chemical formula $C_{60}(OH)_n$ with n between 6 and 44) is one of the most studied fullerene derivatives. It shows increasing solubility with increasing number of side adducts. Generally, fullerenols with a higher number of hydroxyl groups (e.g. 16, 20-24, 36 or 44) exhibit higher solubility in water, between tens and hundreds of grams per liter.[4,5] In some cases functionalization leads, besides to hydrophilicity, also to hygroscopic behavior. This is the case of polyhydroxylated fullerene $C_{60}(OH)_{24}$, which is studied in this chapter (Figure 5.1).

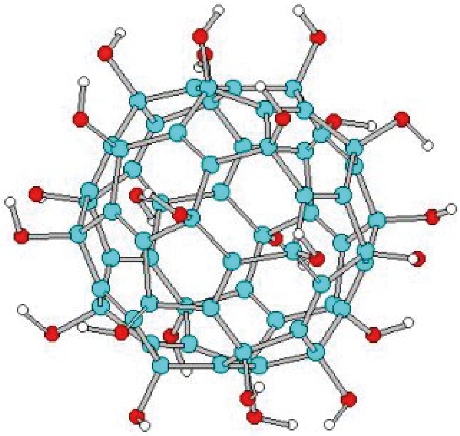

Figure 5.1 Molecular structure of the fullerenol molecule.

As most organic molecular materials, fullerenes and their derivatives are semiconducting or insulating in the solid state. C_{60} is an electron accepting molecule,[6,7] and this property is retained by most of its derivatives.[8] Charge transport in fullerene solids may be due either to electrons/holes introduced by thermal excitation and by the presence of defects or impurities, as in other organic semiconductors, or else to small ionic species (usually cations) diffusing through the organic matrix. Besides supporting electronic conduction, fullerenols can also support proton conductivity when hydrated, that is, when water is the source of the protonic charge carriers, as found also for other fullerene derivatives.[9]

Fullerenol is the first fullerene-based material studied in this thesis (two more chapters are devoted to systems involving fullerene). The symmetric distribution of the covalently bonded hydroxyl groups onto the fullerene cages leads to zero dipole moment of the fullerenol molecule, thus no dipolar relaxation is expected to be observed with dielectric spectroscopy. The lack of a dipole moment, as well as its highly hydrophilic and hygroscopic nature, makes fullerenol a suitable material in order to study the dynamics of water-guest molecules and water-induced conduction effects within carbon structures.

5.2 Experimental Methods

Polyhydroxylated fullerenes or fullerenols (chemical formula $C_{60}(OH)_{24}$) were synthesized from polybrominated fullerenes following the procedure described in reference 10. In a typical synthesis, 300 mg of fullerene (Aldrich, 99.8 %) were dissolved in 2 ml of elementary bromine, in the presence of the catalytic quantities of $FeBr_3$. The mixture was stirred for 40 minutes at room temperature and when reaction was completed, the excess of unreacted bromine was evaporated and the catalyst was separated by dissolving in a mixture of $EtOH/H_2O$ (v/v 1:2). The product was an orange-brown powder that showed no solubility in organic solvents. The fullerenol derivative $C_{60}(OH)_{24}$ was obtained upon reaction of $C_{60}Br_{24}$ with 5 ml of NaOH 2M (pH =13) for 2 hours at room temperature. After the completion of the reaction, the solvent was evaporated at 40 ^{o}C and the mixture was filtered and washed 5 times with 10 ml of ethanol (70 %). The product after the filtration was a dark brown powder, soluble in polar solvents like water.

The powder of fullerenol, stored in air, was characterized by thermogravimetric analysis (TGA) and differential scanning calorimetry (DSC) as thermal probes. Fourier-transform infrared spectroscopy (FT-IR) and X-ray powder diffraction (XRPD) were also used as complementary characterization techniques. Finally, broadband dielectric spectroscopy (BDS) was utilized for studying the dynamic behavior of water-related relaxation features in the fullerenol powder.

TGA scans were acquired while heating the sample under N_2 atmosphere between room temperature (303 K) and 623 K at a rate of 2 K per minute. DSC experiments involved heating and cooling cycles in the temperature interval between 290 and 600 K, at a same rate as used for TGA scans. Also, another DSC heating-cooling cycle was carried at lower temperatures (between 295 and 200 K) at a rate 2 K/min. The samples were weighed before and after the measurements. FT-IR measurements were acquired on samples~~,~~ which were prepared in pellet form with the addition of potassium bromide (KBr). Due to the hygroscopic nature of KBr, we were keeping the powder to the furnace (373 - 383 K) for 20 hours prior to the measurement. The pellets have a diameter of ~13 mm. The characterization was performed at room temperature in the mid-infrared wavelength range (4000 cm^{-1} - 400 cm^{-1}). We have conducted measurements on an as-stored sample and on an annealed sample at 420 K. FT-IR characterization was carried out at the centre for research in nanoengineering of the UPC (CRnE). High-resolution XRPD patterns were acquired at room temperature on an as-stored sample and in a sample preheated to 413 K. The acquisition time was almost 4 hours for each measurement.

BDS measurements were carried out using a parallel-plate capacitor configuration made by a pellet sandwiched between two metal disks (see section 3.4) The pellet form of the samples was achieved using a hydraulic press (20 kN), with pellet thickness between 0.25 and 0.35 mm. Dielectric spectra were acquired in the temperature range between 193 and 413 K, every 5 K upon heating and every 10 K upon cooling (with a temperature stability of ± 0.5 K).

5.3 Thermal study of a hydrated fullerenol

The covalent functionalization of fullerenes with oxygen-containing groups leads in some cases to hydrophilic and hygroscopic behavior. The C_{60} derivatives studied in this thesis are of this type. In some cases, the interaction with retained water moieties can be particularly strong, which implies the need of higher thermal energy in order to desorb the water species. This may be gathered from Figures 5.2 and 5.3, where we show the TGA and DSC curves, respectively, measured on an as-stored fullerenol powder.

The first mass loss (up to approximately 420 K) is due to water desorption. The dehydration process results in a 20% loss of the initial mass of the as-stored fullerenol sample (Figure 5.2), which is quite large in comparison with hydrated Rh6G (see preceding chapter). The asymmetric shape of the dehydration peak is similar to the one of Rh6G. The multi-component curve is reminiscent of those of other C_{60}-derived systems[11] and results from the different processes accompanying the water loss and, at higher temperature, from decomposition of the material. In the case of fullerenol, the first mass loss between room temperature and 350 K corresponds to the loss of water physisorbed onto the outer surface of the fullerenol grains. This water, commonly termed "secondary water", is present in all the samples due to their continuous contact with (normal or relatively humid) atmospheric conditions.[12] The main mass loss occurs at temperatures close to or higher than the boiling point of pure water at standard pressure (373 K), and display in fact a maximum at 393 K. Such mass loss is possibly associated with bulk-like water inside the fullerenol matrix and to water with direct hydrogen bonds to the hydroxyl groups of the fullerenol molecules. Both would rationalize the higher desorption temperatures. This main mass loss extends up to 420 K, and it is possible that the mass loss visible above 400 K also involves the partial loss of some hydroxyl groups covalently attached onto the fullerene cages.

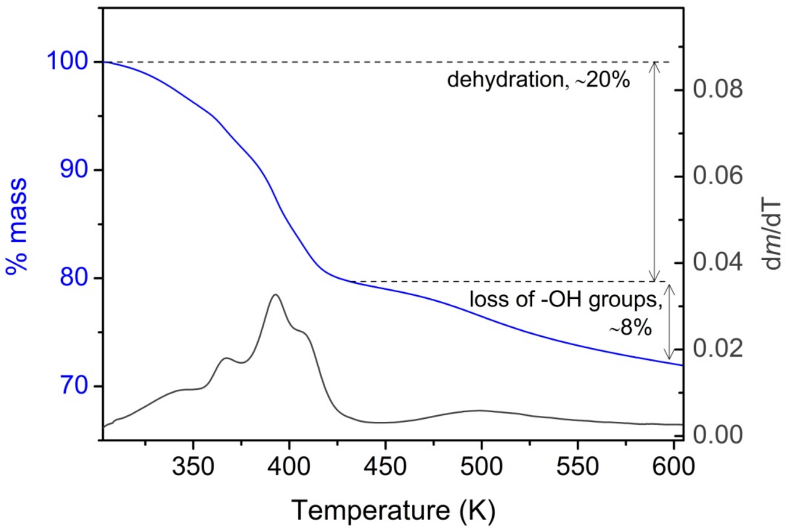

Figure 5.2 TGA thermograph of the hydrated fullerenol (blue line) and its first derivative (grey curve) in the temperature range 303 K - 605 K. For each step, the corresponding lost moieties and the related percentage are indicated. The heating rate is 2 K/min.

Fullerenol shows a further mass loss above approximately 425 K, peaked in fact around 500 K. This high-temperature loss is associated with the loss of the covalently bonded hydroxyl groups, and marks the onset of the decomposition of the material. Fullerenol decomposes totally at higher temperatures (T > 623 K), i.e., decomposition of fullerenol does not lead to the formation of pristine fullerite . In general, the different mass loss steps are not clearly separated in temperature, so that the onset temperature of each process is not well defined and their corresponding percentage of mass loss is only approximate. However, assuming that all water has left the sample at 420 K, we have estimated the number of water molecules per fullerenol moiety, which turned out to be of approximately 16 H_2O molecules per fullerenol, distributed in distinct environments.

The dehydration and dehydroxylation processes are also observed in the scanning calorimetry data acquired on a fullerenol sample upon heating from 290 to 600 K. Figure 5.3 displays the DSC curve of the dehydration process between 290 and 440 K. The curve exhibits a multi-component dehydration peak, which lies in the same temperature interval as in TGA measurements (320 K - 420 K). Each component of the DSC peak has approximately the same peak maximum temperature as the corresponding TGA derivative peaks.

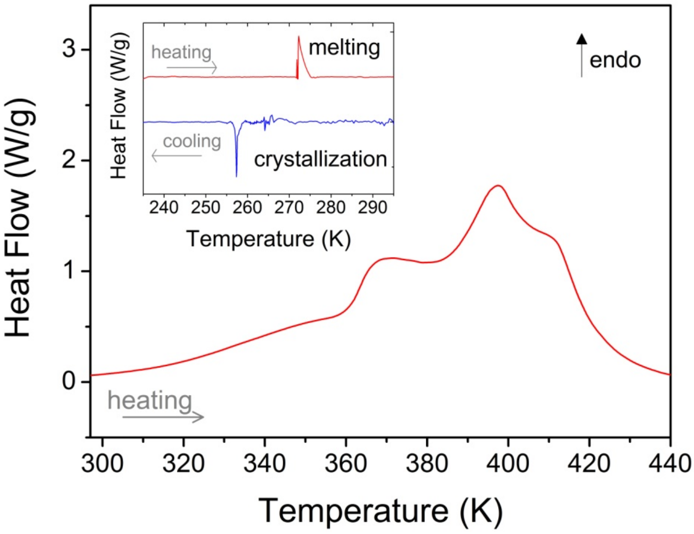

Figure 5.3 DSC thermograph of hydrated fullerenol (20% water) upon heating between 297 and 440 K. The heating rate is 2 K/min. Inset: DSC thermograph of another hydrated fullerenol sample upon cooling and heating between 295 and 235 K with the same heating rate. Heating and cooling processes are depicted by red and blue curves, respectively.

After heating to the highest temperature and then cooling down till ambient temperature, we did not observe any peak, implying that the transitions observed in DSC are irreversible (as are, of course, the corresponding mass losses). Furthermore, we conducted a DSC measurement on a different hydrated sample in a cooling - heating cycle at a temperature interval between 295 and 200 K, in order to detect any calorimetric response of water at low temperatures (crystallization/melting peak). The result can be seen in the inset of Figure 5.3. As expected from the high water content of the sample, an exothermic peak at ~256 K was observed upon cooling, indicating the formation of ice. The corresponding melting peak is observed at ~271 K upon heating. The observed DSC signals indicate the presence of bulk-like water in the sample. The high water content revealed by thermal analysis gives rise to a complex dielectric signal in hydrated fullerenol (see section 5.5), in an analogous way as found in Rh6G.

5.4 Spectroscopic and Structural Characterization (FT-IR, XRD)

To further investigate its water content, we have studied fullerenol by means of FT-IR spectroscopy. We have acquired the infrared spectra of two fullerenol samples at room temperature on an as-stored sample (Figure 5.4), and on a sample after annealed at 420 K (Figure 5.5 (b)), in order to identify the contribution of water. The molecule´s bond vibrations have wavenumbers in the mid-infrared range (4000 ÷ 400 cm^{-1}). As one may expect, an unambiguous identification of the characteristic peaks of water vibrations is a difficult task due to the presence of the hydroxyl groups attached covalently onto the C_{60} cages.

Both hydroxyl groups intrinsic to fullerenol and those due to water molecules exhibit intra-molecular bond vibrations at similar wavenumbers, in the range between 3600 cm^{-1} and 3100 cm^{-1}. However, various absorption peaks are visible also at lower frequencies, due to vibrations of both fullerenol molecules and to water contributions.

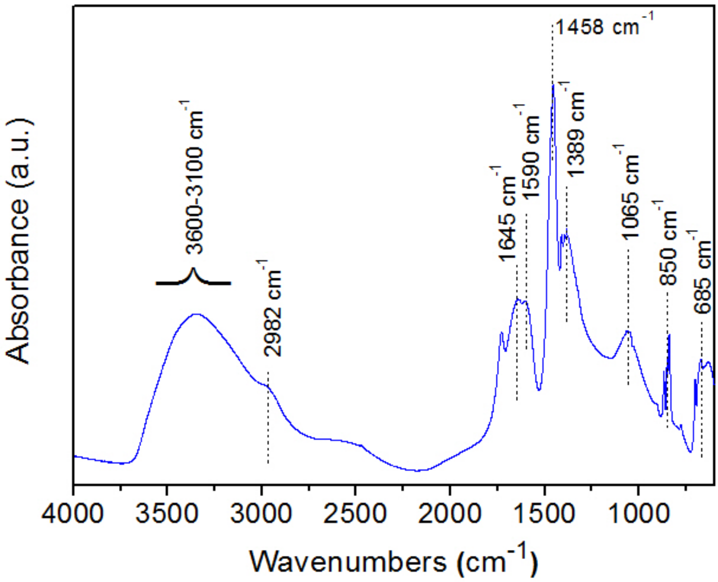

Figure 5.4 FT-IR spectrum of fullerenol at room temperature. The spectral positions of the absorption bands that could be assigned to fullerenol or water vibrations are marked by vertical dotted lines.

Characteristic IR bands due to the hydroxyl groups of the fullerenol molecules are observed at 685 and 850 cm^{-1} (O-H wagging) and as well at 1065 cm^{-1} (C-O stretching mode)[13], 1389 and 1458 cm^{-1} (C-OH bending modes).[10,14,15].The band at 1645 cm^{-1} is instead indicative of the presence of water molecules.[16,17] We also observed two absorption peaks at 1590 and 2982 cm^{-1}, which correspond to carbon-carbon double bonds and C-H stretching modes of fullerenol, respectively.[18]

In Figure 5.4, the broad spectral feature from 3600 to 3100 cm^{-1} is indicative of the O-H stretching vibrations. Due to the simultaneous presence of O-H moieties of fullerenol and water molecules, a more detailed analysis is carried out on this feature. As in the case of the FT-IR analysis of Rh6G (see section 4.4), we have fitted the high frequency spectral range with separate Gaussian components (Figure 5.5 (a)). Additionally, we have acquired a room temperature spectrum of an annealed sample to 420 K, in order to identify the water contributions, given that, according to our TGA characterization, most water desorbs from the sample below this temperature (section 5.3). Three components can be identified by means of the Gaussian fit of FTIR spectra. The presence of three bands is also directly visible in the spectrum acquired on the preheated sample (Figure 5.5 (b)). Comparing the spectra before and after heating to 420 K, it would appear that the contribution of water vibration is significant in terms of overall intensity and that it is quite broad in terms of spectral profile, as it may be expected due to the different environments of water molecules in the sample. Also, we point out that, contrary to the Rh6G case, we cannot heat to temperatures higher than 420 K to eliminate completely the contribution of water, due to the decomposition of the fullerenol powder above 430 K. In fact, we have seen in the previous section that de-hydroxylation starts before the end of the dehydration process. This implies that some water is still present in the preheated sample.

A tentative assignment of the three IR features may be attempted based on comparison with similar studies. The first component lies at 3550 cm^{-1} (1) and corresponds to the O-H stretching vibrations of water molecules that have a low number of hydrogen bonds (*i.e.*, to secondary surface water or small water aggregates such as dimers).[16] The second one is centered at ~3400 cm^{-1} (2) and is indicative of the O-H stretching vibrations intrinsic to fullerenol molecules.[10,13] This peak could be partially associated with water molecules interacting with the material´s surfaces or confined at interstitial voids.[16] The fact, however, that this absorption peak remains the most intense, in the spectrum of the annealed sample, (Figure 5.5 (b)) suggests that this band stems predominantly from the OH vibrations of the fullerenol molecule. The last Gaussian component is centered at 3170 cm^{-1} (3) and is probably associated with the bulk-like water present in the powder, which crystallizes at lower temperature and melts at 273 K (see Figure 5.3).[16,17] As it can be observed in Figure 5.5 (b), the latter component undergoes a major reduction after heating to 420 K, due to water desorption. The difference in wavenumber between the two water components is due to the fact that bulk-like water molecules have four hydrogen bonds per molecule, while water in few-molecule aggregates or at the outer surface of a hydration layer has on average only one or two hydrogen bonds per molecule (thus leading to faster vibration).

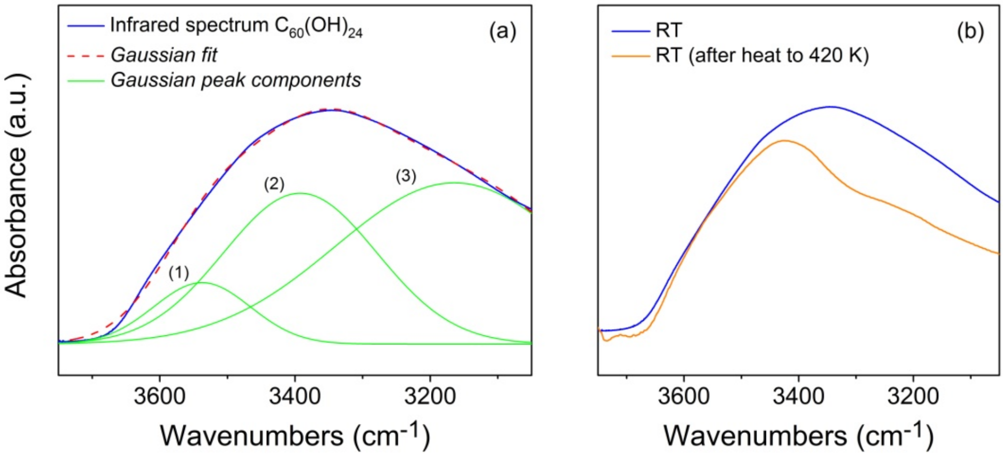

Figure 5.5 (a) FT-IR spectra of fullerenol, at room-temperature, in the 3750 - 3050 cm^{-1} spectral range, characteristic of O-H stretching vibrations. The experimental data (blue curve) between the frequencies 3750 - 3050 cm^{-1} were fitted (red dashed curve) as the sum of three Gaussian components (green curves), centered respectively at 3550 (1), 3400 (2) and 3170 (3) cm^{-1}. (b) Comparison between the room-temperature FT-IR spectra of the as-stored powder (blue curve) and after heating it to 420 K (orange curve). The latter was normalized to the intensity of the component at the highest wavenumber in the spectrum of the as-stored powder. The spectral range is the same as in panel (a).

Figure 5.6 shows the XRPD patterns of hydrated and quasi-anhydrous samples of fullerenol. The hydrated fullerenol powder exhibits only weak, broad diffraction features. This indicates that hydrated fullerol has a high degree of disorder or very low crystallinity. Upon heating, the material exhibits more crystalline character. This is confirmed by the appearance of clear, narrower diffraction peaks after heating at 413 K, where most of the water has left from the fullerenol sample. Even so, the diffraction pattern of the quasi-anhydrous material shows a high scattering background and significantly broad peaks, suggesting only partial order.

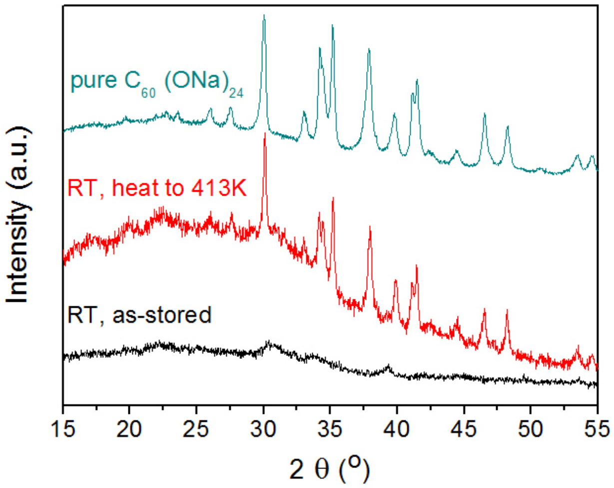

Figure 5.6 XRPD patterns at room-temperature of the as-stored fullerenol (black line) and of a fullerenol sample after heating at 413 K (red line), after de-hydration process. The 2θ range is between 15° and 55°. For comparison, we have added the room-temperature XRPD pattern of an ionic salt of C_{60}, namely $C_{60}(ONa)_{24}$ (blue line), in its pure phase.[19]

An intriguing fact is the similarity between fullerenol and the related $C_{60}(ONa)_{24}$ compound, where the covalently bonded OH groups are substituted by (more ionic) O-Na groups.[19] Both molecules show similar diffraction patterns in their pure phase (after water loss). This originates from the fact that fullerenol is used as the initial material for the synthetic route of the C_{60} sodium salt.

The high water content within a non-polar molecule such as fullerenol leads, as we show in the next section, to an interesting and diverse dynamics of the water guest-molecules.

5.5 Dielectric Spectroscopy Study

In the previous chapter the dynamics of water inside a chlorine salt (Rh6G) was measured. That material exhibited intrinsic relaxation processes, thus making the identification of the dynamical behavior of water guest-molecules a complicated task. Fullerenol has zero dipole moment [20] by symmetry, implying that the pure material should not exhibit any relaxation in BDS, which can only detect changes in the orientation and the magnitude of electric dipoles in the sample.[21] Hence all relaxation peaks observed in fullerenol must arise either from polar "impurities" such as water molecules or else have a conductivity origin. The fullerenol system under scrutiny is a (hydrated) powder of carbon cages covered by hydroxyl groups in a symmetrical way. Here, we study the dynamical behavior of water molecules in fullerenol, which exhibits common traits with other hydrated systems,[20,22,23] including the existence of different relaxation features characteristic of water in distinct molecular environments.

The following figures show the dielectric loss spectra of hydrated fullerenol upon heating from low temperatures. The fullerenol sample (without any previous thermal treatment) was cooled down to 193 K and loss spectra were then acquired upon heating to 413 K, every 5 K. Figure 5.7 shows the dielectric spectra in the temperature interval between 193 and 303 K. As it can be seen, three relaxation processes are observed. We labeled the processes as I, II and III from the fastest (higher frequency) to the slowest (lower frequency) relaxation. The loss features of processes I and II appear broad and symmetric. Both were fitted with Cole-Cole functions with shape parameters $0.18 < \alpha_{CC} < 0.22$ for the process I and $0.66 < \alpha_{CC} < 0.45$ for process II. Feature II is slower by a factor of more than two orders of magnitude than feature I, and much more intense. The dielectric strength of process I depends only weakly on temperature, while the loss feature II exhibits increasing intensity upon heating to 303 K.

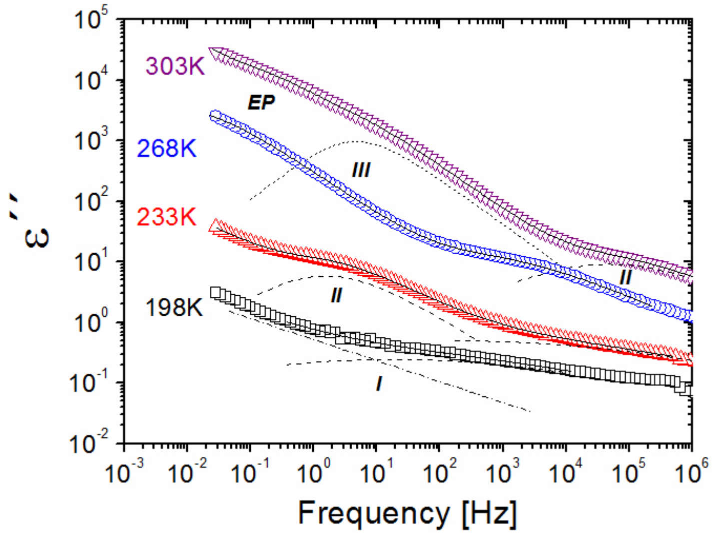

Figure 5.7 Relaxation dielectric loss curves for a fullerenol sample at various temperatures between 198 and 303 K. Three relaxation features are observed. The solid lines though the data are fits of loss peaks lying on a conductivity-like background. The loss peaks are fitted with Cole-Cole (dashed lines) and Havriliak-Negami (dotted line) functions. A fit of the conductivity-like background is shown only at the spectrum of 198 K (dashed-dotted line). At high temperatures and low-frequencies the electrode polarization effect is shown.

Another feature (process III) enters the experimental window from the low frequency side at approximately 278 K. Process III appears as a broad and asymmetric loss peak, and could be fitted with a Havriliak-Negami function with shape parameters $0.83 < \alpha_{HN} < 1$ and $0.92 < \beta_{HN} < 0.98$. All three processes shift to higher frequencies upon heating in this temperature interval (Figure 5.7), as it is expected for normal dielectric relaxation processes.

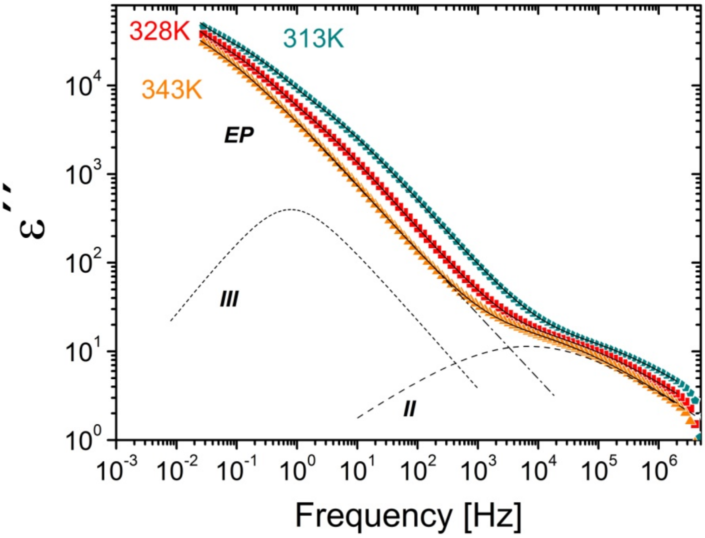

Figure 5.8 Dielectric loss spectra of a fullerenol sample upon heating from 313 K to 343 K. The solid lines though the data are fits of the loss peaks including a conductivity background (dashed-dotted line). The two loss peaks are fitted with Cole-Cole (dashed lines, process II) and Havriliak-Negami (dotted line, process III) functions, respectively. At low-frequencies the electrode polarization effect is shown.

At temperatures higher than 313 K, features II and III exhibit distinct atypical behavior. Between 313 and 343 K, both peaks shift to lower frequency upon heating, as it can be observed in Figure 5.8. A prominent electrode polarization effect is visible at low frequencies, which complicates the fitting of the slowest process III. A reduction of the conductivity background accompanies the anomalous shift of the loss peaks.

Above 343 K, the loss feature of process III is not visible, while the remaining feature (process II) keeps on displaying atypical behavior. At first, the peak remains at the same frequency position for few temperatures between 348 and 368 K (Figure 5.9 (a1)). The standstill of process II can be better visualized from the plots of the derivative of the real permittivity (panel a2). The low frequency part of the spectra (conductivity background and electrode polarization) starts rising once again at the same temperature range. At temperatures higher than 370 K, the lineshape of process II starts becoming broader and more asymmetric (Figure 5.9 (b)). Conductivity does not seem to vary with temperature in this range. The anomalous peak behavior in this temperature range (348 - 393 K) is more apparent in the right panels of Figure 5.9.

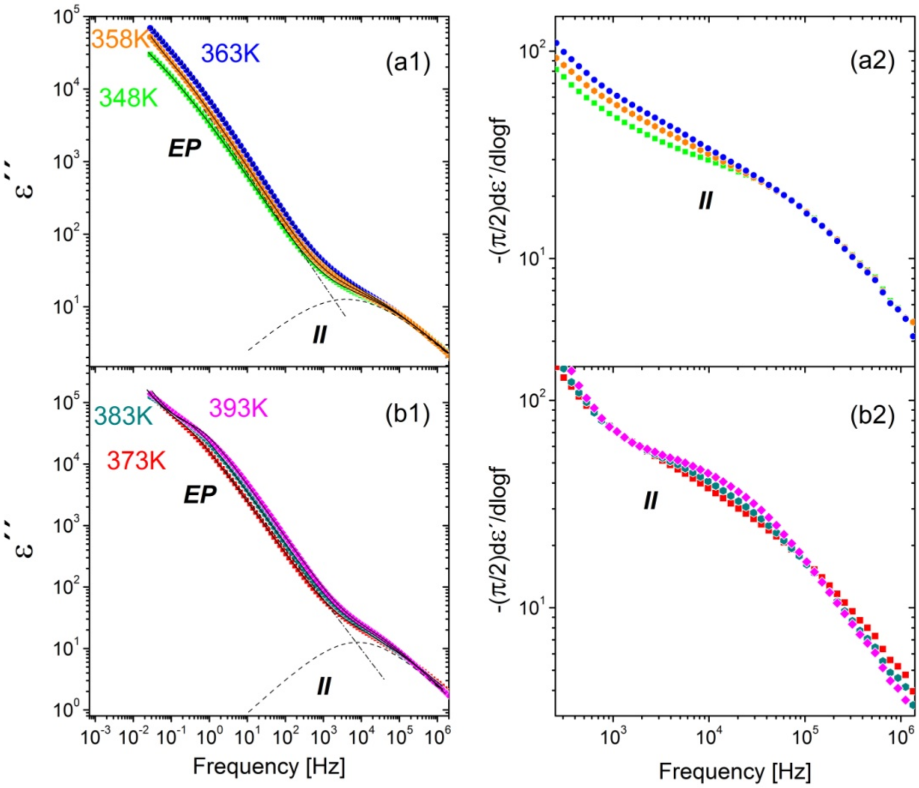

Figure 5.9 Dielectric loss spectra (left panels, 1) and corresponding plots of the derivatives of the real permittivity[24] (right panels, 2) for the fullerenol sample upon heating from 348 to 393 K. Panel (a) corresponds to the temperature range 348 - 363 K and panel (b) to 373 - 393 K. The solid lines through the data are fits with a Cole-Cole (dashed lines) function plus a conductivity background inversely proportional to the frequency (dashed-dotted line). At low frequencies an electrode polarization effect is visible.

The new lineshape of feature II can be fitted with a Havriliak-Negami function up to the highest measured temperature (413 K). It should be noted that, after behaving anomalously in the temperature region between 311 and 390 K, process II shifts properly as a normal dielectric peak upon heating from 393 to 413 K (Figure 5.10), interval in which also the conductivity shows a normal behavior for disordered systems, *i.e.*, it increases with increasing temperature.

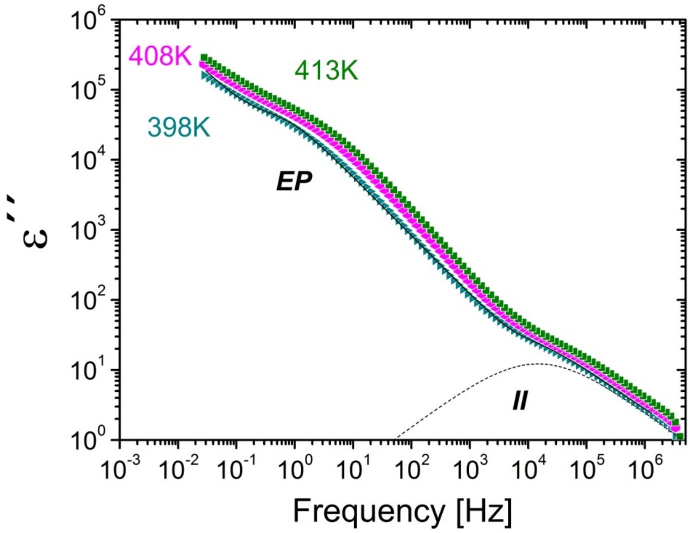

Figure 5.10 Dielectric loss curves of a fullerenol sample at three temperatures close to the end of the dehydration (398 - 413 K). A relaxation feature (process II) is observed at high frequencies. The solid line though the experimental spectrum at 398 K are fits with a Havriliak-Negami peak (dotted line) on top of a conductivity background. A prominent electrode polarization effect is visible at low frequencies.

To better visualize the temperature evolution of the relaxation processes of the hydrated fullerenol sample, we have plotted the relaxation times against inverse temperature (Arrhenius plot) in Figure 5.11. As it can be observed, the onset of the atypical behavior of both processes II and III is the same (~311 K), though this behavior extents to higher temperatures for process II (~368 K), as already discussed above. In the next section we will deepen our analysis of all three water-related dynamic processes in fullerenol.

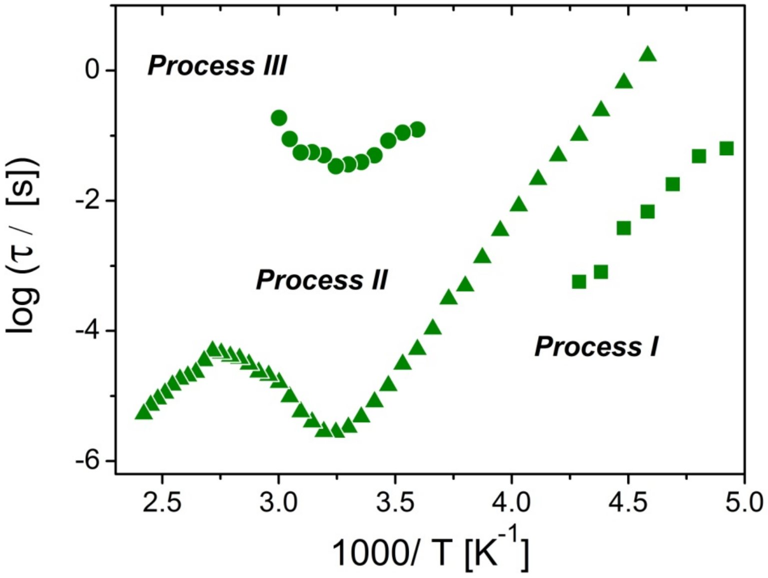

Figure 5.11 Relaxation times of the water-related processes (I, II, III) in hydrated fullerenol, as a function of reciprocal temperature. The temperature interval is between 193 and 413K.

5.6 Analysis of the water relaxation dynamics

Given that the observed relaxation processes cannot be intrinsic to fullerenol molecules due to its zero dipole moment, their origin is related with the (relatively high) water content of fullerenol and/or with space-charge effects. Based on our thermal analysis (section 5.3), we expect that after heating the samples at 410-420 K the water signature will no longer be present in the dynamical response of the fullerenol sample. To test this and identify the water-related contributions, we have acquired dielectric spectra on the same pellet described in section 5.5 upon cooling down from 413 to 200 K. In Figure 5.12 (a) we present the dielectric spectra of the resulting quasi-anhydrous fullerenol sample. As it can be observed, besides the electrode polarization effect only one relaxation feature is present in the spectra. The electrode polarization effect is visible only at high temperatures (above ~370 K). The loss feature, whose intensity varies only slightly with temperature, was fitted with a Havriliak-Negami function with exponents $0.63 < \alpha_{HN} < 0.86$ and $0.58 < \beta_{HN} < 1.00$. As it can be seen in Figure 5.12 (b), above 370 K this relaxation loss overlaps with process II measured upon heating the hydrated sample.

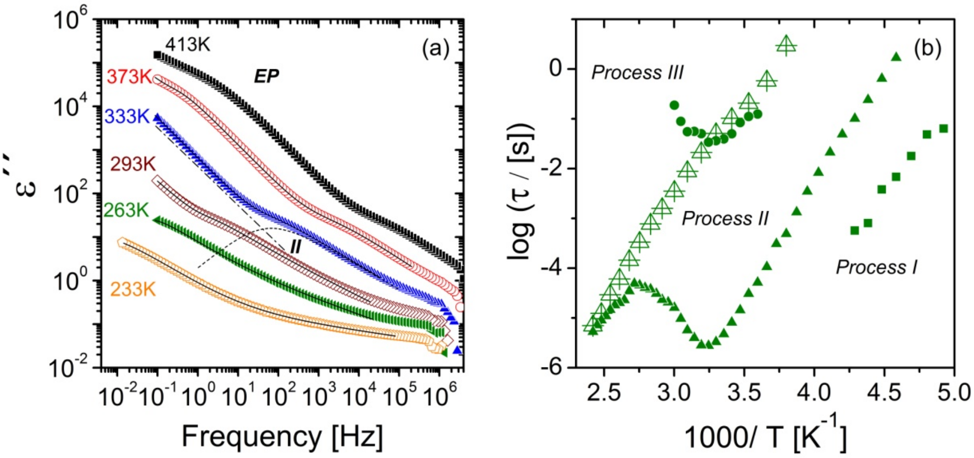

Figure 5.12 (a) Dielectric loss spectra of a quasi-anhydrous fullerenol sample, measured upon cooling down in the temperature interval 413 - 233 K. The solid lines through the data points represent the fits to experimental data. In the spectrum at 333 K the dotted line is the Havriliak-Negami function used to fit the loss peak, and the dash-dotted line corresponds to the conductivity background. The loss peak is labeled as process II given its similarity with such process. Only at the highest temperatures, a characteristic bending due to the electrode polarization is visible in the low-frequency part of the spectra. (b) Arrhenius plot of the relaxation times of the loss feature of panel (a) (measured upon cooling, empty triangles) together with the relaxation times of the three processes observed upon heating (filled triangles).

Since only the high-temperature process II is present in the quasi-anhydrous sample, all other relaxation processes that appear upon heating must be somehow related with the water content inside fullerenol. Some of them can be dipolar relaxations associated with actual motions of the water molecules, while other can result from other processes that occur inside the material and involve the presence of water (water-related charge transport mechanisms, non-homogeneity of the sample, etc.). In order to identify the exact origin of each relaxation, we analyze each feature separately. Firstly, we deal with the two relaxation processes (I and III) which occur in hydrated fullerenol only upon heating and are absent in the quasi-anhydrous sample. These two features (I and III) disappear when heating the sample at 413 K implying that both processes depend directly from the presence of water molecules inside fullerenol. Instead, water moieties only affect process II, which is present also in the absence of water and, as we argument later in this section, is related to a space-charge effect. The values and the temperature dependence of the fit parameters will be discussed to help elucidate their origin.

5.6.1 Fastest and slowest relaxation of water inside fullerenol

The fastest relaxation (process I) is observed at low temperatures and high frequencies. It appears as a broad and symmetric peak, which could be fitted with a Cole-Cole function. The dielectric strength of loss feature I had weak temperature dependence at low temperatures, and then vanished upon dehydration. After heating the sample at the highest temperature where dehydration occurs, it was not observed again upon further cooling and heating cycles. The activation energy of process I was determined as 67.0 ± 0.3 kJ/mol, or approximately 0.69 eV, which is a typical value of water-related relaxations. However, process I is observed at longer relaxation times than the typical secondary relaxation of water.[25] Instead, it is found to match the relaxation times of bulk ice,[26,27] as it can be seen in Figure 5.13. Moreover, by fitting together both our experimental data and the data of reference 26, the average value of the activation energy is ~55.31 ± 0.08 kJ/mol, or approximately 0.58 eV. The high water content rationalizes the existence of bulk-like water in fullerenol below 273 K, where process I is detected. Also the preliminary analysis of hydrated fullerenol (sections 5.3 and 5.4) showed characteristic traits of the presence of bulk-like water, which then disappeared upon heating to high temperature.

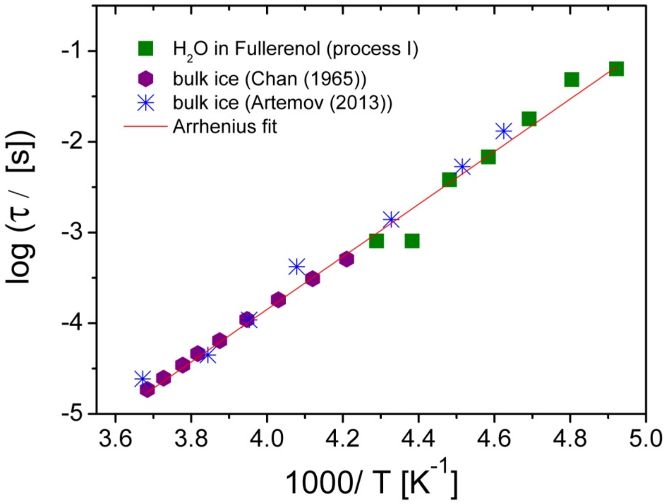

Figure 5.13 Relaxation time of the water-related process I of hydrated fullerenol as a function of reciprocal temperature, in the temperature range 198 - 233 K upon heating. For comparison purposes, we have added the relaxation times of bulk ice from two different studies The red line through the data is the Arrhenius fit of our experimental data and the data taken from references 26 and 27.

Such bulk-like water molecules must be present in relatively large agglomerates, either in-between fullerenol grains or at their surface, or even as confined clusters inside pores with sizes bigger than 3 nm , if present.[28]

Due to its relatively large characteristic times, process I cannot be ascribed to single-water molecule reorientations, as these are observed at much shorter times (see also chapter 4). Its similarity with the relaxation in bulk ice indicates that it corresponds to a relaxation process typical of pure ice. The dielectric feature of pure ice is associated with the diffusion of neutral or ionic orientational defects.[29] In particular, the authors of reference 29 argue that the dielectric response of ice above 230 K is due to the migration of neutral orientational defects (water molecules with an orientation that prevents them to form four hydrogen bonds). As visible in Figure 5.13, the activation energy for process I is identical to that for the diffusion of such defects. The origin of process I in hydrated fullerenol is related in an analogous fashion with the fluctuations of the dipole moments of water clusters in bulk-like ice due to the migration of orientational defects.

Upon further heating, relaxation III entered the experimental window from the low frequency side (above 273 K). This feature displayed a Havriliak-Negami lineshape and was visible till 340 K. Figure 5.14 shows the Arrhenius plot of process III together with relaxations found in other water-containing systems, namely Rh6G[20] (see chapter 4), zeolites[30] and microporous silica[23]. The high similarity of the normal and atypical temperature dependence of process III with the one found in Rh6G implies a common origin of both. The activation energy of process III, as extracted from the Arrhenius slope of the four lowest-temperature spectra (black line in Figure 5.14) was 0.45 eV; a similar value was found in Rh6G (0.49 eV).

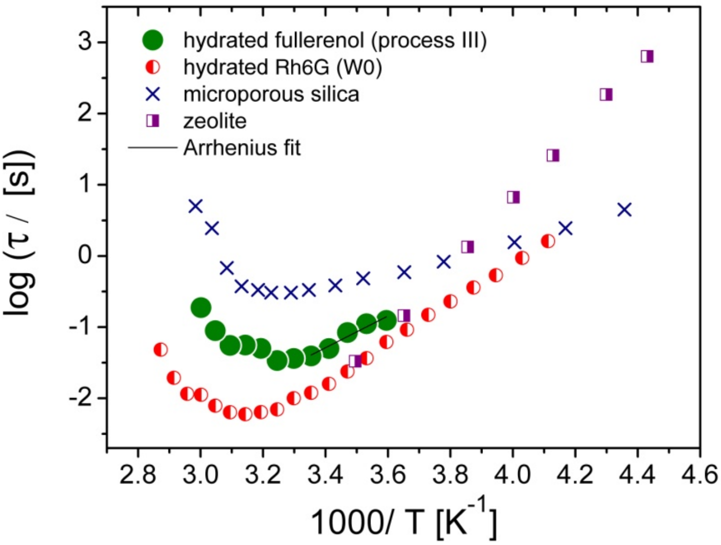

Figure 5.14 Arrhenius plot of the slowest relaxation process III of hydrated fullerenol in the temperature range 278 - 340 K upon heating. The black line through the data of process III is the Arrhenius fit of the low-temperature data. For comparison, the relaxation times of water-containing systems of Rh6G[20], microporous silica[31] and zeolite[30] (are also shown.

As we have seen in section 4.7.1 of the previous chapter, which concerned the atypical behavior of the slowest water-related process in Rh6G (W0), this temperature behavior is associated with the conductivity drop due to the loss of surface water molecules. The same phenomenon was observed not only in the low water-content Rh6G system, but also in the fullerene derivative $C_{60}(ONa)_{24}$, which is very similar to fullerenol, after it is exposed to humid atmosphere.[12] In order to test the validity of the same scenario for the case of fullerenol, we have analyzed the temperature dependence of the dc-conductivity of a hydrated sample (20% H_2O weight) in the temperature range between 298 and 413 K upon heating. The σ_{dc} values were obtained from the low frequency plateau visible in all spectra above 298 K, in the same way as has been done for Rh6G (see chapter 4, section 4.6). The conductivity temperature dependence is also atypical, due to water desorption resulting in non-monotonic behavior of σ_{dc}. In fact, the conductivity undergoes several changes in the whole temperature interval, as Figure 5.15 displays. The temperatures at which these changes occur are correlated with those found in the thermal analysis (DSC), and correspond to different desorption processes of water molecules in different environments. In the figure we have also added the temperature behavior of σ_{dc} upon cooling (413 - 283 K) for comparison. The higher conductivity value in hydrated fullerenol is reminiscent of the conductivity enhancement in inorganic metals and oxides when exposed to humid atmosphere (by exposure to humidity, water condenses onto the material´s surface).[31] It has been shown in a study of $C_{60}(ONa)_{24}$ that the extra conductivity contribution due to surface water is protonic in nature,[19] and that it is likely due to a proton exchange mechanism between adjacent water molecules.[27,32]

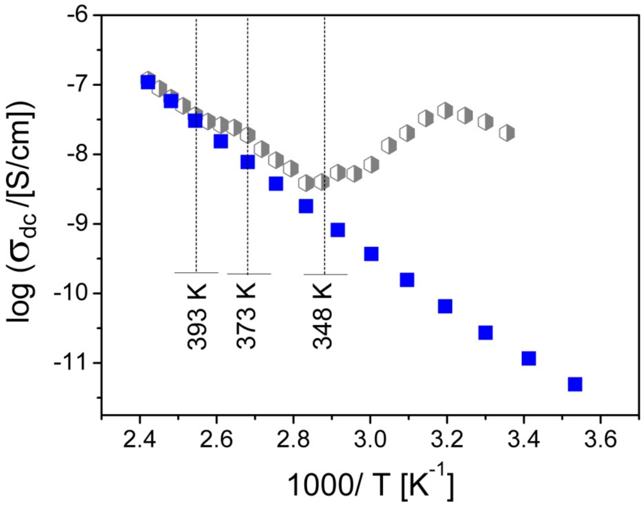

Figure 5.15 Dc-conductivity (σ_{dc}) as a function of the inverse temperature in the range from 298 to 413 K upon heating (grey hexagons) and from 413 K to 283 K upon cooling (blue squares). The annotated temperatures correspond to the thermal changes due to water desorption according to DSC measurements.

In order to check for a possible correlation between process III and the conductivity, in Figure 5.16 (a) we have displayed both the dc-conductivity and the characteristic frequency of process III ($f_{max}(III) = 1/2\pi\tau_{III}$) as a function of temperature (both vertical scales in Figure 5.16 (a) span the same number of decades). The temperature scale ranges from room temperature (298 K) to the temperature at which process III is no longer visible in the loss spectra upon heating (~340 K). The two plots show similar profiles, with a maximum around 310 K. The decrease of both quantities (σ_{dc}, f_{max}(III)) above ~310 K is accompanied by the reduction of the dielectric strength of the relaxation process (Figure 5.16 (b)). These similarities indicate that process III is a space-charge effect associated with the species mainly responsible for the dc conductivity in hydrated fullerenol, namely, protons.

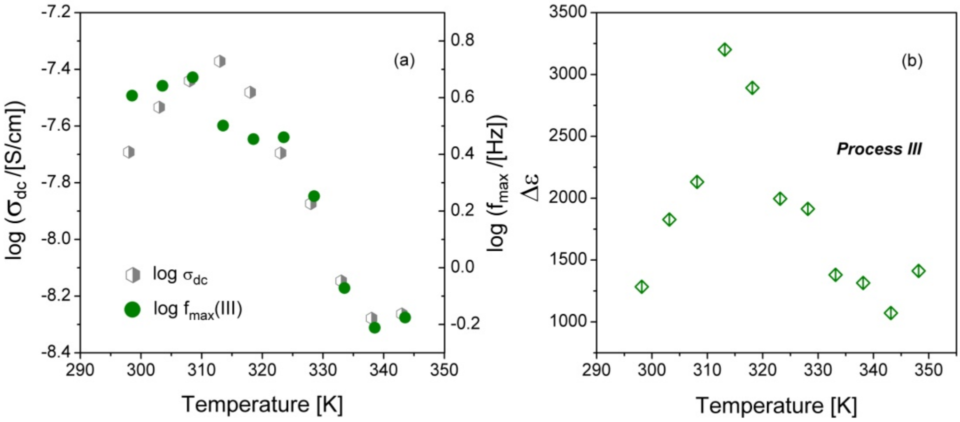

Figure 5.16 (a) Temperature dependence of the dc conductivity (σ_{dc}) and of the relaxation frequency (f_{max}) of process III between 298 and 333 K (data acquired upon heating). (b) Dielectric strength of process III as a function of temperature, upon heating between 298 and 348 K.

The water moieties responsible for the protonic conductivity contribution appear to be only weakly adsorbed onto fullerenol grains, according to their low desorption temperature.

5.6.2 Intermediate relaxation of water inside fullerenol

In this section we deal with the intermediate process II. As we have seen in Figure 5.12 (b), upon cooling from 413 K, process II is the only relaxation that appears in dielectric spectra of the quasi-anhydrous sample obtained by heating hydrated fullerenol to 420 K. This behavior entails that this process cannot originate only from the contribution of water molecules.

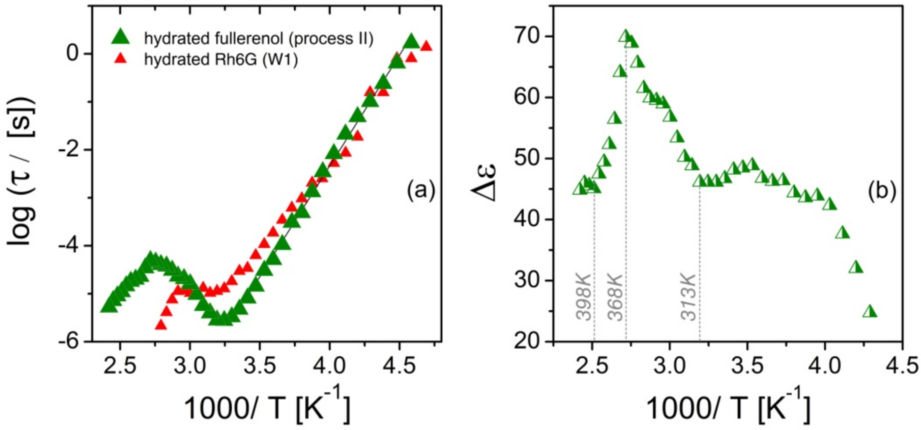

Figure 5.17 (a) Arrhenius plot of the relaxation process II of a hydrated fullerenol in the temperature range 218 - 413 K upon heating. The black line through the linear part of the data of process III is the Arrhenius fit. The relaxation times of process W1 of hydrated Rh6G are also shown. (b) Dielectric strength of process II as a function of the inverse temperature in the same temperature range.

The relaxation time of process II upon heating from low temperature is quite close to that of the W1 relaxation of Rh6G, as it can be seen in the Arrhenius plot of Figure 5.17 (a). The activation energy of the simply-activated portion of process II (the low-temperature region) is 0.92 eV, which is a bit higher than that of W1 relaxation, as one can conclude from the steeper slope of process II. The non-monotonic behavior of fullerenol is more prominent than in Rh6G, probably due to higher water content in the former.

As we can observe from both panels of Figure 5.17, both the relaxation time and the dielectric strength display non-monotonic behavior upon heating between 310 and 400 K. While feature III is not visible above 340 K, feature II displays the most dramatic changes above this temperature (see also Figure 5.9). Above 370 K, both the characteristic time and dielectric strength of process II decrease with increasing temperature. The temperature of 370 K marks the desorption of strongly bound water molecules, according to thermal analysis (see section 5.3). Above 398 K, feature II displays a broader and more asymmetric profile, and it shifts to higher frequency with increasing temperature with constant dielectric strength.

After heating to the highest measured temperature (~420 K), water content in fullerenol undergoes a significant reduction. Upon subsequent cooling, only one process is present in the dielectric spectra (see Figure 5.12), namely process II. This process upon cooling appears at longer times than its analogous process upon heating, due to the loss of water. In order to test the correlation of process II with the conduction mechanisms inside fullerenol, it is more suitable to study a sample with the lowest water content. Thus, in Figure 5.18 we have plotted the temperature dependence of both dc-conductivity and frequency of the loss maximum for process II (f_{max} (II)) upon cooling in the same Arrhenius plot (both vertical scales in Figure 5.18 span the same number of decades).

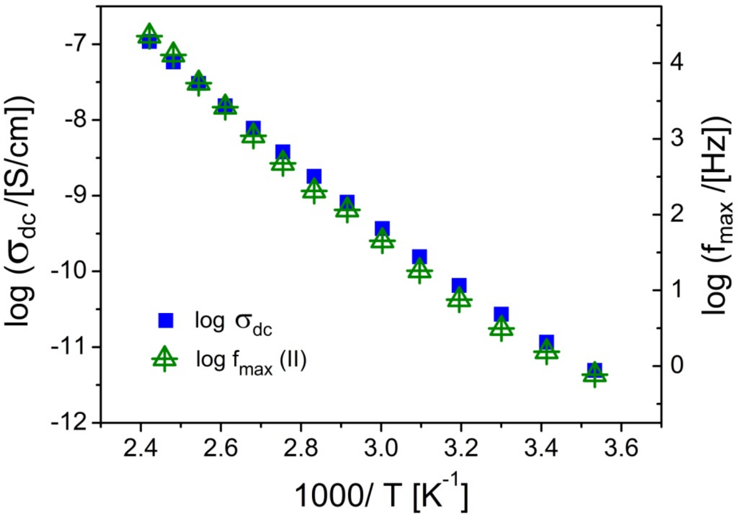

Figure 5.18 Arrhenius plot of the dc conductivity (σ_{dc}) compared with the relaxation frequency (f_{max}) of process II at the temperature range between 413 and 283 K, upon cooling down.

Process II is associated with the long range conductivity mechanisms of quasi-anhydrous fullerenol. As it can be seen above, the water molecules that remain trapped within the material´s matrix do not induce any contribution to the consistency between charge transport mechanisms and dielectric loss II. In order to prove furthermore the similarity of both quantities, we consider the quantity f_σ defined as $f_\sigma = \sigma_{dc}/2\pi\varepsilon_0\Delta\varepsilon(II)$, where $\Delta\varepsilon$(II), is the dielectric strength of feature II. As we already discussed in chapter 4, the frequency f_σ is correlated with the long-range conductivity and is in fact the characteristic relaxation frequency of spatial charge fluctuations in a conducting medium. It is seen in Figure 5.19 that the slope of the logarithmic plot of f_{max} (II) as a function of f_σ is unity, which entails a perfect (linear) correlation between the dielectric loss and the dc-conductivity.

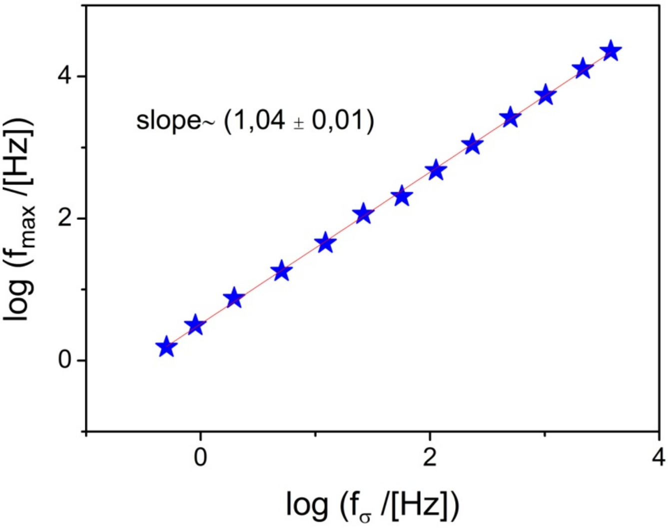

Figure 5.19 Plot of the relaxation frequency of process II (f_{max}) upon cooling (413 - 283 K) versus the characteristic relaxation frequency (f_σ) of spatial charge fluctuations for the same temperature interval. Both frequencies are in logarithmic form.

Consequently, process II upon cooling is a conductivity related space-charge relaxation, also known as Barton-Nakajima-Namikawa (BNN) relaxation (see section 2.4). The simplest explanation of the loss feature is the accumulation of the charges at the surface of fullerenol grains, which after the loss of water are disconnected.

By studying the temperature dependence of the dc-conductivity of the quasi-anhydrous sample, we can identify the type of conduction in pure fullerenol.[33]From Figure 5.20 (a), we can see that the plot of σ_{dc} versus 1000/T deviates slightly from the simply activated Arrhenius behavior (straight line in the Arrhenius plot), displaying in fact a slight positive curvature. This curvature is also visible from the increase of the apparent activation energy with increasing temperature (Figure 5.20 (b)).

The activation energy is calculated as the first derivative of the σ_{dc} plot, namely $E_a(\sigma_{dc}) = -\frac{d\,(\ln\sigma_{dc})}{d(1/k_BT)}$, where k_B is the Boltzmann constant.

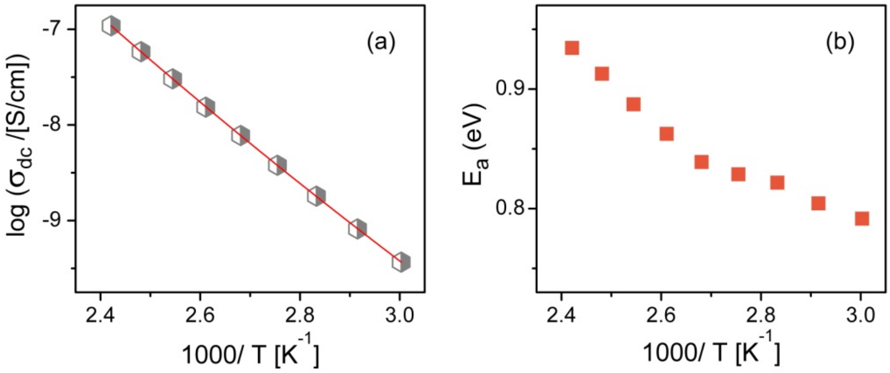

Figure 5.20 (a) Arrhenius plot of the σ_{dc} conductivity in the temperature interval 413 - 333 K, upon cooling. The red line through the data is a power-law fit function (see text). (b) Effective activation energy of the σ_{dc} curve, as a function of the inverse temperature for the same temperature interval.

The non-Arrhenius temperature dependence of σ_{dc}) is consistent with a certain type of conduction, namely the hopping electronic conduction.[34,35] The experimental temperature dependence of σ_{dc} was fitted assuming a power-law dependence of the form $\log(\sigma_{dc}) = A - \frac{B}{T^n}$.[19] The result of the fit for different samples gave a value of the power *n* of 0.43 ± 0.05. This value is very close to the theoretical value of 1/2 that corresponds to variable-range hopping electronic conductivity[36,37], and which is observed experimentally in a large variety of systems.[38,39] This type of conduction found in the quasi-anhydrous fullerenol is the most common conduction mechanism in disordered organic semi-conductors,[40] and may be expected in electron-acceptors such as C_{60} and its derivatives.

Having identified process II in anhydrous fullerenol as a genuine space-charge relaxation associated with electronic hopping, we now discuss the interpretation of this feature in hydrated fullerenol. It is clear that the presence of the water molecules on the surface of the fullerenol grains or within them will have an impact on the electronic space-charge loss. The water moieties that are expected to affect most strongly the accumulation of electrons at grain boundaries are the molecules sitting directly at the boundary, which therefore interact directly with the fullerenol matrix. This expectation is verified by the positive slope of the plot of its Cole-Cole exponent as a function of its relaxation times [41](Figure 5.21).

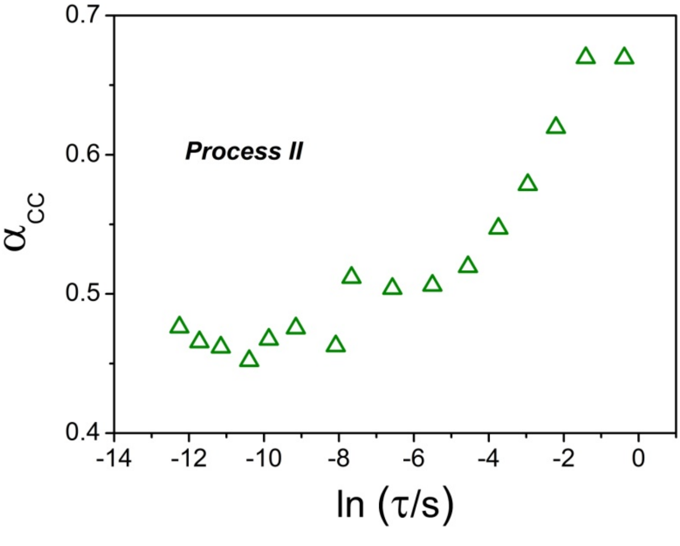

Figure 5.21 Dependence of the Cole-Cole α_{CC} exponent on ln(τ) for the intermediate water relaxation II in fullerenol upon heating between 223 and 298 K.

In order to study the similarities between process II and the conductivity in the hydrated sample, in Figure 5.22 we have plotted together in the same Arrhenius plot the dc-conductivity and the characteristic frequency of process II (f_{max}(II)) as measured upon heating (for temperatures above 350 K). It is seen that at temperatures higher than 368 K the temperature dependence~~s~~ of both quantities are identical, which is again expected for a space-charge relaxation, while below this temperature the two quantities are uncorrelated due to the fact that the conductivity is dominated by proton hopping at lower T.

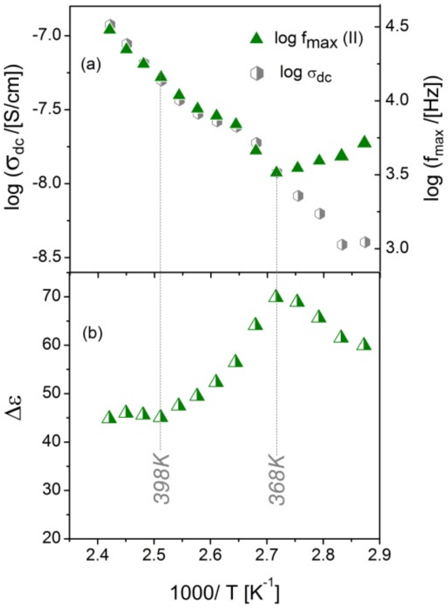

Figure 5.22 (a) Arrhenius plot of the dc conductivity (σ_{dc}) and of the relaxation frequency (f_{max}) of process II between 348 and 413 K, upon heating. (b) Dielectric strength of process II as a function of the inverse temperature in the same temperature range.

However, as shown in Figure 5.23, the slope of the logarithmic plot of f_{max}(II) *versus* f_σ is significantly lower than unity, implying that the two are not linearly correlated, and therefore that the loss feature is not a simple BNN relaxation. A similar behavior was observed also in $C_{60}(ONa)_{24}$.[12]

Notice that the temperature range of Figure 5.23 is above the region where proton conduction dominates. Hence, the lack of validity of the BNN relation is not due to a non-electronic conductivity; instead, we argue that it is associated with the large polarizability of the interfacial water molecules and with a contribution of surface water to the interfacial dipole moment.

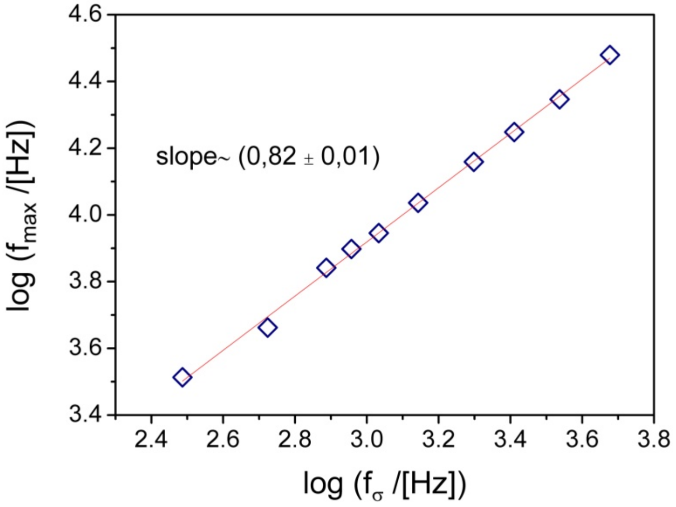

Figure 5.24 Logarithmic plot of the relaxation frequency of process II (f_{max}) upon heating (363 - 413 K) versus the characteristic relaxation frequency (f_σ) of spatial charge fluctuations for the same temperature interval.

A behavior similar to that of the dielectric relaxation II in hydrated fullerenol was observed also on a hydrated melanin polymer upon heating and cooling cycles. Loss of bound water upon heating resulted in modifications of the relaxation process of hydrated melanin, which was found to display quite similar behavior as process II upon heating.[42]

The contribution of interfacial water dipoles to the dielectric process II upon heating in the hydrated sample corroborates our interpretation of feature II as a space-charge relaxation associated with charge accumulation at grain boundaries. The exact microscopic mechanism by which the interfacial water molecules modify the space-charge relaxation of the electronic charge carriers is yet unknown.

5.7 Conclusions

The hydrophilic and hygroscopic behavior of an oxygen-containing C_{60} derivative has verified in this study. Hydrated fullerenol samples contain 20% in weight of hydration water, mainly present at the surface of the fullerene grains. The water molecules occupy different molecular environments within the material, as observed in thermal spectroscopic studies.

Bulk-like water has been identified in such studies by observing the melting of ice clusters at 273 K in hydrated fullerenol. The presence of ice is also detected with dielectric spectroscopy, by the existence of a relaxation below 230 K which is due to the diffusion of orientational defects throughout the bulk water network (process I). The hydration water introduces a new conduction mechanism at sufficiently high hydration level, which is the same as in bulk water or ice, namely the Grotthus proton exchange conduction. This new conduction mechanism and pathway also entails the existence of a protonic space-charge relaxation associated with the proton hopping, which is visible at higher temperature, close to the temperature of water desorption (process III). Besides these two relaxations, associated directly with a dielectric response of water moieties present in large-enough quantities (several hydration layers or clusters), another one is observed at intermediate temperatures (process II). The fact that this relaxation is also present in a quasi-anhydrous sample, where the conductivity is due to electronic charge carriers, and that the pure material is not expected to display any intrinsic orientational relaxation imply that process II has an electronic space-charge origin. When the powder is hydrated, the large polarizability of the surface water molecules contributes to this interfacial relaxation, thus modifying its properties and temperature dependence.

Bibliography

[1] Mchedlov-Petrossyan *Chem. Rev.*, vol. 113, p. 5149, 2013.

[2] J.D. Fortner, D.Y. Lyon, C.M. Sayes, A.M. Boyd, J.C. Falkner, E.M. Hotze, L.B. Alemany, Y.J. Tao, W. Guo, K.D. Ausman, V.L. Colvin, J.B. Hughes *Environ. Sci. Technol.*, vol. 39, p. 4307, 2005.

[3] T. Da Ros, M. Prato, *Chem. Commun.*, vol. 8, p. 663, 1999.

[4] S. Wang, P. He, J.M. Zhang, H. Jiang, S.Z. Zhu *Synth Commun.*, vol 35, p.1803, 2005.

[5] J. Li, A. Takeuchi, M. Ozawa, X. Li, K. Saigo, K. Kitazawa *J. Chem. Soc. Chem. Commun.*, vol. 23, p. 1784, 1993.

[6] L. Echegoyen, F. Diederich, L.E. Echegoyen; Electrochemistry of fullerenes. *In: Fullerenes: Chemistry, Physics, and Technology*; Ruoff, R.S., Eds.; John Wiley & Sons, Inc.: New York, pp. 1-51, 2000.

[7] R. Macovez, A. Goldoni, L. Petaccia, I. Marenne, P.A. Brühwiler, P. Rudolf *Phys. Rev. Lett.*, vol. 101, p. 236403, 2008.

[8] P.J. Bracher, D.I. Schuster; Electron transfer in functionalized fullerenes. *In: Developments in Fullerene Science: Fullerenes: From Synthesis to Optoelectronic Properties*; Guldi, D.M.; Martin, N., Eds.; Springer, vol. 4, pp. 163-212, 2002.

[9] K. Tasaki, A. Venkatesan, H. Wang, B. Jousselme, G. Stucky, F. Wudl *J. Electrochem. Soc.*, vol. 155, B1077, 2008.

[10] G. Bogdanovic, V. Kojic, A. Dordevic, J. Canadanovic-Brunet, M. Vojinovic-Miloradov, V. Vit. Baltic *Toxicology in Vitro*, vol. 18, p. 629, 2004.

[11] F. Michaud, M. Barrio, S. Toscani, D.O. López, J.L. Tamarit, V. Agafonov, H. Szwarc, R. Céolin *Phys. Rev. B.*, vol. 57, p. 10351, 1998.

[12] M. Zachariah, E. Mitsari, M. Romanini, P. Zygouri, D. Gournis, M. del Barrio, J.L.Tamarit, R. Macovez *J. Phys. Chem. C.*, vol. 119, p. 685, 2015.

[13] R. Rivelino, T. Malaspina, E.E. Fileti *Phys. Rev. A.*, vol. 79, 013201, 2009.

[14] H. He, L. Zheng, P. Jin, M. Yang *Computational and Theoretical Chemistry* (Comptc)., vol. 974, p. 16, 2011.

[15] B. Vileno, P.R. Marcoux, M. Lekka, A. Sienkiewicz, T. Fehér, L. Forró *Adv. Funct. Mater.*, *vol.* 16, p. 120, 2006.

[16] S. Cerveny, F. Barroso-Bujans, Á. Alegría, J. Colmenero J. *Phys. Chem. C.*, vol 114, p. 2604, 2010.

[17] B. Brubach, A. Mermet, A. Filabozzi, A. Gerschel, P. Roy *J. Chem Phys.*, vol. 122, p. 184509, 2005.

[18] P. A. Indeglia, A. Georgieva, V.B. Krishna, J-C. J. Bonzongo *J Nanopart Res.*, vol. 16, p. 2599, 2014.

[19] R. Macovez, M. Zachariah, M. Romanini, P. Zygouri, D. Gournis, J.L.Tamarit, *J. Phys. Chem. C.*, vol. 118, p. 12170, 2014.

[20] R. Macovez, E. Mitsari, M. Zachariah, M. Romanini, P. Zygouri, D. Gournis, J.L.Tamarit, *J. Phys. Chem. C.*, vol. 118, p. 4941, 2014.

[21] Kremer, A. Schönhals *Broadband Dielectric Spectroscopy.* Berlin: Springer, 2002.

[22] S. Cerveny, S. Arrese-Igor, J.S. Dolado, J.J. Gaitero, A. Alegría, J. Colmenero *J. Chem Phys.*, vol. 134, p. 034509, 2011.

[23] J. Sjöström, J. Swenson, R. Bergman, S. Kittaka *J. Chem Phys.*, vol. 128, p. 154503, 2008

[24] M. Wübbenhorst, J. van Turnhout *J. Non-Crist. Solids.*, vol. 305, p. 40, 2002.

[25] K.L. Ngai, S. Capaccioli, S. Ancherbak, N. Shinyashiki *Phil. Mag.*, vol. 91, p. 1809, 2011.

[26] R.K. Chan, D.W. Davidson, E.J. Whalley *J. Chem. Phys.*, vol 43, p.

2376, 1965.

[27] V.G. Artemov, A.A. Volkov *cond-mat.soft* arXiv:1308.1229, 2013.

[28] M. Monasterio, H. Jansson, J.J. Gaitero, J.S. Dolado, S. Cerveny *J. Chem Phys.*, vol. 139, p. 164714, 2013.

[29] I. Popov, A. Puzenko, A. Khamzin, Y. Feldman *Phys. Chem. Chem. Phys.,* vol 17, p. 1489, 2015.

[30] L. Frunza, H. Kosslick, S. Frunza, A. Schönhals *J. Phys. Chem.*, vol. 106, p. 9192, 2002.

[31] M.M. Ahmad, S.A. Makhlouf, K.M. Khalil *J. Appl. Phys.*, vol. 100, p. 094324, 2006

[32] J.H. Anderson, G.A. Parks *J. Phys. Chem.*, vol. 72, p. 3662, 1968.

[33] E. Mitsari, M. Romanini, M. Zachariah, R. Macovez *Curr. Org. Chem.*, vol 20, p. 645, 2016.

[34] H. Han, C. Davis, III, J.C. Nino *J. Phys. Chem.*, vol. 118, p. 9137, 2014.

[35] S. Capaccioli, M. Luchessi, P.A. Rolla, G. Ruggeri *J. Phys: Condens. Matter.*, vol. 10, p. 5595, 1998.

[36] M.P.J. Van Staveren, H.B. Brom, L.J. De Jongh *Phys. Rep.*, vol 208, p. 1, 1991.

[37] B.I. Shklovskii, A.L. Efros *Electronic Properties of Doped Semiconductors*; Springer: Berlin, 1984.

[38] L.J. Huijbregts, H.B. Brom, J.C.M. Brokken-Zijp, M. Kemerink, Z. Chen, M.P. De Goeje, M. Yuan, M.A.J. Michels *J. Phys. Chem. B*, vol. 110, p. 23115, 2006.

[39] D. Yu, C. Wang, B.L. Wehrenberg, P. Guyot-Sionnest *Phys. Rev. Lett.*, vol. 92, p. 216802, 2004.

[40] W. Brutting, Ch. Adachi *In Physics of organic Semiconductors, 2nd ed.*; Eds.; Wiley: Chichester, 2012.

[41] A. Puzenko, P.B. Ishai, Y. Feldman P *Phys. Rev. Lett.*, vol. 105, p. 037601, 2010.

[42] M. Jastrzebska, A. Kocot, J.K. Vij, J. Zalewska-Rejdak, T. Witecki *J. Mol. Struct.,* vol. 606, p. 205, 2002.

Chapter 6

ORIENTATIONAL TRANSITIONS & CONDUCTIVITY-INDUCED EFFECTS IN SOLID OXOFULLEROL

6.1 Introduction

Fullerene molecules display highly symmetric, quasi-spherical shapes, and interact via intermolecular forces of dispersive (van der Waals) origin. These features of fullerenes lead, in the solid state, to the existence of plastic-crystalline phases, glassy transitions, and in general to interesting rotational dynamics. Rotational motions and transitions are reported in the solid phases of pristine fullerenes and of some simple derivatives, as well as in co-crystals and solvates with smaller organic molecules.[1] For example, in solid C_{60} the molecules rotate very rapidly at room temperature, resulting in a high-symmetry orientationally disordered face-centered cubic (fcc) structure. Below 260 K this free-rotor motion is reduced to a ratcheting motion between two preferred orientations (such transition displays a temperature hysteresis of 5 K).[2,3] The merohedral twinning motion of the C_{60} molecules finally freezes out at a glassy transition at 90 K, below which the lattice structure still remains simple cubic (sc).[4,5] The simple derivatives $C_{60}O$ and $C_{61}H_2$

display analogous transitions, albeit at slightly higher temperature than C_{60}. It has been shown that the slight increase in the transition temperatures originates from the lower entropy of dynamically-disordered phases of fullerene derivatives with respect to C_{60} (since the side groups must occupy octahedral or tetrahedral voids).[6,7] This suggests that also in pristine fullerite the orientational transitions are entropy-driven, and in the case of $C_{60}O$ it indicates that the stronger (dipolar) intermolecular interactions due to the presence of epoxy moiety have instead a negligible effect on the transition temperature.

In this chapter we study a novel fullerene derivative, synthesized with the well-known Staudenmaier method,[8] already applied for the chemical oxidation of graphite.[9] The covalent functionalization produces oxygen functional groups such as epoxy, carbonyl and hydroxyl onto the C_{60} surfaces, thus enhancing the water solubility of the fullerene moieties.

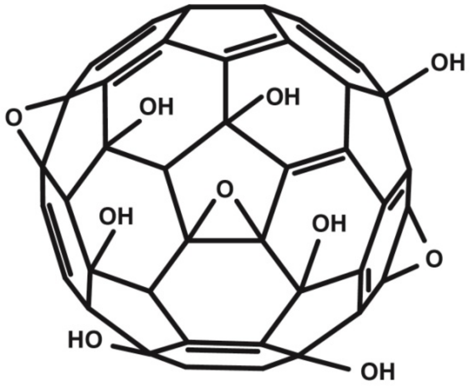

Figure 6.1 Molecular structure of the oxofullerenol molecule (oxC_{60}).

We will refer to this recently synthesized C_{60} derivative as oxofullerenol (hereafter oxC_{60}). It has been found from X-ray photoelectron spectroscopy (XPS) characterization that the chemical composition is similar to that of fullerenol molecules ($C_{60}(OH)_n$), but with extra oxygen groups, at least some of which are epoxy bridges (Figure 6.1). The average chemical formula of oxC_{60} is $C_{60}(OH)_{14}O_n$, with n between 4 and 8.[10]

As it will be shown in this chapter, oxC_{60} displays interesting orientational dynamics, with rotational transitions reminiscent of those of C_{60}, which were described above. As one may expect, the presence of both hydroxyl groups and epoxy/carbonyl oxygens results in the formation of hydrogen bonds which hinder the rotational motions at low temperature. These bonds are broken at higher temperature, leading to rotational dynamics.

We find that, like pristine C_{60} and many of its derivatives, water-free oxC_{60} shows semiconducting or insulating behavior in the solid state. The charge transport is probably due to electrons/holes introduced by thermal excitation and by the presence of defects or impurities, as in other organic semiconductors. The phase transitions are detected, in the dielectric spectra, through their impact on the charge conduction properties of the sample.

6.2 Experimental Methods

Oxidized buckminsterfullerene (oxC_{60}) was obtained by a modified Staudenmaier’s method.[8]Briefly, C_{60} (98%, Sigma-Aldrich) was added to a 2 to 1 mixture of H_2SO_4 (95-97%) and HNO_3 (65%) while cooling in an ice-water bath (at 0°C). $KClO_3$ was then added in small portions under vigorous stirring. The reaction was completed after 18 hours and then acetone was added and the mixture was stirred for another day. The oxidation product was separated by centrifugation, washed with distilled water until a pH 6 and air-dried on a glass plate. The remaining solid is highly soluble in polar solvents like water. The synthesis of the samples was carried out at the laboratories of Ceramics and Composites group at the University of Ioannina in Greece.

FT-IR characterization was carried out at the centre for research in nanoengineering of the UPC (CRnE). FTIR spectra were measured in the mid-infrared range (4000 – 400 cm^{-1}) on samples which were prepared in pellet form with the addition of potassium bromide (KBr). Due to the hygroscopic nature of KBr, we keep the powder to the furnace (373 K) for 20 hours prior to the measurement. Measurements were conducted at room temperature on the as-stored (partially hydrated) sample and on a sample pre-heated to 365 K.

For the thermal analysis of oxC_{60}, thermogravimetry (TGA) and differential scanning calorimetry (DSC) were employed. TGA scans were acquired while heating the sample under N_2 flow between 300 and 630 K at a rate of 5 K/min. DSC was performed between 290 and 400 K with a heating/cooling rate of 5 K/min. The samples were weighed before and after the measurements.

High-resolution X-ray powder diffraction (XRD) profiles of pure oxC_{60} samples were recorded over a 2θ range between 4° and 120° (with an angular step of 0.029° (2θ)), at various temperatures with a typical acquisition time of 4 hours for each temperature. For XRD measurements, the powder sample was placed into a Lindemann capillary tube (0.5 mm diameter) and the temperature was controlled with a N_2 gas flow.

Dielectric spectroscopy (BDS) data were acquired on pellets placed between two steel disks in parallel-plate capacitor geometry. The pellets were obtained by using a hydraulic press (20 kN), and their thickness was between 0.10 and 0.15 mm. Dielectric measurements were performed every 2 K (with a temperature stability of ±0.5 K) between 293 and 408 K in the frequency range from 10^{-2} Hz to 10^{7} Hz (see chapter 3). In order to measure pure (dehydrated) samples, we preheated the pellets to 365 K prior to BDS measurements, to remove the hydration water adsorbed onto the material upon storage in air.

6.3 FTIR analysis of oxC$_{60}$

Fourier-transform infrared spectra were acquired at room temperature on a pellet made with the as-stored oxC$_{60}$ powder in the mid-infrared range. Due to the chemical similarity of oxC$_{60}$ with fullerenol, which we have studied in the previous chapter, several spectroscopic characteristic peaks coincide, which simplifies the identification of the oxC$_{60}$ spectral features. Figure 6.2 shows the FTIR spectrum of an as-stored pellet, which is indeed reminiscent of the fullerenol spectrum (see Figure 5.4 in chapter 5).

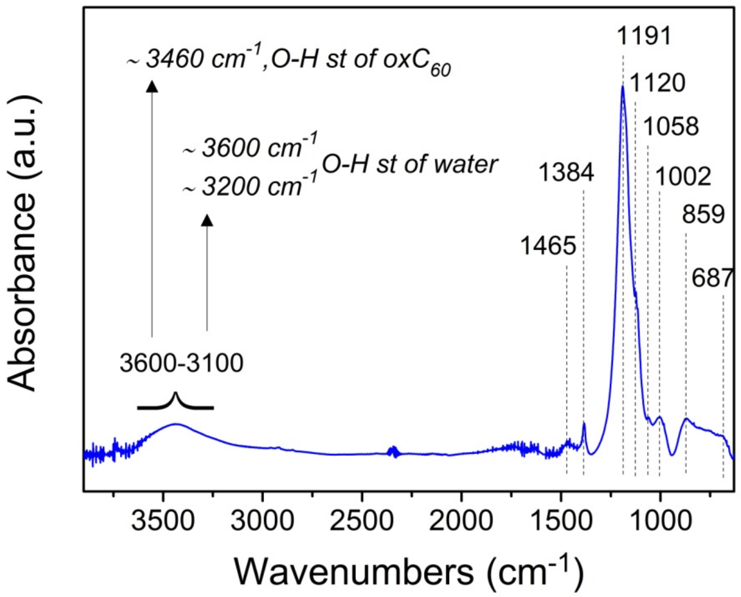

Figure 6.2 FT-IR spectrum of an as-stored oxC$_{60}$ sample. The absorption bands that could be assigned to oxofullerenol or water vibrations are marked by vertical dotted lines onto the spectrum.

Starting from the low wavenumbers, the bands at 687 and 859 cm^{-1} are assigned to the O-H waggings of the hydroxyl groups onto the C$_{60}$ buckyballs. The next three bands are associated with the C-O stretching vibrations,[11,12] observed at 1002, 1058 and 1120 cm^{-1}. The extremely intense band at 1191 cm^{-1} is characteristic of the potassium sulfate salt (K_2SO_4), which is present as impurity in the oxC$_{60}$ sample (see section 6.5). Such salt is a by-product of the strong oxidation process. The mentioned band corresponds to the stretching vibration of the S-O bonds in K_2SO_4.[12]At slightly higher wavenumber, the bands at 1384 cm^{-1} and 1465 cm^{-1} are characteristic of the C-OH bending modes.[13,14,15] Finally, at the high wavenumber limit of the experimental range, a very broad feature is observed, centered at approximately 3450 cm^{-1}, which originates from a wide distribution of O-H vibration frequencies, corresponding both to the OH groups of the oxC_{60} molecules[13,15] and those of water impurities (see Section 6.4). Indeed, an FT-IR spectrum acquired at room temperature after heating the pellet to 365 K shows a reduction of intensity of the broad feature, while the other bands remain unchanged (not shown).

The analysis of the high-frequency feature in oxC_{60} by means of a Gaussian fit proves even more complicated than in the case of fullerenol, due to the broad and featureless spectral profile. It is likely that part of the difficulty arises due to the presence of a hydrogen bond network within hydrated and pure oxC_{60}, as we discuss in the next section.

6.4 Thermal behavior of as-stored and water-free oxC_{60}

The oxygen-containing groups attached covalently onto the C_{60} moieties leads in some cases to hygroscopic behavior, as we have observed in the previous chapter. The chemical composition of oxC_{60} is similar to that of fullerenol molecules ($C_{60}(OH)_n$), but with extra oxygen groups (epoxy bridges). Similarly to the case of $C_{60}(OH)_{24}$ (see chapter 5)[16] and other oxidized C_{60} derivatives such as $C_{60}O_{24}Na_{24}$,[17]oxC_{60} shows hygroscopic behavior. This may be gathered from Figure 6.3 (a), where the TGA curve measured on an as-stored oxC_{60} powder is shown. A first mass loss may be observed below 400 K, which is due to the water desorption. This mass loss is lower in the case of oxC_{60} compared to fullerenol (see section 5.3), indicating a lower water content. The lost mass corresponds to ~2% of water content, which using the chemical formula for oxC_{60} leads to an average of roughly 2 water molecules per oxC_{60} moiety. Water desorption occurs at relatively low temperature, namely ~350 K, the temperature of the first water loss in fullerenol (see

Figure 6.3 (b)). This “secondary water” is physisorbed onto the outer surface of the material´s grains, and it is present in the samples due to their continuous contact with (normal or relatively humid) atmospheric conditions.[16,17] The dehydration process was also observed in the scanning calorimetry data acquired on oxC_{60} samples upon heating to 370 K (not shown). The dehydration process was visible in the DSC thermograph between 350 and 365 K. Thus, we can obtain a pure (water-free) oxC_{60} powder only by annealing to ~365 - 370 K in nitrogen atmosphere in order to remove the physisorbed water.

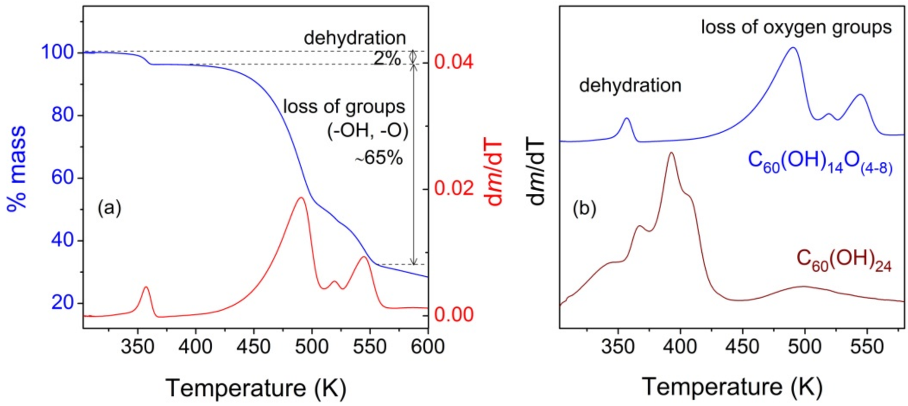

Figure 6.3 (a) TGA thermograph of hydrated oxC_{60} (blue line, left y-axis) and its first derivative (red line, right y-axis), in the temperature range 303 - 600 K. For each mass loss, the corresponding lost moieties and the loss percentage are indicated. The heating rate is 5 K/min. (b) First derivative of the TGA thermographs of oxC_{60} (blue line) and fullerenol (wine line) samples at temperatures between 303 K and 580 K.

Between approximately 450 and 550 K, both fullerenol and oxC_{60} show a further mass loss, much more significant in the latter than in the former (Figure 6.3 (b)). In fullerenol, this high-temperature mass loss is associated with the loss of the covalently bonded hydroxyl groups.

Given the similar chemical formula it is natural to assign the mass loss in oxC_{60} in the same temperature interval to the breaking of the covalent C-O bonds of hydroxyl and epoxy moieties (Figure 6.3 (a)). However, the high percentage (~65%) of the second mass loss in this case indicates that the breaking of C-O bonds actually marks the onset of decomposition of the C_{60} derivative, which takes place in different steps until its total decomposition at $T > 623$ K. The decomposition of oxC_{60} appears to occur in three steps, as it can be discerned from the first derivative of the TGA graph in Figure 6.3a. The first step occurs between 425 and 500 K and it leads to the highest mass loss (~42%) of the three. Due to the similar onset temperature of decomposition and the similar chemical formulas of fullerenol and oxC_{60}, we assign the first decomposition step of oxC_{60} to the loss of the hydroxyl groups and of other oxygen-containing groups.

Figure 6.4 displays the DSC data acquired on the water-free oxC_{60} sample (obtained by heating the as-stored powder to 370 K) during a heating cooling cycle between 290 and 400 K. The pure oxC_{60} material displays two main endothermic transitions with onset upon heating at 320 and 372 K, respectively, and a minor one with onset at 337 K. All three transitions are solid-to-solid (no liquid phases are observed in fullerene systems), fully reversible in the temperature range of the experiment, and exhibit a thermal hysteresis of 4 - 8 K between heating and cooling (onset-to-onset). The observation of solid-solid first-order reversible transitions in oxC_{60} is reminiscent of the temperature-dependent phase behavior of pristine fullerite, C_{60} solvates, and simple derivatives such as $C_{60}O$ and $C_{61}H_2$, which exhibit glassy and order-disorder transitions involving the orientational degrees of freedom of the constituent molecules.[6, 18] The thermal hysteresis of 4-8 K of the transitions of oxC_{60} is similar to the value observed in rotational transitions of pristine C_{60}.[2,3,4,5]

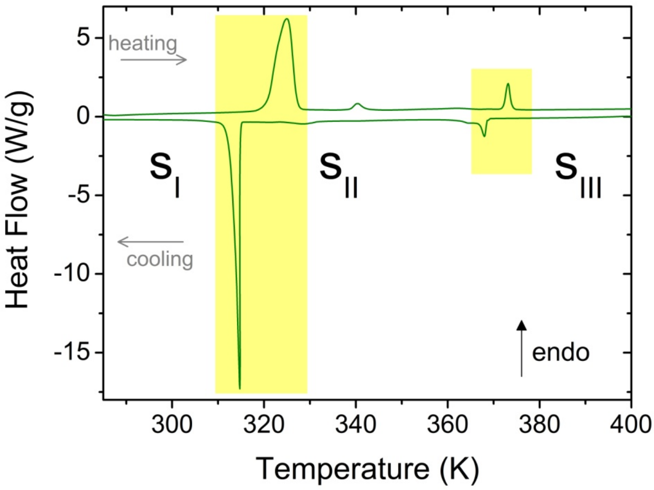

Figure 6.4 DSC thermograph of pure (water-free) oxC_{60} in a heating-cooling cycle between 290 and 400 K. The heating and cooling rates were both 5 K/min. The yellow regions indicate the temperature ranges of the (reversible) phase transitions. The symbols s_I, s_{II} and s_{III} indicate the different orientational phases of solid oxC_{60}.

The transition enthalpies of the two main phase transitions are 100 ± 15 J/g (320 K) and 8 ± 1 J/g (372 K). In terms of molar quantities, this yields 105 ± 20 kJ/mol (320 K) and 8.5 ± 1.5 kJ/mol (372 K), where the error takes into account both the variation between samples and the uncertainty in the chemical formula $C_{60}(OH)_{14}O_n$ with n between 4 and 8, leading to a molecular mass between 1022 and 1086 a.m.u. As mentioned in the Introduction, the oxC_{60} derivative contains hydroxyl, epoxy and possibly carbonyl groups. The presence of both hydrogen and oxygen atoms on the surface of the oxC_{60} molecule entails that hydrogen bonds can be formed between next-neighbor molecules. The large transition enthalpy of the phase change at 320 K indicates that this transition involves the breaking of hydrogen bonds between the hydroxyl group of a molecule and the epoxy (or carbonyl) oxygen of a neighboring oxC_{60} molecule. This is also confirmed by the calorimetry results on the partially decomposed material obtained after heating to 500 K, shown in Figure 6.5. In fact, from TGA results (see Figure 6.3) we know that the mass loss between 425 and 500 K is associated to the loss of the OH and other oxygen-containing groups covalently attached onto C_{60} spheres. Thus, the absence of the transition at 320 K in the DSC thermogram of a sample heated to 500 K confirms that such transition involves the H-bonding groups (-OH, -O, =O) of the pristine oxC_{60} molecules.

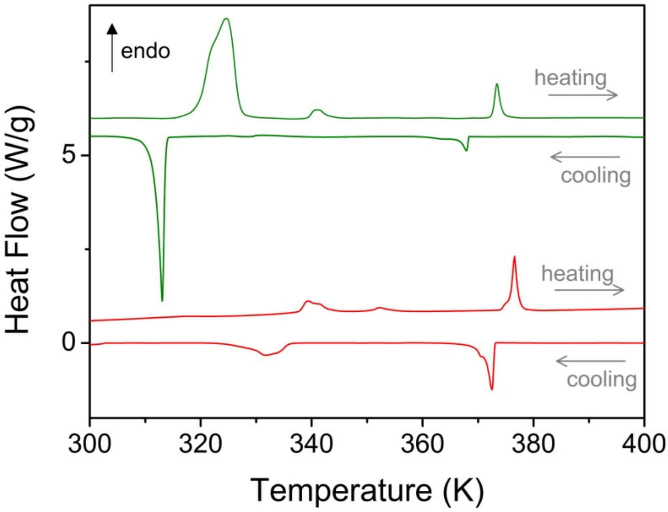

Figure 6.5 Differential scanning calorimetry thermograms acquired in a heating-cooling cycle between 300 and 400 K on a sample preheated to 400 K to remove physisorbed water (green line), and on a sample preheated to 500 K to induce the loss of hydrogen-bonding groups (red line) (see text for details). The heating/cooling rate is 5 K/min for both DCS measurements.

It may be observed that the material obtained by annealing to 500 K still displays two of the three phase transitions observed in pristine water-free oxC_{60}, which suggests that the fullerene cages still maintain their integrity up to at least 500 K.

6.5 X-ray diffraction study of the pure (water-free) compound

In order to study the solid-to-solid phase transitions recorded in the calorimetry measurements on pure oxC_{60} (section 6.4), an X-ray diffraction study was performed. The XRD patterns acquired at various temperatures showed a number of diffraction peaks, indicative of the fact that the oxC_{60} powder is polycrystalline. The diffraction profiles of oxC_{60} are quite different from that of face-centered cubic fullerite (Figure 6.6), which confirms the successful functionalization of C_{60} during synthesis.

The diffraction pattern of oxC_{60} is strongly temperature-dependent: while a large number of peaks is observed at room temperature, as the temperature is raised some of the peaks disappear from the pattern (Figure 6.6). This is not only indicative of a more symmetric high-temperature structure, a feature that is ubiquitous in solid-solid transitions, but also of the fact that the high-temperature symmetry is a subgroup of the low-temperature symmetry, as it occurs for pristine fullerite. In fact, the positions of the diffraction peaks do not vary abruptly upon heating, rather, some peaks remain while other disappear, as also observed in pristine C_{60} across the (purely orientational) solid-solid phase transitions.[7] The remaining reflections at high temperatures, except perhaps for a few ones at low diffraction angles, correspond to the diffraction pattern of potassium sulfate[19] (K_2SO_4)[a] that exists in oxC_{60} as an impurity formed during the oxidation procedure (both H_2SO_4 and $KClO_3$ were employed in the initial steps of the synthesis, see Section 6.2). Thus, inside the material there are actually two different chemical species: oxC_{60} and potassium sulfate. The latter is present in a significant amount, large enough to be observed in XRD.

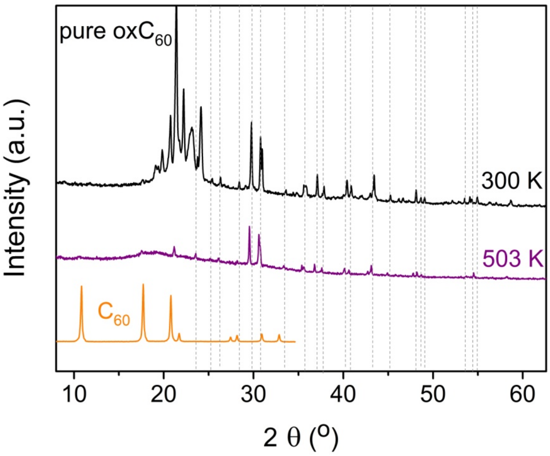

Figure 6.6 X-ray diffraction patterns of pure oxC_{60} at two indicated temperatures. For comparison, also the room temperature XRD pattern of fullerite (orange line) is shown. Vertical dotted lines correspond to the reflections of the solid potassium sulfate (K_2SO_4), taken from reference19.

Having identified the XRD features of the impurities, we will deal solely with the reflections of oxC_{60}. The observation of several diffraction peaks at room temperature indicates that the side-group-mediated

---

[a] From the oxidation processes that occur during the synthesis of the ox impurities C_{60}, secondary products can occur as impurities. *Potassium sulfate* is one of the remaining, actually the product of the reaction between potassium chlorate and sulfuric acid:

$$2\ KClO_3 + H_2SO_4 \rightarrow 2\ HClO_3 + K_2SO_4$$

interactions between the oxC_{60} molecules result in the formation of an ordered hydrogen-bond network at low temperature.

Due to the globular shape of C_{60}, the equilibrium structure of fullerite is basically determined by hard-sphere packing, and the same is basically true for solvate crystallites obtained with low-molecular weight solvents.[20] For oxC_{60} the situation differs from that of pristine fullerite due to the (directional) hydrogen-bond interactions that emerge due to the simultaneous presence of hydroxyl and epoxy functional moieties. While the presence of functional moieties leads to stronger interactions between the functionalized oxC_{60} molecules, at the same time it represents a steric barrier against denser packing, resulting in a lattice spacing of the same order of those found for several C_{60} solvates. Also, as visible in Figure 6.7 (a) the central portion of the diffraction pattern of oxC_{60} at room temperature exhibits the clear fingerprint of closely-spaced Bragg peaks as found in some solvates.[18]

Figure 6.7 (b) shows the comparison between the room-temperature XRD profile of oxC_{60} with those recorded at higher temperatures, chosen to be representative of the phase changes observed by DSC (see the previous section and Figure 6.4). It may be gathered that no new peaks arise in the high-temperature phases. Moreover, oxC_{60}-related reflections are completely absent at high temperature, especially in the region between 18° and 24°.

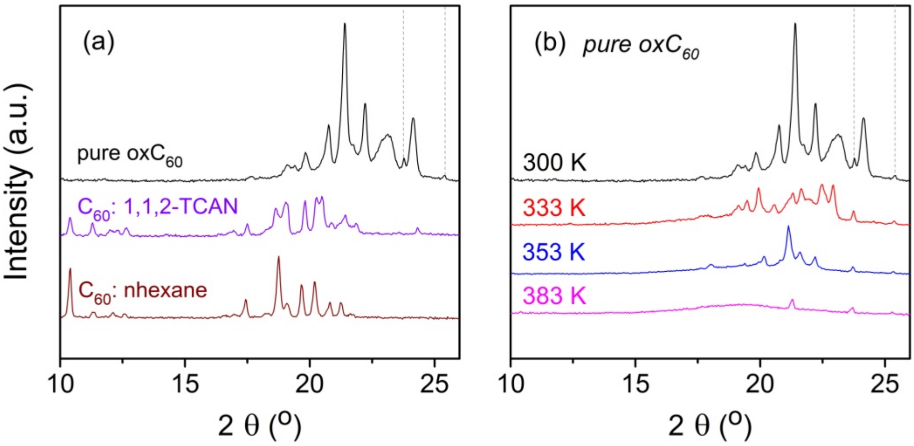

Figure 6.7 (a) X-ray diffraction pattern of pure oxC_{60} at room temperature for a 2θ range between 10° and 26°. For comparison, also the room temperature XRD pattern of the C_{60}·1,1,2-trichloroethane (TCAN)[18] and C_{60}·n-hexane (after reference 20) solvates are shown. (b) X-ray diffraction patterns of pure oxC_{60} at selected temperatures for the same 2θ range as in panel (a). Vertical dashed lines indicate the reflections of potassium sulfate (K_2SO_4), taken from reference 19.

Although we were not able to carry out a refinement of the oxC_{60} pattern, the fact that the number of peaks diminishes upon heating without the appearance of new ones means that the symmetry of the high-temperature phases includes the symmetry elements of the room-temperature one, or, in other words, that the high temperature phases differ from the room temperature one because an additional kind of disorder emerges. The change of the diffraction pattern with temperature is reminiscent of the temperature dependence of the diffraction profile in pristine fullerite, where some diffraction peaks become forbidden in the transition from the sc to the fcc phases and thus are absent from the high-temperature diffraction profile.[5] This similarity and the low number of diffraction peaks in oxC_{60} in the spectrum at 383 K suggests that the high temperature phase of oxC$_{60}$ is characterized by dynamic rotational disorder as pristine C$_{60}$.[5,7] The fact that in DSC there are two main (reversible) phase transitions (the intermediate minor peak is absent in some samples) indicates that the rotational melting in oxC$_{60}$ occurs in two steps, with the room temperature phase being fully ordered, the high-temperature one displaying full orientational disorder, and the intermediate phase (320 - 368 K) displaying only partial orientational disorder. Such double-step orientational transition in a narrow temperature range is likely related to the more varied decoration of the C$_{60}$ molecule with epoxy and hydroxyl moieties.

As we have concluded based on our calorimetry results, the transition at 320 K is associated with the breaking of the hydrogen bonds, which are totally absent after heating the sample to 503 K. Figure 6.8 presents the room-temperature XRD patterns of both the pristine oxC$_{60}$ sample and of a sample annealed to 503 K. The loss of the OH groups covalently attached onto C$_{60}$ spheres apparently induces a more symmetric structure, as visible from the lower number of peaks.

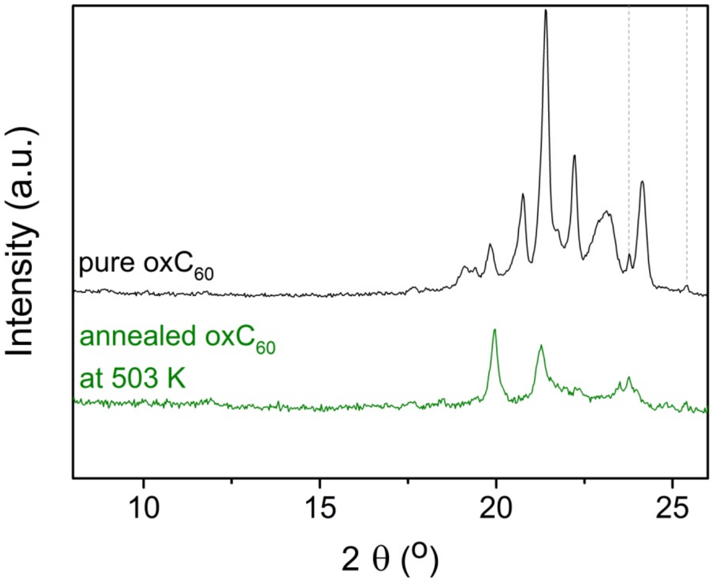

Figure 6.8 X-ray diffraction patterns of the pristine oxC_{60} sample and of a sample annealed at 503 K, recorded at ambient temperature in the 2θ range between 8° and 26°. The dotted lines in both panels correspond to the reflections of the solid potassium sulfate (K_2SO_4), taken from reference 19.

6.6 Dielectric signature of the orientational phase transitions in oxC_{60}.

In this section we focus on the dielectric behavior of pure (water-free) oxC_{60}, as obtained by heating to ~370 K to get rid of the water moieties. As argued in the preceding sections, after water desorption the material´s integrity is preserved and that pure oxC_{60} exhibits interesting phase behavior. The most striking characteristic of the pure material is the existence of an orientational order-disorder transition occurring in two steps, and involving the breaking of hydrogen bonds between the oxygen-decorated buckyballs.

We performed dielectric spectroscopy measurements on pure oxC_{60} in order to further study the orientational phase changes. Unfortunately, due to the symmetric shape of the fullerene cage and the presumably roughly symmetrical distribution of polar groups in oxC_{60}, we did not detect any orientational relaxation. However, as shown here, the phase changes can be detected in the dc conductivity as well as in the space-charge relaxations. Upon heating up a pure oxC_{60} pellet from room temperature to 408 K, we observed a single loss peak, which shifted to higher frequencies with increasing temperature, and a low-frequency conductivity background (Figure 6.9 (a)). The loss feature displayed a broad and symmetric shape, which above 315 K could be modeled with a Cole-Cole function with exponent $0.67 < \alpha_{CC} < 0.82$ whose value was only slightly temperature-dependent. Instead, below 315 K the peak appeared weaker, broader and more asymmetric, and was accordingly fitted with a Havriliak-Negami function. This prominent change of the dielectric feature at ~317 K was accompanied by a clear change in the conductivity background, both of which are readily seen in Figure 6.9 (a) as well as in Figure 6.9 (b), where the ac conductivity spectra are shown. In the latter, the low-frequency plateau corresponds to the long-range charge transport (dc conductivity) and the dispersive region is associated with charge percolation in restricted ranges (ac conductivity).[21] The changes at ~317 K in both loss and ac conductivity spectra correspond to the first (and most prominent) phase change observed in DSC and XRD measurements (occurring at approximately 317 K, see sections 6.4 and 6.5).

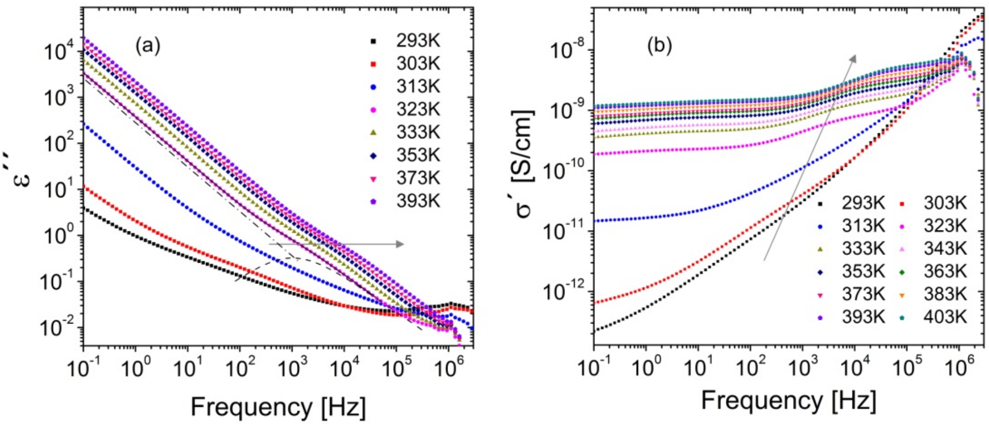

Figure 6.9 (a) Dielectric loss spectra of pure oxC$_{60}$, at selected temperatures upon heating from 293 to 393 K. The solid line through the spectrum at 323 K represents the fit with a single Cole-Cole loss peak (dashed line) on top of a conductivity background (dashed-dotted line). (b) Logarithmic plot of ac conductivity (σ´) of the same sample, upon heating from 293 to 403 K every 10 K. The grey arrows in both panels show the shift of the loss peak from low to high temperatures.

Figure 6.10 shows the Arrhenius plot of the characteristic relaxation time and dielectric strength of the loss feature visible in Figure 6.9. Clear and significant variations are observed across the transition at 320 K (1000/T ≈ 3.12 K^{-1}). The characteristic relaxation time decreases by more than two decades, while the dielectric strength shows non-monotonic behavior with a maximum close to the transition temperature, and similar values before and after the phase change.

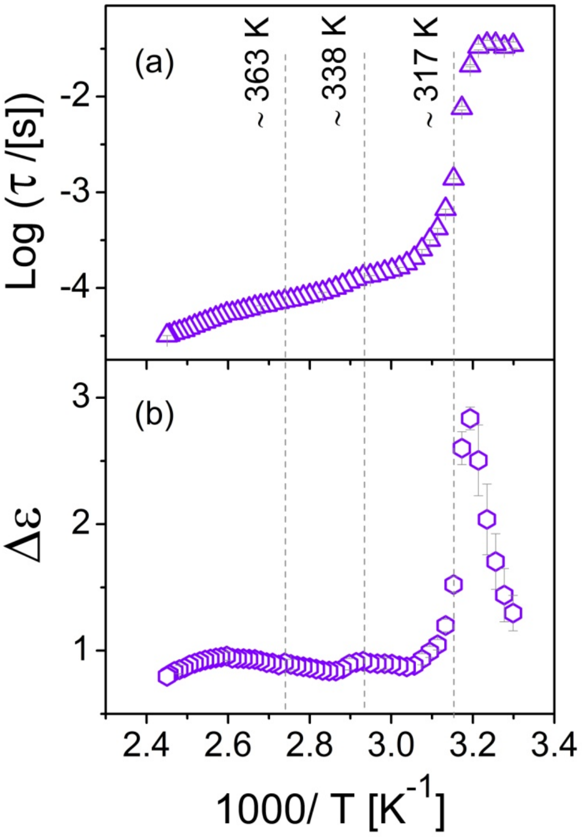

Figure 6.10 Relaxation time (a) and dielectric strength Δε (b) of the loss feature in pure oxC$_{60}$, as a function of the inverse temperature between 293 and 408 K. In both panels the vertical dashed lines indicate the temperatures of the phase transformations observed by DSC.

At ~338 K, there is a small change, which corresponds to the minor endothermic peak seen in the calorimetry thermogram (see Figure 6.4). Another minor discontinuity in the dielectric strength is observed around 363 K, which can be assigned to the last DSC transition. Finally, the dielectric strength above 363 K is seen to vary non-monotononically with temperature, displaying a maximum at ~383 K, in correspondence with a “kink” in the Arrhenius plot of the relaxation time. The origin of this last change at 383 K is not known.

We have extracted the dc conductivity (σ_{dc}) values from the low-frequency plateau of the ac conductivity spectra (see chapter 3) and we have plotted them against the inverse temperature in Figure 6.11 (b). It may be observed that the σ_{dc} value increases almost monotonically with increasing temperature, except around 363 K where a discontinuous variation (decrease) is observed in the temperature dependence of σ_{dc}. Such change coincides with the transition at ~370 K. The corresponding ac spectra are shown in Figure 6.11 (a). The phase transitions at 320 and 338 K are visible instead as smooth cross-overs between different temperature dependences (slopes of the Arrhenius plot) of σ_{dc}. Hence we conclude that almost all the observable changes in the loss and ac conductivity spectra are correlated with the phase transitions in the material. The (perhaps surprising) decrease of σ_{dc} around 370 K can be rationalized if one considers that this temperature marks the final step of the rotational melting of the oxC_{60} molecules. In fact, the electronic conduction properties of pure fullerite are known to be strongly influenced by the orientational dynamics: the hopping between the molecules is enhanced when the molecules are orientational ordered, leading to a step-like variation by two orders of magnitude of the dc conductivity upon crossing the transition at ~260 K.[22,23] A similar scenario is likely responsible for the decrease of the conductivity at the temperature of full rotational melting in oxC_{60}.

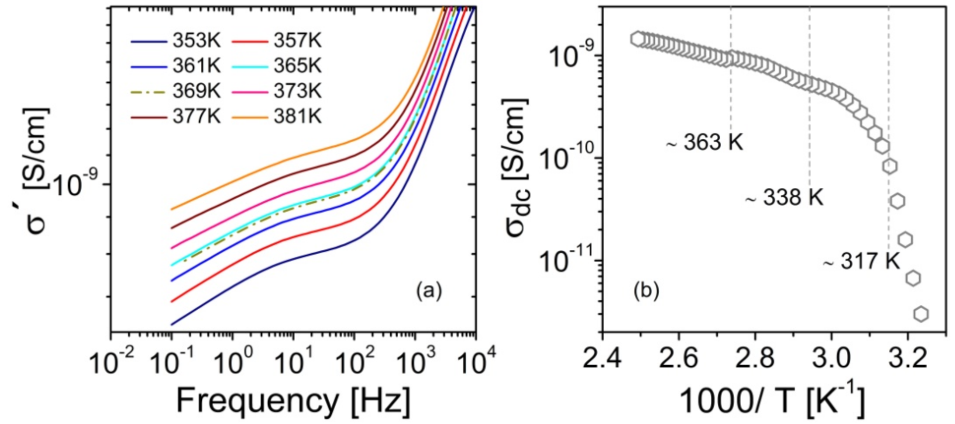

Figure 6.11 (a) Logarithmic plot of ac conductivity (σ′) at various temperatures in the range from 353 to 381 K every 2 K, upon heating. The value of the conductivity plateau increases with temperature up to 365 K, then decreases in two consecutive spectra (367 and 369 K) to resume increasing at higher temperature. (b) Arrhenius plot of the dc conductivity (σ_{dc}) extracted from the data of Figure 6.9 (b). The marked temperatures correspond to the phase transitions.

Figure 6.12 (a) displays the temperature dependence of σ_{dc} and of the frequency f_{max} of the maximum loss ($f_{max} = 1/2\pi\tau$). The data are displayed in a single Arrhenius plot with the same number of decades on both vertical axes. It may be observed that the variation with temperature of both quantities is virtually identical up to 367 K (roughly the temperature of the last phase transition). The common temperature dependence indicates that the loss feature has a conductivity origin.[24] We argue in what follows that, at least up to 367 K, the loss is a space-charge relaxation.

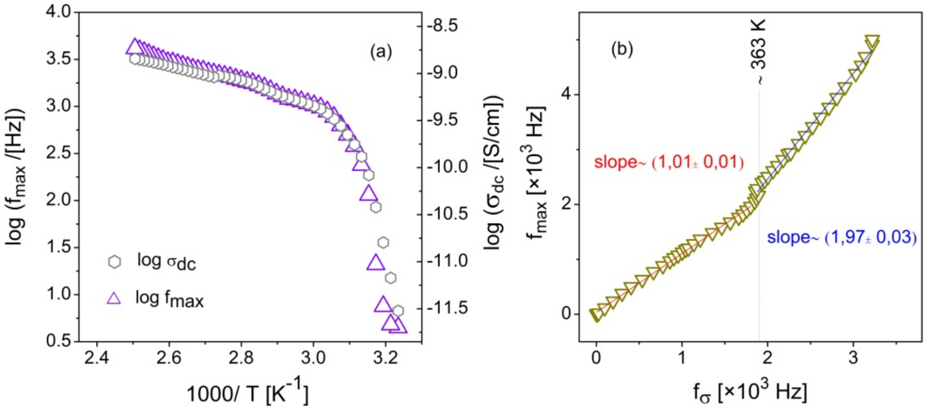

Figure 6.12 (a) Arrhenius plot of the characteristic frequency (f_{max}) of the relaxation process, compared with that of the dc conductivity (σ_{dc}), in the temperature range between 309 and 400 K upon heating. (b) Plot of f_{max} versus the space-charge relaxation frequency f_σ (characteristic frequency of spatial charge fluctuations, see the text), in the same temperature interval as in (a).

A space-charge loss feature must satisfy the Barton-Nakajima-Namikawa (BNN) condition,[25] according to which $\sigma_{dc} = p\ 2\pi\varepsilon_0\Delta\varepsilon\ f_{max}$, where p is a constant of the order unity, ε_0 is the vacuum permittivity, and $\Delta\varepsilon$ is the dielectric strength of the loss feature (see chapter 2). Based on the BNN condition, one can introduce a so-called space-charge relaxation frequency, f_σ, defined as $\mathbf{f}_\sigma = \sigma_{dc}/2\pi\varepsilon_0\Delta\varepsilon$. The parameter f_σ represents the characteristic frequency for spatial charge fluctuations in a conducting medium,[26] in other words, it is the frequency corresponding to the typical percolation length for restricted hopping, which marks the onset of the ac regime of the conductivity. As visible in Figure 6.12 (b), a linear dependence is found between the experimental maximum loss frequency f_{max} and the BNN space-charge relaxation frequency f_σ. The slope of the linear plot of one frequency versus the other is unity (1.01±0.01) below ~367 K, implying that $f_{max} \approx f_\sigma$ (Figure 6.12 (b)), confirming the space-charge nature of the dielectric loss. The proportionality between f_σ and σ_{dc} shows that the microscopic mechanism responsible for space-charge fluctuations is exactly the same as the one involved in the long-range conductivity. On the other hand, the divergence of the Arrhenius plots of f_{max} and σ_{dc} (Figure 6.12 (a)) and the change in the slope of f_{max} versus f_σ (Figure 6.12 (b)) above 367 K, both indicate that the loss feature acquires a different character at higher temperature, possibly related to the rotational motions of the oxC_{60} molecules in the high-temperature phase. In the log-log plot of f_{max} versus f_σ (not shown), the data below 367 K have a linear slope of approximately unity, while the higher-temperature data have a slope close to 1.4, which shows that in the high-T phase the two quantities are correlated but not linearly proportional to one another, confirming the non-pure space-charge character of the relaxation at high temperature.

The space-charge relaxation is due to accumulation of electronic charges due to the spatial heterogeneities in the conductivity of the medium (such as grain boundaries).[24] The changes observed in the space-charge loss in oxC_{60} around 320 and 370 K may then be rationalized in terms of allowed molecular motions, since these may influence the hopping of charges. At low temperature, the electrical conductivity is quite low, and so is the significance of space-charge effects. Around 320 K the first rotational phase transition is accompanied by a significant increase in the dc conductivity, which also enhances the visibility of the conductivity-related loss. The final orientational melting transition around 370 K lowers the dc conductivity and results in a higher rotational lability of the oxC_{60} molecules with the possibility of reorientation of the molecular dipole moment following the spatial fluctuation of the free charges, leading perhaps to a partially dipolar character of the dielectric loss feature.[27]

We have found in our calorimetric study (see section 6.4) that, upon heating to 500 K, several oxygen-containing groups of the oxC_{60} molecules detach from the carbon cage, resulting in the inability to form hydrogen bonds. This was visible by the vanishing intensity of the DSC transition at 320 K in samples heated to 500 K. We have performed dielectric measurements on a sample pre-annealed to 503 K in order to study the conduction and relaxation properties after the loss of the (major part of) the functional groups. Figure 6.13 (a) displays the dielectric spectra acquired in the temperature range 293 - 408 K (every 10 K). A prominent electrode polarization effect is observed, which masks the presence of a very weak loss at higher frequencies. To better visualize the loss feature, in the inset to Figure 6.13 (a) we employed a derivative-based analysis.[28] The Arrhenius plot of the relaxation time extracted from the fitting of the spectra of panel (a) is shown in Figure 6.13 (b). A cross-over is visible in the temperature-dependence of τ, roughly in correspondence with the highest-temperature phase transition (~370 K, see vertical dotted line). For comparison, we have added the relaxation times of pristine oxC_{60} (Figure 6.10 (b)).

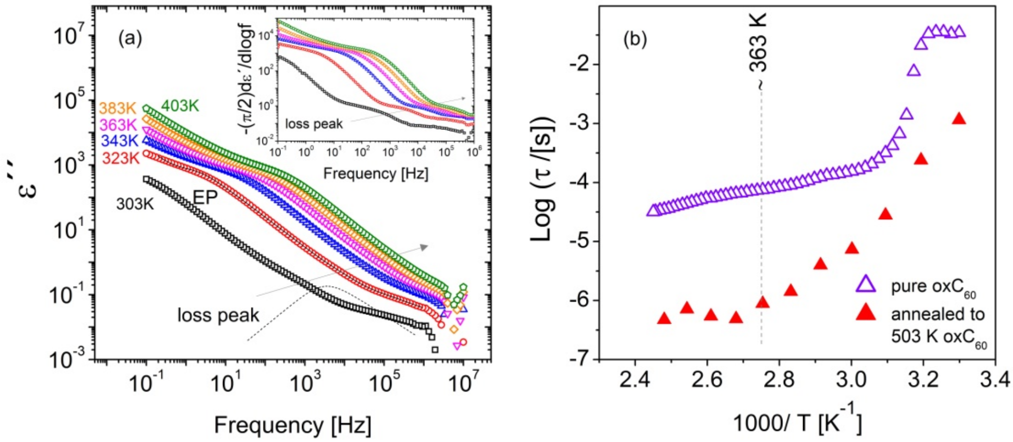

Figure 6.13 (a) Loss spectra of an oxC$_{60}$ sample pre-annealed to 503 K, upon heating from 303 to 403 K (spectra every 20 K are shown). The solid line through the spectrum at 323 K represents a fit of the loss spectrum with a Havriliak-Negami function (dotted line) on top of a conductivity background. The spectral bending at low frequency is due to the electrode polarization effect. Inset: Derivative of the real part of the complex permittivity of the spectra shown in panel (a), to better visualize the shift of the loss peak (marked by an arrow). (b) Relaxation times τ of the sample in (a) (filled triangles) as a function of the inverse temperature between 293 and 408 K. The relaxation time for pristine oxC$_{60}$ (empty triangles) is added for comparison.

In order to study the change in the conduction properties of oxC$_{60}$ after the loss of the oxygen-containing groups, we have analyzed the temperature dependence of the dc-conductivity of the annealed sample at 503 K in the temperature range between 293 and 408 K upon heating. The σ_{dc} values were obtained from the plateau at intermediate frequeny visible in the spectra above 308 K (Figure 6.14 (a)) Due to the prominent electrode polarization effect (bending) at low frequencies, the σ_{dc} value is extracted with the help of the first derivative: the minimum of the first derivative ($\frac{d\sigma'}{df}$) is used to define the frequency f_0 where the value of σ_{dc} should be determined as $\sigma_{dc} = \sigma'(f_0)$ (see chapter 2). The dc conductivity of the sample pre-annealed to 503 K undergoes few changes in the whole temperature interval as Figure 6.14 (b) displays. In the figure we have also added the temperature behavior of σ_{dc} of a pure oxC$_{60}$ upon heating in the same temperature range (293 - 403 K) for comparison.

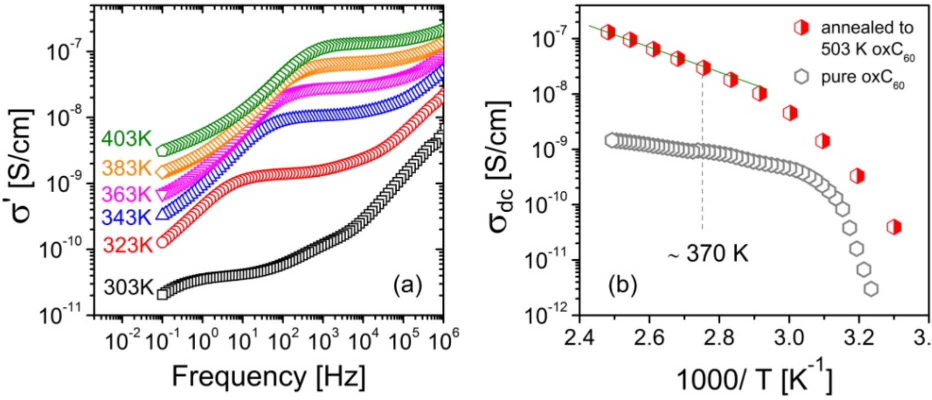

Figure 6.14 (a) Logarithmic ac conductivity spectra (σ′) measured upon heating on a sample pre-annealed to 503 K (same data set as Figure 6.13). The low-frequency 'bending' in the spectra is due to electrode polarization effect (also visible in the corresponding loss spectra of figure 6.13 (a)). (b) Arrhenius plot of the dc conductivity (σ_{dc}) extracted from the data of panel (a). The value of σ_{dc} for pristine oxC$_{60}$ (empty markers) is added for comparison. The marked temperature correspond to the highest-temperature phase transition according to DSC measurements, and the solid line was added to highlight the change of slope In the data.

Electrical conduction is enhanced after the partial decomposition, possibly due to the formation of a material closer to pure C$_{60}$, which is known to exhibit a relatively high electronic conductivity (while the oxygen functionalization in oxC_{60} probably leads to trapping of charge carriers).[22] However, the most important observation is the almost negligible change of τ and σ_{dc} at 320 K, in agreement with the lack of a low-temperature transition in our calorimetric results on this material. The only transition visible in the dielectric data is a change of slope in the Arrhenius plot of the relaxation time and of the dc conductivity (see Figures 6.13 (b) and 6.14 (b), respectively), which appears to be associated with the highest-temperature phase transition. These findings corroborate the fact that the high-temperature rotational melting is maintained in the material obtained by annealing at 500 K.

6.8 Conclusions

A combination of characterization techniques was applied to investigate the orientational phase transitions in a newly-synthesized C_{60} derivative, oxofullerenol (oxC_{60}), of chemical formula $C_{60}(OH)_{14}O_n$ with n between 4 and 8. The presence of oxygen-containing functional groups (hydroxyl, carbonyl, and epoxy oxygens) covalently bonded onto the surface of the buckyballs leads to hygroscopic behavior, and most importantly, to the formation of a hydrogen-bond network between the oxC_{60} moieties. X-ray diffraction reveals the presence of a minority inorganic salt (K_2SO_4) in the sample.

Upon water desorption, the oxC_{60} molecules not only maintain their integrity, but actually display intriguing orientational phase transitions reminiscent of the phase behavior of other fullerene solids. The orientational phase transitions were demonstrated by calorimetry, X-ray diffraction, and dielectric measurements. A hydrogen-bonded network appears to be present in the room-temperature stable phase, which leads to an ordered, lower-symmetry structure without molecular motions. The rotational melting of the oxC_{60} moieties takes place in at least two steps (at 320 and 370 K), with an intermediate partially ordered phase separating the ordered room-temperature phase and the disordered high-temperature phase. The latter seems to be characterized by dynamical reorientational motions.

The dc conductivity of oxC_{60}, as measured by dielectric spectroscopy, displays changes across all rotational phase transitions. A space-charge relaxation is detected, due to charge accumulation at the sample heterogeneities (grain boundaries), which fulfills the Barton-Nakajima-Namikawa relation. An anomaly in the space-charge relaxation is observed at 370 K, the temperature that marks the full rotational melting, where the dc conductivity is observed to decrease as in the analogous transition at 260 K in pristine fullerite (C_{60}).

Bibliography

[1] E. Mitsari, M. Romanini, M. Zachariah, R. Macovez *Curr. Org. Chem.,* vol. 20, p. 645, 2016.

[2] R. Tycko, G. Dabbagh, R.M. Fleming, R.C. Haddon, A.V. Makhija, S.M. Zahurak *Phys. Rev. Lett.*, vol. 67, p. 1886, 1991.

[3] D.I.F. William, R.M. Ibberson, J.C. Matthewman, K. Prassides, T.J.S. Dennis, J.P. Hare, H.W. Kroto, R. Taylor *D.R.M. WAalton Nature* vol. 353, p.147, 1991.

[4] F. Gugenberger, R. Heid, C. Meigast, Adelmann, M. Braun, H. Wuhl. *Phys. Rev. Lett.,* vol. 69, 3774, 1992.

[5] P.A. Heiney, J.E. Fischer, A.R. McGhie, W.J. Romanow *Phys. Rev. Lett.,* vol. 66, p. 2911,1991.

[6] C. Meingast, G. Roth, L. Pintschovius, R.H. Michel, C. Stoermer, M.M. Kappes, P.A. Heiney, L. Brard, R.M. Strongin, A.B. Smith *III Phys. Rev. B.,* vol. 54, p. 124, 1996.

[7] A.N. Lommen, P.A. Heiney, G.B.M. Vaughan, P.W. Stephens, D. Liu, D. Li, A.L. Smith, A.R. McGhie, R.M. Strongin, L. Brard, A.B. Smith *III Phys. Rev. B.,* vol. 49, p.12572, 1994.

[8] L. Staudenmaier *Berichte der deutschen chemischen Gesellschaft.*, vol. 31 p. 1481, 1898.

[9] R.Y.N. Gengler, A. Veligura, A. Enotiadis, E.K. Diamanti, D. Gournis, C. Jozsa, *Large-Yield Preparation of High-Electronic-Quatity Graphene* by a Langmuir-Schaefer Approach. Small vol. 6, p. 35, 2010.

[10] P. Zygouri, K. Spyrou, E. Mitsari, M. del Barrio, R. Macovez, D. Gournis, P. Rudolf (submitted)

[11] R. Rivelino, T. Malaspina, E.E. Fileti *Phys. Rev. A.*, vol. 79, 013201, 2009.

[12] E. Pretsch, P. Bühlmann, C. Affolter, A. Herrera, R. Martínez *Structural determination of organic compounds.* Barcelona: Masson, 2002.

[13] G. Bogdanovic, V. Kojic, A. Dordevic, J. Canadanovic-Brunet, M. Vojinovic-Miloradov, V. Vit. Baltic *Toxicology in Vitro*, vol. 18, p. 629,

[14] H. He, L. Zheng, P. Jin, M. Yang *Computational and Theoretical Chemistry* (Comptc)., vol. 974, p. 16, 2011.

[15] B. Vileno, P.R. Marcoux, M. Lekka, A. Sienkiewicz, T. Fehér, L. Forró *Adv. Funct. Mater.*, *vol.* 16, p. 120, 2006.

[16] R. Macovez, E. Mitsari, M. Zachariah, M. Romanini, P. Zygouri, D. Gournis, J.L.Tamarit, *J. Phys. Chem. C.*, vol. 118, p. 4941, 2014.

[17] M. Zachariah, E. Mitsari, M. Romanini, P. Zygouri, D. Gournis, M. del Barrio, J.L.Tamarit, R. Macovez *J. Phys. Chem. C.*, vol. 119, p. 685, 2015.

[18] F. Michaud, M. del Barrio, D.O. Lopez, J.L. Tamarit, V. Agafonov, S. Toscani, H. Szwarc, R. Céolin *Chem. Mater.* vol. 12, p. 3595, 2000.

[19] S. Bin Anooz, R. Bertram, D. Klimm. *The solid state phase transformation of potassium sulfate.* Solid State Communications., vol. 141, p. 497, 2007.

[20] S. Toscani, H. Allouchi, J.L. Tamarit, D.O. López, M. del Barrio, V.; Rassat, A. Agafonov, H. Szwarc, R. Céolin, *Chem. Phys. Lett.,* vol. 330, p.491, 2000.

[21] A.K. Jonscher *Nature* vol. 267, p. 673, 1977.

[22] R. Macovez, P.Rudolf, “Electronic structure of fullerene-based materials”, in *Encyclopedia of Materials: Science and Technology, 2006 Online Update*, Ed.s: Jürgen Buschow, Merton Flemings, Robert Cahn, Patrick Veyssière, Edward Kramer, Subhash Mahajan, Elsevier Ltd, Amsterdam, The Netherlands, 2006.

[23] E.A. Katz, D. Faiman, K. Iakoubovskii, A. Isakina, K.A. Yagotintsev, M.A. Strzhemechny, I. Balberg, *J. Appl. Phys.,* vol. 93, p. 3401, 2003.

[24] J. C. Dyre, T.B. Schroder *Rev. Mod. Phys.,* vol. 72, p. 873, 2000.

[25] H. Namikawa, *J. Non-Cryst. Solids.,* vol. 18, p. 173, 1975.

[26] D.L. Sidebottom *Phys. Rev. Lett.,* vol. 82, p. 3653, 1999.

[27] R. Macovez, M. Zachariah, M. Romanini, P. Zygouri, D. Gournis, J.L. Tamarit *J. Phys. Chem. C.,* vol. 118, p. 12170, 2014.

[28] M. Wubbenhorst, J. van Turnhout *J. Non-Cryst. Solids.,* vol. 305, p. 40, 2002.

Chapter 7

C_{60} SOLVATE WITH (1,1,2) -TRICHLOROETHANE: DYNAMIC STATISTICAL DISORDER AND MIXED CONFORMATION

7.1 Introduction

Molecular solids can display complete translational and rotational order (*crystal*) or complete rototranslational disorder (*liquid*). In between these two extremes, molecular solids display phases with only partial order, as is the case of *orientationally disordered solids (OD)*. In OD phases, a prominent example of which are plastic crystals[1], the molecules' average centers of mass occupy lattice positions while their orientations are disordered as in a liquid. These phases can be formed by small molecules such as methane[2,3,4] or ethane derivatives,[5,6,7,8] or by globular-shaped molecules such as adamantanes[9,10] or fullerenes.[11,12] Research on OD phases has lead to important, in some instances unexpected, discoveries: for example, studies on orientationally disordered fullerene (C_{60}) films have highlighted that orientational melting and solid-solid transitions are fundamentally modified at the surface of an OD phase.[13,14] Studies on solvents that display below their melting point either a supercooled liquid phase or an OD solid phase depending on the thermal treatment showed quite surprisingly that the glass transition is governed to a large extent by the freezing of the orientational degrees of freedom rather than translational ones.[1,15,16,17,18]

Fullerite (solid C_{60}) is a particularly simple and interesting example of a material displaying an OD phase. At room temperature, fullerite displays a so-called crystalline "rotator" phase in which the molecules spin as free rotors. Below 260 K the free-rotor spinning is reduced to a merohedral ratcheting motion between two preferred orientations[11,12] that freezes out at the glass transition temperature of 90 K.[19,20] OD phases with free-rotor or merohedral disorder have been identified also in many C_{60} intercalation compounds, such as inorganic co-crystals like alkali fullerides,[14,21] or molecular co-crystals of C_{60} with organic intercalants.[22,23,24,25] Binary C_{60} co-crystals are relatively simple systems to study the effects on rotational degrees of freedom of heteromolecular interactions (specifically, between C_{60} and the organic intercalants). While several studies have shown the unhindered rotational motion of C_{60} (even when it is intercalated with guest molecules),[23,26,27] very few studies have focused on the dynamics of the intercalant molecules, most of which limited to establishing the existence of dynamic disorder of the intercalants.[24,26,28,29,30] Probing the dynamics of both host and guest molecules can shed light on possible correlations between the dynamics of different species, and thus help understand from an experimental perspective the dynamic interactions (steric, van der Waals, dipolar, etc.) taking place between different molecules. Such knowledge may have a direct relevance for organic and biological systems, where the different present chemical species generally display correlated dynamics.[31,32,33]

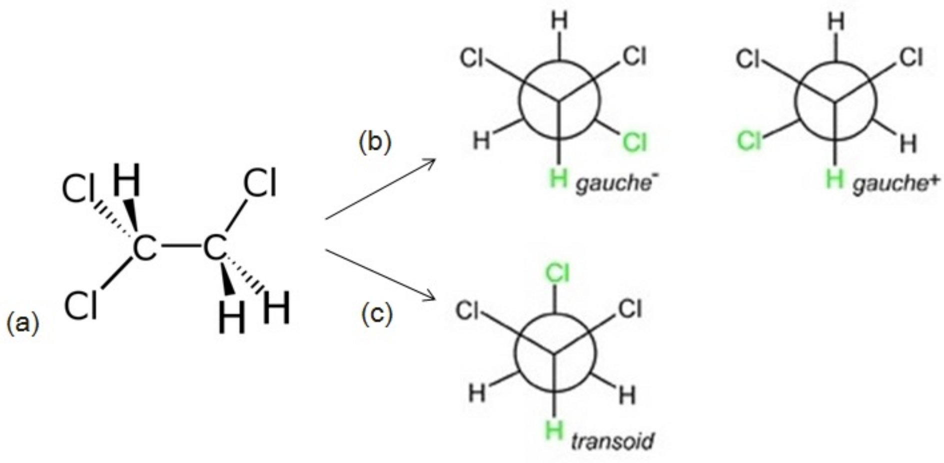

Figure 7.1 Molecular structure of (1,1,2)-trichloroethane molecule (a) and its both conformers, gauche (b) and transoid (c).

In this chapter we study the binary system consisting of the dipolar solvent (1,1,2)-trichloroethane ($C_2H_3Cl_3$) (Figure 7.1) and the nonpolar Buckminster fullerene molecule (C_{60}). This binary system is particularly interesting because both C_{60} and $C_2H_3Cl_3$ display disordered solid phases,[11,12,19,20,34] and together they form a stable solvate.[35] Moreover, (1,1,2)-trichloroethane is known to exist in two conformations[34]: the gauche (gauche$^+$/ gauche$^-$) conformer is less polar and more stable and the transoid one, which is more polar. Both conformers can be visualized in Figure 7.1 (b) and (c), respectively. These two different conformations of the ethane derivative ($C_2H_3Cl_3$) are expected to contribute to the dynamical behavior of the solvate due to their polarity.

7.2 Experimental Methods

Buckminsterfullerene C_{60} and (1,1,2)-trichloroethane ($C_2H_3Cl_3$) were purchased from Aldrich with purities 99.5 % and 99 %, respectively. The $C_2H_3Cl_3$ solvent was distilled twice at 385 K before use. The formation of the C_{60}:$C_2H_3Cl_3$ solvate was already reported in reference 35, in a study which also specified the symmetry of the solvate structure and the stability inside the mother liquor for prolonged periods of time. Briefly, dissolutions of C_{60} in $C_2H_3Cl_3$ were allowed to evaporate in the dark at room temperature, yielding a powder composed of plate-like and needle-shaped crystals. The sample was probed by thermogravimetry, calorimetry, powder X-ray diffraction, Raman spectroscopy and broadband dielectric spectroscopy. Grinding and application of hydraulic pressure to the samples were avoided due to the tendency of the solvate to decompose under mechanical treatment,[35] as observed also in other C_{60} solvates.[36]

Thermogravimetric characterization of the solvate powder (not shown) shows a mass loss of about 15% upon desolvation, which is consistent with the 1:1 stoichiometry of the solvate. The phase behavior of the synthesized powder, as measured by calorimetry, was similar to that reported in ref. 35. Thermal analyses carried out on the solvate polycrystalline powder indicate a desolvation temperature of 420 K, slightly lower than that of the single crystal solvate (440 K).[35]

High-resolution X-ray powder diffraction (XRPD) profiles were recorded over a 2θ range between 4° and 40° with an angular step of 0.029° (2θ) at ambient temperature. The solvate powder was placed in a Lindemann capillary tube (0.5 mm diameter). Analysis of the diffraction data was carried out using the Fullprof software by comparing the experimental data, including the single crystal data published in ref. 35, with different microscopic models for the molecular arrangements.[a] The FullProf package offers the possibility to refine a single structure model on multiple data sets (such as a powder and a single-crystal data set) with relative weights. Instead, a structure analysis based exclusively on the single-crystal data (which include only 29 reflections) was not possible due to the large number of refined parameters.

For dielectric measurements, the solvate powder was pressed manually between two stainless steel disks to obtain a pellet inside the parallel plate capacitor formed by the metal disks. The thickness of the pellets was varying between 0.50 to 0.92 mm. The dielectric spectra were acquired in the frequency range from 10^{-2} to 10^{6} Hz with a Novocontrol Alpha analyzer. Temperature control was achieved by nitrogen-gas flow, which allowed measuring every 5 K in a temperature interval between 120 and 300 K with a temperature stability of 0.5 K. Raman Microscopy was employed to record spectra at room temperature in the wavenumber range between 50 cm^{-1} and 2500 cm^{-1} (at higher wavenumbers a fluorescence signal dominated the spectra). The Raman scattering spectra were measured with ten accumulations (with acquisition time of 30 s) and low laser power (0.05 mW) so as to avoid any photodecomposition. Pure C_{60} powder and liquid (1,1,2)-trichloroethane were also characterized for comparison. For the liquid only 5 accumulations were used each with acquisition time of 5 s, and the laser power was set to 5 mW. Raman characterization was carried out at the Scientific and Technological Center (ccit) at university of Barcelona.

---

[a] The rigid-body model analysis was carried out by Dr. Navid Qureshi of the Diffraction Group of Institut Laue-Langevin (Grenoble, France).

7.3 XRD Patterns and Structural Modeling

When co-crystallized with solvent or guest molecules, C_{60} forms a large variety of structures depending on the size of the solvent/guest molecules compared with that of the C_{60} species.[22] In the case of the C_{60}:$C_2H_3Cl_3$ solvate, a single-crystal study[35] reported orthorhombic lattice metrics but with monoclinic symmetry of space group $P2_1/n$. The monoclinic symmetry departs from the orthorhombic symmetry of similar C_{60} solvates with 1:1 stoichiometric ratios, such as the ones with *n*-pentane, *n*-hexane or dichloroethane.[37,38,39]

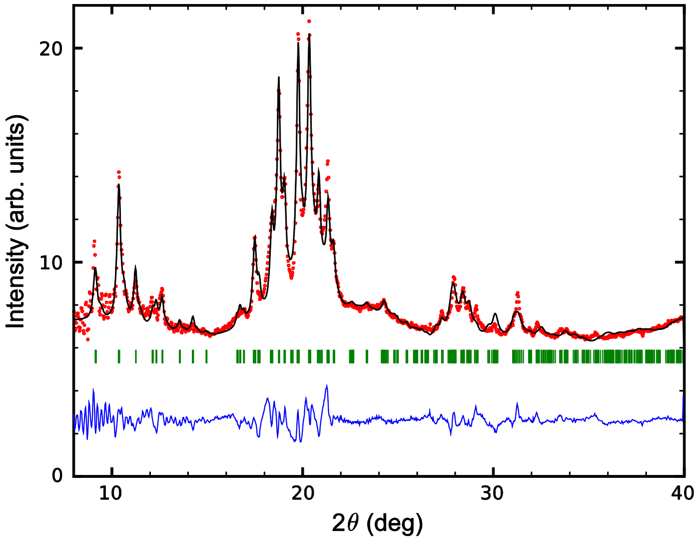

Figure 7.2 Experimental X-ray powder diffraction pattern of the C_{60}:$C_2H_3Cl_3$ solvate (red markers), together with the Rietveld fit (superposed solid line) and the respective difference (lower solid line). Vertical bars indicate the refined angular Bragg peaks.

The room-temperature powder XRD pattern of C_{60}:$C_2H_3Cl_3$ (Figure 7.2) is consistent with the monoclinic symmetry. A symmetry lower than orthorhombic could be due to an anisotropic orientational disorder of the ethane derivatives or results from the fact that the $C_2H_3Cl_3$ molecules do not possess a mirror plane symmetry. To explore this issue, we modeled both powder and single-crystal diffraction patterns using different assumptions on the conformation, position and orientation of each molecular species.

The powder diffraction pattern and the single-crystal intensities were analyzed using a rigid-body model for both the C_{60} and the $C_2H_3Cl_3$ molecules. The data was also analyzed using symmetry-adapted spherical harmonics in order to mimic a possible orientational disorder of the C_{60} molecules, yielding similar results. This suggests that the C_{60} molecules might display dynamic orientational disorder, as found in several solvates.[23,24,40] Refined parameters of the crystal structure were the lattice constants, the positions of the molecules, their orientation, the isotropic temperature factors and the occupation factors. The quite broad diffraction profiles could only be described by introducing positional and orientational disorder of the C_{60} moieties. The C_{60} positional disorder was simulated by considering two nonequivalent molecular positions in the unit cell, *p1* and *p2*, and fixing the sum of the respective occupation factors to unity.

The refinement of the powder data clearly reveals the positions of the C_{60} molecules and provides the lattice symmetry and parameters. The average lattice parameters deduced from the powder data are a = 10.1302(5) Å, b = 31.449(2) Å, c = 10.1749(5) Å, and β = 90.14(8)°. The matrix formed by the fullerene units can be described as the stacking, along the b crystallographic axis, of C_{60} layers parallel to the ac plane with a square-like base of side equal to the fullerene van-der-Waals diameter. This is visible in Figure 7.3, where the refined structure of the C_{60}:$C_2H_3Cl_3$ solvate is depicted. The stacking order of the square-like planes is of the type AB-B'A'-AB. In units of the unit cell parameters, B is shifted by (x+½, –y+½, z+½) with respect to A, and B' and A' are shifted by (–x+½, y+½, –z+½) with respect to A and B, respectively, where the fractional coordinates x, y and z refer to the position (*p1* or *p2*) of a C_{60} molecule within the A layer. The positions *p1* and *p2* of the centers of mass of the two nonequivalent fullerene molecules in the A layer are listed in Table 1. The positional disorder is mainly along the b axis, and leads to a significant overlap of *p1* and *p2* molecules in the unit cell. The positional disorder corresponds to a locally-varying separation (orthogonal distance) between the AB and B'A' bilayers. It is worth pointing out that two nonequivalent C_{60} positions were also reported in the fullerene solvate with benzene (C_{60}:$4C_6H_6$).[41] We argue that the existence of different (positional) C_{60} sites is related to a static (and not dynamic) translational disorder, associated with the relatively poor crystallinity of the powder.

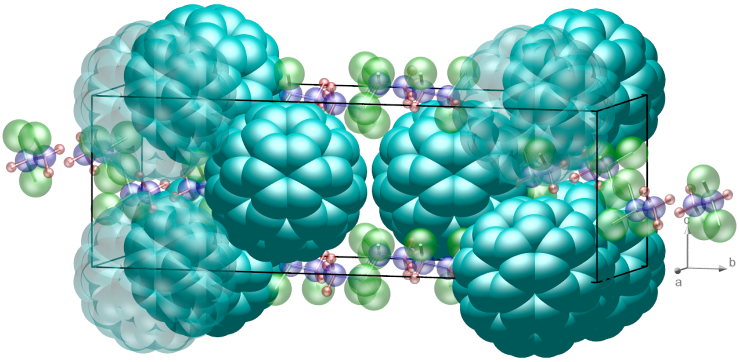

Figure 7.3 Visualization of the refined crystal structure of the C_{60}:$C_2H_3Cl_3$ solvate. The cuboid represents the monoclinic unit cell. For clarity, only the averaged centers of mass of the C_{60} molecules are shown, and some fullerenes are displayed with a transparency to better visualize the positions of the other molecules. Both *transoid* and *gauche* $C_2H_3Cl_3$ conformers are present, and for each conformer both refined positions are shown, to emphasize the filling of the interstitial cavities between the C_{60} molecules (two $C_2H_3Cl_3$ molecules occupy each cavity).

The excess electron density between the C_{60} species is attributed to the contribution of orientationally disordered $C_2H_3Cl_3$ molecules. The $C_2H_3Cl_3$ positions were refined by reproducing the extra diffraction intensity not accounted for by the contribution of the C_{60} species. As visible in Figure 7.3, relatively large interstitial cavities separate fullerene molecules along the direction parallel to the b axis. These interstitial sites are large enough to accommodate at least two ethane derivatives (instead, the $C_2H_3Cl_3$ molecules are too big to fit in the octahedral cavities of pristine fullerite), and due to the symmetry of the crystallographic space group and the obtained positions of the $C_2H_3Cl_3$ molecule, there are always two molecules within a cavity, connected by an inversion center.

Two distinct positions and orientations of either two transoid, two gauche or one of each conformer were refined, restricting the total occupation to one molecule per formula unit. From the powder data alone it was not possible to deduce the distribution of the different conformers, because also populations of 100% transoid or 100% gauche conformers yielded comparable results (R_F = 4.02%). However, a correlated refinement between the powder and the single crystal data strongly favors the scenario with two conformers, with a majority of gauche transformers (the agreement factors of the correlated refinement are $R_{F,p}$ = 8.95% and $R_{F,sc}$ = 22.1%, while the refinements using exclusively transoid or gauche diverged). The existence of both conformers is confirmed by the characterization by dielectric spectroscopy and Raman (see the next section).

The obtained positions of both the transoid and gauche conformers are listed in Table 1. As visible in Figure 7.3, the stacking of fullerene planes along the b direction is interrupted by interstitial $C_2H_3Cl_3$

molecules arranged in pairs; the translational disorder of the C_{60} molecules along the b axis is therefore related to the disordered arrangement of the (1,1,2)-trichloroethane molecules in the interstitial cavities. Inspection of the refined atomic positions indicates that the ethane derivatives display a tendency to orient themselves with a C–halogen bond rotated towards the closest C_{60} neighbor, as reported for example also in the case of the C_{60} solvates with bromobenzene (C_{60}:$2C_6H_5Br$) and with benzene and diiodomethane (C_{60}:CH_2I_2:C_6H_6).[42,43] Both the C_{60} and the $C_2H_3Cl_3$ molecules occupy a single general 4e Wyckoff site, which in particular means that all the $C_2H_3Cl_3$ molecules of the same conformation have the same crystallographic environment.

Table 1. Molecular center-of-mass positions obtained by correlated refinement between powder and single-crystal diffraction data. The positions of each molecule (two of each kind) are given in units of the lattice constants deduced from the powder data.

	C_{60} *p1*	C_{60} *p2*	$C_2H_3Cl_3$ *transoid*	$C_2H_3Cl_3$ *gauche*
x	0.218(4)	0.193(2)	0.90(3)	0.76(1)
y	0.169(2)	0.122(2)	0.67(1)	0.571(4)
z	0.004(3)	-0.0.03(2)	0.06(6)	0.09(1)
occupancy	0.46(2)	0.54(2)	0.25(1)	0.75(1)

7.4 Dielectric Relaxations and Raman Spectroscopy Results

Since $C_2H_3Cl_3$ has a permanent dipole moment whereas C_{60} does not, one may expects that the response of the solvate under an applied electric field will be possibly attributed to the dynamics of (1,1,2)-trichloroethane molecules. Figure 7.4 (a) shows the dielectric spectra of the solvate at a temperature range between 120 and 300 K. From visual inspection of e.g. the spectra at 180 and 195 K, two distinct relaxation features are present, with comparable dielectric strength (see Figure 7.4 (b)). These results are found to be reproducible measuring at multiple heating-cooling cycles and in different samples. Both dielectric features are due to dipolar moieties present in the solvate. Moreover, the observation of dynamic processes indicates that the disorder highlighted by the analysis of XRD data is actually dynamic in character, at least for what concerns the ethane derivatives.

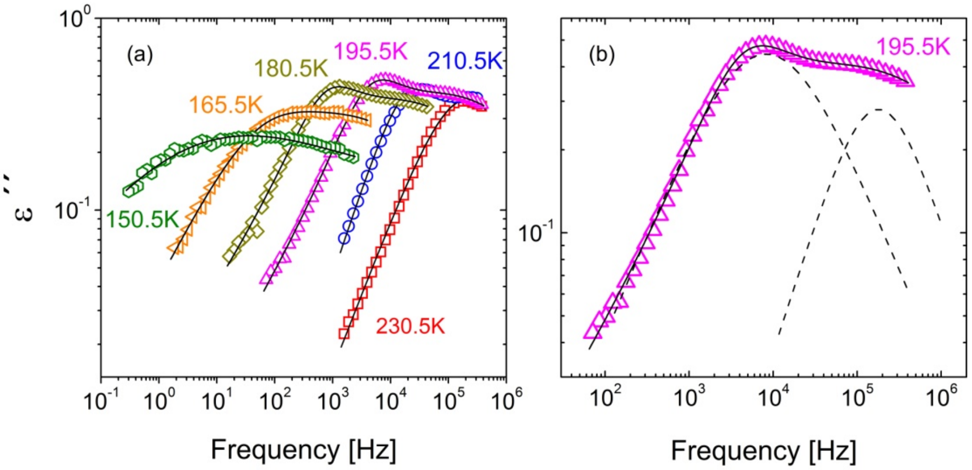

Figure 7.4 (a) Dielectric loss spectra of the C_{60}:$C_2H_2Cl_3$ solvate, at selected temperatures in the range from 120 to 300 K. Continuous lines are fits assuming a Cole-Cole profile of each loss feature (see the text). (b) Visualization of both components (dashed lines) in the fit of the spectrum acquired at 195.5 K.

As it can be seen in Figure 7.4 (a), starting from the lowest temperature one broad relaxation process appears, while upon further heating another one emerges in the experimental window. In order to carry out a quantitative analysis, both dielectric loss features were fitted by a Cole-Cole function with shape parameters $0.49 < \alpha_{CC} < 0.80$ for the lower frequency peak and $0.45 < \alpha_{CC} < 0.99$ for the high frequency peak. The lower frequency feature appears with a slightly higher dielectric strength than the other (see Fig. 7.4 (b)).

Figure 7.5 (a) shows the relaxation time for both $C_2H_3Cl_3$ relaxations as a function of the inverse temperature (Arrhenius plot). The dielectric strength of each process, depicted in Figure 7.5 (b), is found to be basically independent of temperature, while the exponents (α_{CC}) of the Cole-Cole distributions (Figure 7.5 (c)) are found to decrease with decreasing temperature. A lower Cole-Cole exponent implies a wider distribution of relaxation times, consistent with the larger spectral width at low temperature (compare for example the loss spectra at 195.5 and 150.5 K in Fig. 7.4). Such increase in spectral width with decreasing temperature is common to many disordered systems.[44]

It is observed in Figure 7.5 (a) that both relaxations follow, at least within the studied temperature range, a simply-activated (Arrhenius) temperature dependence. The activation energies (E_a) of both relaxations (Figure 7.5 (a)) are virtually identical, namely 0.37±0.02 eV for the slower (lower-frequency) relaxation and 0.36±0.03 eV for the faster (higher-frequency) one, or equivalently, approximately 36 kJ/mol in both cases. By extrapolating the Arrhenius behavior to high temperature, the attempt time of the two relaxations are obtained as $\log(\tau_\infty(s)) = -14$ and $\log(\tau_\infty(s)) = -15$ for the slower and faster relaxations, respectively. These values are in agreement with the expectation for a dipolar process at high temperature (where all processes are non-cooperative due to the high thermal excitation), and are typical values for dielectric relaxations in glass-forming systems. We point out that, since we cannot reliably separate the two contributions to the dielectric loss at low temperatures (due to the increased spectral width), we cannot exclude a deviation from simply-activated behavior at low *T*.

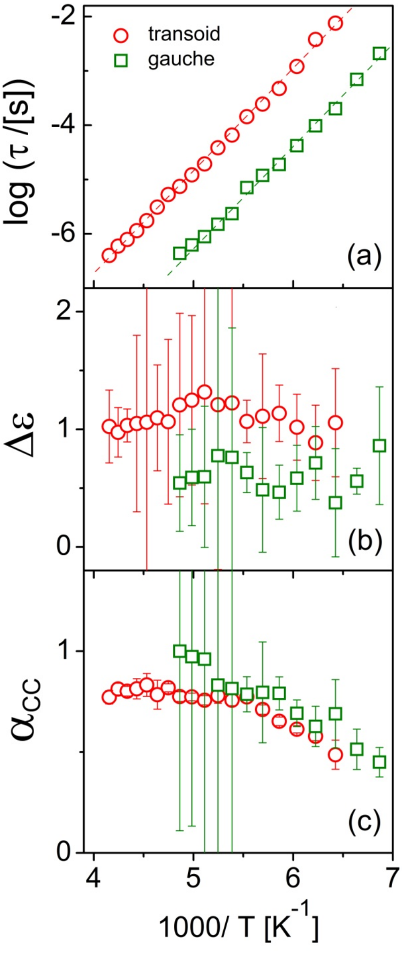

Figure 7.5 (a) Arrhenius plots of the relaxation times τ of $C_2H_3Cl_3$ molecules in the solvate (markers), together with the Arrhenius fits (dashed lines). Dielectric strength Δε (b) and Cole-Cole exponent α_{CC} (c) of both solvate relaxations, as a function of the inverse temperature. In all panels, open circles and squares represent the *transoid* relaxation, respectively.

It is worth pointing out that both the simply-activated nature and the Cole-Cole profile of the relaxation features are uncommon for cooperative primary relaxations associated with a glass transition,[1] and are instead typical of primary relaxations in non-viscous, non-polar solvents or of so-called secondary (local) relaxations in glass formers.[44] In the solvate, the $C_2H_3Cl_3$ molecules may be expected to interact only weakly with one another: each $C_2H_3Cl_3$ has only one $C_2H_3Cl_3$ first neighbor, namely the molecule that shares the same cavity, while all other next-neighbors are fullerenes (Figure 7.3). Apart from the solvent molecules sitting in the same interstitial site, the separation between ethane derivatives is thus larger than the van der Waals diameter of the C_{60} molecule, which is of the order of 1 nm,[45] leading to a relatively large inter-molecular separation compared to pure $C_2H_3Cl_3$. In other words, the polarization interactions with the quasi-spherical fullerene molecules are expected to be predominant, while interactions between $C_2H_3Cl_3$ molecules (dipole-dipole or steric) are less important. This discussion and the spectral properties of both relaxations indicate that the observed dynamic processes are at most weakly cooperative, and should rather be classified as (local) secondary relaxations.

Given that the crystallographic sites occupied by the solvent molecules are very similar to one another, the observed difference in relaxation time between both dynamic processes cannot be due to the different positions occupied by the $C_2H_3Cl_3$ molecules. Instead, it is likely that the origin of the two relaxations is the isomerism of the ethane derivatives. The two $C_2H_3Cl_3$ conformers have quite different dipole moments, of magnitude 1.44 D for the *gauche* isomer and 2.95 D (*i.e.*, more than twice as much) for the *transoid* isomer.[46.47] We thus assign each relaxation process to the reorientational dynamics of a different

(1,1,2)-trichloroethane conformer. On the other hand, *transoid-gauche* and/or *gauche–gauche* isomer fluctuations (internal rotations) would not result in two relaxations well separated in frequency. Moreover, conformational relaxations are expected to be significantly faster than the observed dynamics. A preliminary study on the conformationally-disordered solid phase of (1,1,2)-trichloroethane, where isomeric fluctuations take place, shows that the main relaxation dynamics visible by BDS is indeed faster than either dynamic process in the solvate, confirming our interpretation of the dielectric loss features as due to a dynamic *orientational* disorder.

To confirm the presence of both conformers, we characterized the solvate by means of Raman spectroscopy. Vibrational and NMR studies on the pure solvent have shown that the $C_2H_3Cl_3$ molecules exist in both conformations[46] in the liquid phase, with comparable concentrations,[48,49] and that each conformer has a specific vibrational signature.[47] Given that two conformers are present in the solution used to form the solvate, it is possible that they are also present in the solvate; however, the occurrence and relative concentration of conformers varies according to the nature of the system,[50] and depend~~s~~ on the subtle balance of intramolecular strains and the effects of the molecular environment.[34] For example, the *gauche* conformer is energetically more stable and by far the most abundant in the gas phase,[47] where intermolecular interactions are negligible. In the disordered solid phase of pure $C_2H_3Cl_3$ only *gauche* conformers are present, and they undergo dynamic conformational changes between isomers of different chirality.[34] Quite oppositely, in the fully ordered crystalline phase of (1,1,2)-trichloroethane only *transoid* conformers are observed.

We acquired Raman spectra on the polycrystalline C_{60}:$C_2H_3Cl_3$ powder, on pristine C_{60} and on the pure liquid solvent (always using the same substrate), to positively identify the weak features corresponding to the different conformers. Figure 7.6 shows a Raman micrograph of solvate crystallites, where a rectangular platelet and a ten-sided prism can be observed. The crystallite shapes are similar to those of the SEM photographs of the solvate published in reference 35.

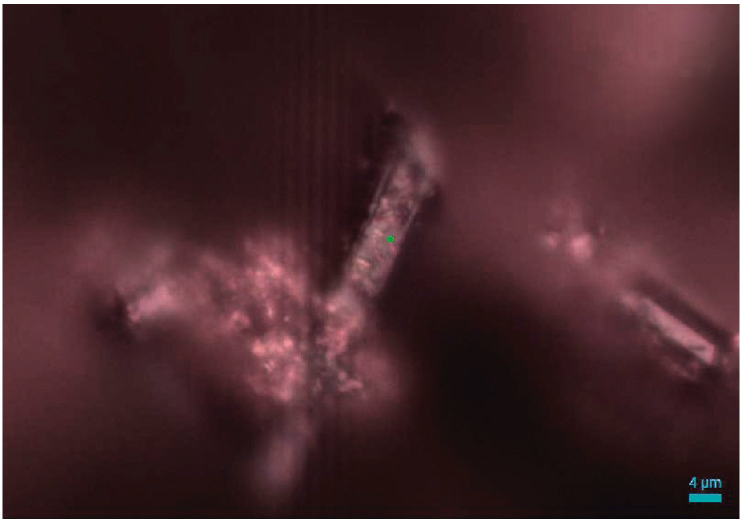

Figure 7.6 Raman microscopy image of solvate crystallites. The bright green spot is produced by the excitation laser and indicates the measuring position of the Raman spectrum of the solvate.

Figure 7.7 (a) shows the Raman spectrum of the C_{60}:$C_2H_3Cl_3$ solvate compared to that of the pure $C_2H_3Cl_3$ solvent. The solvate spectrum includes vibrations of both solvent and C_{60} molecules, the contribution of (1,1,2)- tricloroethane being comparatively weak due to the relatively small volume density of these molecules in the solvate structure. The relatively poor signal-to-noise ratio in the solvate spectrum might also be due to possible inhomogeneities in the material. Based on the Raman results presented in references 46 and 49 we are able to assign some of the vibrational modes of the C_{60}:$C_2H_3Cl_3$ solvate to either *gauche* or *transoid* $C_2H_3Cl_3$ conformers, and thereby conclude that both conformers are present in the solvate. In particular, the vibrations with wavenumbers of 335, 391, 666, 730, 774, 1211 and 1325 cm^{-1} (solid vertical lines in Figure 7.7 (a)) correspond to the *gauche* isomer, while those visible at 285, 525, 1008 and 1241 cm^{-1} (dashed lines) stem from the *transoid* isomer. Whereas the position of these bands did not change significantly with respect to liquid $C_2H_3Cl_3$, their intensities in the solvate were in general different from those of the pure solvent. The fact that the *gauche* Raman bands are more numerous and more intense on average suggests that the majority of ethane molecules are in the *gauche* conformation.

Figure 7.7 (b) shows a different Raman spectrum (middle curve) acquired on the solvate platelet visible in Fig. 7.6 in the range between 200 and 400 cm^{-1}. For comparison purposes, the solvate spectrum is shown together with that of the liquid solvent (upper curve) and that of pristine fullerite (lower curve). The *gauche* isomer bands at 335 and 391 cm^{-1} are clearly visible, as is the *transoid* peak at 285 cm^{-1}. While all three bands are also visible in liquid $C_2H_3Cl_3$, they are absent in the Raman spectrum of pristine fullerite. These results confirm that both conformations of (1,1,2)-trichloroethane are present in the solvate.

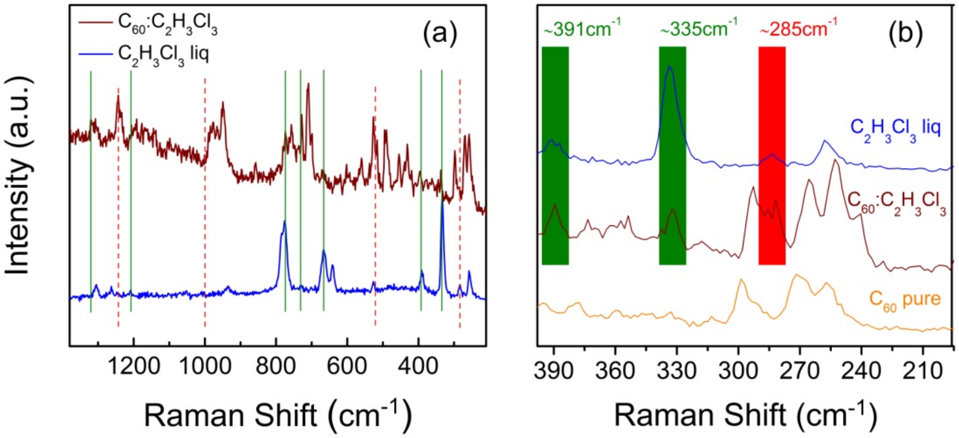

Figure 7.7 (a) Raman spectra of the C_{60}:$C_2H_3Cl_3$ solvate (upper curve) and of liquid $C_2H_3Cl_3$ (lower curve) between 200 and 1400 cm^{-1}. The vibration wavenumbers of modes corresponding exclusively to either the *transoid* or *gauche* $C_2H_3Cl_3$ conformers are highlighted with vertical (red) dashed lines and (green) solid lines, respectively. (b) Raman spectra of liquid $C_2H_3Cl_3$ (upper curve), of the C_{60}:$C_2H_3Cl_3$ solvate (middle curve) and of pure solid C_{60} (lower curve), in the region between 200 and 400 cm^{-1}. The peaks in the spectral regions highlighted in green are due to skeletal deformations of the *gauche* conformer, while that in the red shaded region is due to skeletal vibrations of the *transoid* conformer.

Due to the large difference in dipole moment of the two conformers, in organic binary systems containing $C_2H_3Cl_3$ the intermolecular interactions with the organic co-solvent shifts the conformational equilibrium, with the relative abundances of each conformer depending on the dielectric constant of the mixture and the molecular structure of co-solvent.[47] In the C_{60} solvate, dipolar interactions between the ethane molecules are weaker than in the solid phases of $C_2H_3Cl_3$ due to the presence of the C_{60} spacers[51] Moreover, due to the disorder present in this phase they might be more isotropic compared to solid $C_2H_3Cl_3$

phases and similar in strength to those of the pure liquid solvent, which might rationalize the occurrence of both isomers in the solvate.

As mentioned previously, both measured relaxations exhibit very close activation energies (36 kJ/mol in both cases), which might be due to the fact that the molecular environment of both conformers is virtually the same. On the other hand, the two dynamic processes are observed at quite different relaxation times; such difference is likely due to the fact that the motion of the $C_2H_3Cl_3$ dipoles in the solvate is hindered by the high polarizability of the C_{60} matrix[52,53] resulting in a polarization cloud which must rearrange at each reorientation of the $C_2H_3Cl_3$ molecule and therefore to an effective electrostatic drag acting against the orientational dynamics. Since the induced polarization is larger in the case of the larger permanent dipole of the *transoid* conformer, we assign the slower reorientational motion at lower frequency (longer characteristic times) to the *transoid* isomer, and the faster one to the *gauche* isomer. The freezing temperature of the two motions, defined as it is customary as the temperature at which a given process reaches a characteristic relaxation time of 100 seconds,[54] can be extrapolated assuming that their simply-activated behavior holds for all temperatures. The freezing temperature of the *transoid* relaxation is found to be approximately 170 K while that of the *gauche* relaxation is around 100 K. If the relaxation of the (1,1,2)-trichloroethane molecules were a cooperative process, one would expect a single (glass-transition) temperature to mark the simultaneous freezing of a single, cooperative dynamic process. The observation of two separate relaxations is therefore indicative of non-cooperative, single-molecule-like nature of the molecular dynamics in the solvate.

With this assignment of the dielectric losses, it is found that the dielectric strength ($\Delta\varepsilon$) of the *transoid* relaxation ($\Delta\varepsilon_{transoid}$ = 1.1±0.1) is roughly twice that of the *gauche* relaxation ($\Delta\varepsilon_{gauche}$ = 0.6±0.2), as indicated in Figure 7.5 (b). The dielectric strength of a relaxation involving a dipolar moiety is proportional to the square of the molecular dipole moment μ and to the density of dipoles ($N/_V$),[54] *i.e.*, $\Delta\varepsilon \propto \mu^2\, N/_V$. The proportionality coefficient actually contains the so-called Kirkwood correlation factor,[55] which describes the degree of correlation between the relative orientations of (nearest-neighbor) dipoles during the reorientation dynamics. In view of the similar origin of the two relaxation processes, one may assume that the Kirkwood correlation factor is approximately the same for both dynamics. Under this assumption, and considering that the dipole moment of the *transoid* conformer is twice that of the *gauche* one, if the two conformers had equal populations their strength would differ by a factor of four. The fact that the two strengths are in a ratio close to 2 to 1 would instead indicate that the *gauche* conformation is more abundant in the solvate, in agreement with our Raman and XRD results.

As a final remark, we note that the observation in the solvate of molecular dynamics involving the ethane molecule suggests that also the fullerene species may display merohedral reorientational motions in this phase. This would not be surprising considering that the C_{60} molecules usually display rotational dynamics also when intercalated with other organic molecules.[23,26,27]

7.5 Conclusions

We presented a full characterization of the dynamic statistical disorder in the solvate of C_{60} with (1,1,2)-trichloroethane ($C_2H_3Cl_3$). Our study included the determination, for this solid phase, of molecular conformations, lattice structure, positional and orientational disorder, and molecular dynamics down to the microsecond timescale. Both *gauche* and *transoid* conformations of the $C_2H_3Cl_3$ species are present in the solvate, with a majority of *gauche* conformers. The two conformers exhibit separate dynamics with roughly simply-activated temperature dependence and Cole-Cole spectral profile, implying that they are local, at most weakly cooperative, relaxations of $C_2H_3Cl_3$ molecules "diluted" in the fullerene matrix. The isomer with larger dipole moment (*transoid*) polarizes more strongly the C_{60} moieties, resulting in a more pronounced electrostatic drag against dipole reorientations and thus slower reorientational motion compared to the *gauche* conformer. The low degree of dynamic cooperativity in the solvate evidenced by the observation of two separate relaxations of the $C_2H_3Cl_3$ molecules, contrasts with the collective character of molecular relaxation dynamics in most glass-forming systems. Such low cooperativity likely stems from the presence of the C_{60} molecules, acting as highly polarizable spacers that effectively decouple the molecular dynamics.

Our study provides hard-to-obtain information on the molecular arrangement in a binary organic co-crystal, and to the best of our knowledge it is the first-ever report of the relaxation dynamics of guest molecules in C_{60} solvates. The obtained results show that the characteristic reorientational relaxation times of dipolar species depend on the details of intermolecular coupling such as dipole-induced dipole (polarization) interactions. Considering the very broad variety of structures with dynamic disorder that can be obtained with fullerene solvates with different solvent or guest molecules, orientationally disordered C_{60} solvates represent model systems to investigate the impact of the structure and thus of the interaction geometry on the molecular dynamics of heterogeneous polar systems.

Bibliography

[1] R. Brand, P. Lunkenheimer, A. Loidl, *J. Chem. Phys.,* vol. 116, p. 10386, 2002.

[2] M. Zuriaga, L.C. Pardo, P. Lunkenheimer, J.L. Tamarit, N. Veglio, M. Barrio, F.J. Bermejo, A. Loidl *Phys. Rev. Lett.,* vol. 103, p. 075701, 2009.

[3] A.I. Krivchikov, G. A. Vdovichenko, O. A. Korolyuk, F.J. Bermejo, L.C. Pardo, J.Ll. Tamarit, A. Jezowski, D. Szewczyk *J. Non-Cryst. Solids*, vol. 407, p. 141, 2015.

[4] M. J. Zuriaga, S. C. Perez, L.C. Pardo, J.L. Tamarit *J. Chem. Phys*. Vol. 137, p. 054506, 2012.

[5] I.V. Sharapova, A.I. Krivchikov, O.A. Korolyuk, A. Jezowski, M. Rovira-Esteva, J.Ll. Tamarit, L.C. Pardo, M.D. Ruiz-Martin, F.J. Bermejo *Phys. Rev. B*, vol. 81, p. 094205, 2010.

[6] M. Zachariah, M. Romanini, P. Tripathi, J.Ll. Tamarit, R. Macovez, *Phys. Chem. Chem. Phys.* Vol.17, p. 16053, 2015.

[7] G.A. Vdovichenko, A.I. Krivchikov, O.A. Korolyuk, J.L. Tamarit, L.C. Pardo, M. Rovira-Esteva, F.J. Bermejo, M. Hassaine, M.A. Ramos. *J. Chem. Phys.*, vol. 143, p. 084510, 2015.

[8] S. C. Perez, M. J. Zuriaga, P. Serra, A. Wolfenson, P. Negrier, J.L. Tamarit*. J. Chem. Phys.* vol. 143, p. 134502, 2015.

[9] Ph. Negrier, M. Barrio, J.L. Tamarit, D. Mondieig *J. Phys. Chem. B.,* vol. 118, p. 9595, 2014.

[10] Ph. Negrier, M. Barrio, M. Romanini, J.L. Tamarit, D. Mondieig, A.I. Krivchikov, L. Kepinski, A. Jezowski, D. Szewczyk *Cryst. Growth Des.,* Vol.14, p. 2626, 2014.

[11] R. Tycko, G. Dabbagh, R.M. Fleming, R.C. Haddon, A.V. Makhija, S.M. Zahurak *Phys. Rev. Lett.* vol. 67, p. 1886, 1991.

[12] W.I.F. David, R.M. Ibberson, J.C. Matthewman, K. Prassides, T.J.S. Dennis, J.P. Hare, H.W. Kroto, R. Taylor, D.R.M. Walton, *Nature.*, vol. 353, p. 147, 1991.

[13] A. Goldoni, C. Cepek, R. Larciprete, L. Sangaletti, S. Pagliara, G. Paolucci, M. Sancrotti *Phys. Rev. Lett.,* vol. 88, p. 196102, 2002.

[14] R. Macovez, A. Goldoni, L. Petaccia, I. Marenne, P.A. Brühwiler, P. Rudolf *Phys. Rev. Lett.,* vol. 101, p. 236403, 2008.

[15] M.A. Ramos, S. Vieira, F.J. Bermejo, J. Dawidowski, H.E.; Schober H. Fischer, M.A. González, C.K. Loong, D.L. Price *Phys. Rev. Lett.,* vol. 78, p. 82, 1997.

[16] S. Benkhof, A. Kudlik, T. Blochowicz, E. Rössler *J. Phys. Condens. Matter.*, vol. 10, p. 8155, 1998.

[17] M. Jiménez-Ruiz, M.A. González, F.J. Bermejo, M.A. Miller, N.O. Birge, I. Cendoya, A. Alegría *Phys. Rev. B.*, vol. 59, p. 9155, 1999.

[18] M. Götz, Th. Bauer, P. Lunkenheimer, A. Loidl *J. Chem. Phys.* Vol. 140, p. 094504, 2014.

[19] F. Gugenberger, R. Heid, C. Meingast, P. Adelmann, M.; Braun, H. Wuhl, M. Haluska, H. Kuzmany *Phys. Rev. Lett.,* vol. 69, p. 3774, 1992.

[20] P.A. Heiney, J.E. Fischer, A.R. McGhie, W.J. Romanow, A.M.; McCauley, J.P. Denenstein, A.B. Smith, D.E. Cox *Phys. Rev. Lett.,* vol. 66, p. 2911, 1991.

[21] M. Mehring, K.F. Their, F. Rachdi, T. de Swiet *Carbon.*, vol. 38, p. 1625, 2000

[22] I.S. Neretin, Y.L. Slovokhotov, *Russ. Chem. Rev.,* vol. 73, p. 455, 2004.

[23] S. Pekker, É. Kováts, G. Oszlányi, G. Bényei, G. Bortel, G. Klupp, I. Jakab, E. Jalsovszky, F. Borondics, K. Kamarás, M. Bokor, G. Kriza, K. Tompa, G. Faigel *Nat. Mater.,* vol. 4, p. 764, 2005.

[24] C. Collins, J. Foulkes, A.D. Bond, J. Klinowski *Phys. Chem. Chem. Phys.*, vol. 1, p. 5323, 1999.

[25] E. Mitsari, M. Romanini, M. Zachariah, R. Macovez *Curr. Org. Chem.,* vol. 20, p. 645, 2016.

[26] C. Collins, M. Duer, J. Klinowski *Chem Phys. Lett.,* vol. 321, p. 287, 2000.

[27] J. Rozen, F. Masin, R. Ceolin, H. Szwarc *Phys. Rev. B.,* vol. 70, p. 144206, 2004.

[28] F. Masin, D. Gall, G. Gusman *Solid State Commun.,* vol. 91, p. 849, 1994.

[29] F. Masin, D. Gall, G. Gusman *Solid State Commun.,* vol. 91, p. 849, 1994.

[30] A.S. Grell, F. Masin, R. Céolin, M.F. Gardette, H. Szwarc *Phys. Rev. B.*, vol. 62, p. 3722, 2000.

[31] K.L. Ngai, S. Capaccioli, S. Ancherbak, N. Shinyashiki *Philos. Mag.,* vol. 91, p. 1809, 2011.

[32] S. Capaccioli, K.L. Ngai, *J. Chem. Phys.,* vol. 135, p. 104504.

[33] Einfeldt, J.; Kwasniewski, A. Characterization of Different Types of Cellulose by Dielectric Spectroscopy. *Cellulose* **2002**, *9*, 225–238.

[34] M. Bujak, M. Podsiadło, A. Katrusiak *Chem. Commun.,* vol. 37, p. 4439, 2008.

[35] F. Michaud, M. Barrio, D.O. Lopez, J.Ll. Tamarit, V. Agafonov, S. Toscani, H. Szwarc, R. Céolin *Chem. Mater.* vol. 12, p. 3595, 2000.

[36] G. Oszlanyi, G. Bortel, G. Faigel, S. Pekker, M. Tegze, R.J. Cernik *Phys. Rev. B* vol. 48, p. 7682, 1993.

[37] S. Toscani, H. Allouchi, J.L. Tamarit, D.O. Lopez, M. Barrio, V. Agafonov, A. Rassat, H. Szwarc, R. Céolin *Chem. Phys. Lett.*, vol. 330, p. 491, 2000.

[38] G. Faigel, G. Bortel, G. Oszlányi, S. Pekker, M. Tegze, P.W. Stephens, D. Liu *Phys. Rev. B* vol. 49, p. 9186, 1994.

[39] F. Michaud, M. Barrio, S. Toscani, D.O. Lopez, J.L. Tamarit, V. Agafonov, H. Szwarc, R. Céolin *Phys. Rev. B* vol. 57, p. 10351, 1998.

[40] M.M. Olmstead, F. Jiang, A.L. Balch *Chem. Commun.,* vol. 6, p. 483, 2000.

[41] A.L. Balch, J.W. Lee, B.C. Noil, M.M. Olmstead *J. Chem. Soc., Chem. Commun.,* vol. 1, p. 56, 1993.

[42] M.V. Korobov, A.L. Mirakian, N.V. Avramenko, E.F. Valeev, I.S. Neretin, Y.L. Slovokhotov, A.L. Smith, G. Olofsson, R.S. Ruoff *J. Phys. Chem. B* vol. 102, p. 3712, 1998.

[43] U. Geiser, S.K. Kumar, B.M Savall, S.S. Harried, K.D. Carlson, P.R.; Wang, H.H. Mobley, J.M. Williams, R.E. Botto *Chem. Mater.*, vol. 4, p. 1077, 1992.

[44] C.J.F. Böttcher, P. Bordewijk *Theory of Electric Polarization. Volume II: Dielectrics in Time-Dependent Fields*. Amsterdam: Elsevier Science, 1978.

[45] S. Saito, A. Oshiyama *Phys. Rev. Lett.,* vol. 66, p. 2637, 1991.

[46] A. Buin, H. Wang, S. Consta, Y. Huang *Micropor. Mesopor. Mat.,* vol. 183, p. 207, 2014.

[47] J.I. Iribarren, J. Casanovas, D. Zanuy, C. Aleman *Chem. Phys.,* vol. 302, p. 77, 2004.

[48] K. Kuratani, S. Mizushima *J. Chem. Phys.,* vol. 22, p. 1403, 1954.

[49] S.D. Christian, J. Grundnes, P. Klaeboe, C.J. Nielsen, T. Woldbaek *J. Mol. Struct.,* vol. 34, p. 33, 1976.

[50] R. Macovez, N. Lopez, M. Mariano, M. Maymò, J. *J. Phys. Chem. C.,* vol. 116, p. 26784, 2012.

[51] R. Swietlik, P Byszewski, E. Kowalska *Chem. Phys. Lett.,* vol. 254, p. 73, 1996.

[52] R. Macovez, M.R.C. Hunt, A. Goldoni, M. Pedio, P. Rudolf *J. Electron. Spectrosc.,* vol. 183, p. 94, 2011.

[53] R. Macovez, M. Zachariah, M. Romanini, P. Zygouri, D. Gournis, J.L. Tamarit *J. Phys. Chem. C.,* vol. 118, p. 12170, 2014.

[54] F. Kremer, A. Schönhals, *Broad Band Dielectric Spectroscopy*. Berlin: Springer, 2003.

[55] J.G. Kirkwood *J. Chem. Phys.,* vol. 7, p. 911, 1939.

CONCLUSIONS

Organic molecular materials are usually characterized by relatively weak intermolecular forces of dispersive (van der Waals) origin, which result in characteristic orientational disordered phases and solid-to-solid (order-disorder) transitions. The disorder inside the solids is also partially responsible for the localization of valence electrons on single molecules, so that electron hopping is the main charge transport mechanism and the dc conductivities are rather low. This thesis focuses on the relaxation dynamics and charge-conduction effects of small dipolar molecules hosted by molecular solids, and present at the surface of crystalline grains (such as hydration water) or inside the grain themselves as structural component (such as solvent molecules in a solvate). These properties were studied using temperature-dependent broadband dielectric spectroscopy as main experimental tool. Studying the dynamics of guest molecules enclosed in host systems allows investigating the impact of the structure and of microscopic interactions on the molecular dynamics of heterogeneous systems. As to the conductivity, an enhancement of the dc conductivity and of space-charge relaxation effects was observed when hydration water was present. The dielectric spectroscopy study allows rationalizing both findings.

Water-related relaxation dynamics were investigated in two different molecular solids, namely the solid phases of a rhodamine dye (Rh6G) and of a fullerene derivative (fullerenol), in order to identify possible common signatures of the water present in two different organics, as well as features that could differentiate the behavior of water in different molecular environments. Both materials are hygroscopic and can capture and retain water molecules from the surrounding atmosphere. The presence of water was confirmed by thermal and infrared analysis, both showing the existence of different water environments. Thanks to the dipolar nature of water molecules, their dynamic signature in the dielectric spectra was quite prominent in both molecular systems.

Three different relaxations were ascribed to water inside Rh6G. Two of them stem from reorientational motions of water molecules in different hydration layers on the surface of Rh6G grains. The lowest temperature relaxation has the characteristic traits of the so-called single-water-molecule (β) relaxation of water observed in various water-containing systems, and which appears to stem from water only weakly bonded to the organic substrate. The relaxation at intermediate temperature is instead probably related to the rotational motions of interfacial water molecules interacting directly with the Rh6G grains (in the first or second hydration layers). Both relaxations have reproducible characteristic times in different samples. The third relaxation related to water is a space-charge relaxation associated with the protonic species, which are responsible for a water-induced charge transport mechanisms occurring through the hydration layers, and which is visible as a significant increase of the dc conductivity with respect to pure (water-free) solid Rh6G.

The Rh6G powder also displays two intrinsic relaxations, which are observed also in Rh6G thin films. The faster one, which is affected by the presence of water, is assigned to a local dipolar motion involving the charged nitrogen atom of the Rh6G cation and the chlorine counter-ion, while the slower is related with a space-charge relaxation of electronic charge carriers, namely, the accumulation of electrons/holes at the grain boundaries of the pure powder.

Hydrated fullerenol is characterized by a significantly higher water content, as visible from the observation of the melting of (bulk-like) ice clusters at 273 K. The presence of ice is also detected by means of dielectric spectroscopy, by the existence of a relaxation below 230 K which is due to the diffusion of orientational defects throughout the bulk-like ice network. As in the case of Rh6G, the hydration water introduces a new conduction mechanism at sufficiently high hydration level, which is the same as in bulk water (or ice), namely the Grotthus proton exchange mechanism. This new conduction mechanism and pathway also entails the existence of a protonic space-charge relaxation associated with the proton hopping, which is visible at higher temperature, close to the temperature of water desorption.

Besides these two relaxations, associated directly with a dielectric response of water moieties present in relatively large quantities (several hydration layers or clusters), another one is observed at intermediate temperatures. The fact that this relaxation is also present in the quasi-anhydrous sample, where the conductivity is due to electronic charge carriers, and that the pure material is not expected by symmetry to display any intrinsic orientational relaxation, imply that this process has an electronic space-charge origin. When the powder is hydrated, the large polarizability of the surface water molecules contributes to this interfacial relaxation, thus modifying its properties and temperature dependence.

Space-charge relaxations due to electronic charge carriers in quasi-anhydrous powders and due to protonic charges in hydrated samples displayed similarities in both materials. The protonic space-charge relaxation showed atypical temperature behavior in both samples due to the conductivity decrease upon desorption of water at high temperature.

An electronic space-charge relaxation due to accumulation of the electronic carriers at the grain boundaries was observed also in another C_{60} derivative, oxofullerol (oxC_{60}). This newly-synthesized molecule is characterized by oxygen-containing functional groups (hydroxyl, carbonyl, and epoxy oxygens) covalently bonded onto the surface of the buckyballs, which lead to hygroscopic behavior, and most importantly, to the formation of a hydrogen-bond network between the oxC_{60} moieties. Upon water desorption, the oxC_{60} molecules not only maintain their integrity, but actually display intriguing orientational phase transitions reminiscent of the phase behavior of other fullerene solids. A hydrogen-bonded network appears to be present in the room-temperature solid phase of water-free oxC_{60}, which exhibits an ordered, low-symmetry structure without molecular motions. The rotational melting of the oxC_{60} moieties takes place in at least two steps, with an intermediate partially ordered phase separating the ordered room-temperature phase and the disordered high-temperature phase. The latter seems to be characterized by dynamical reorientational motions.

The dc conductivity of oxC_{60} displays changes across all rotational phase transitions. A space-charge relaxation is detected, which fulfills the Barton-Nakajima-Namikawa relation typical of relaxations stemming from conductivity heterogeneity. Across the high temperature phase transition (full rotational melting), the dc conductivity is observed to decrease as in the analogous transition at 260 K in pristine fullerite (C_{60}).

Finally, to study the effect on organic materials of guest species other than water, in the last chapter of this thesis a non-covalently bonded fullerene complex with an ethane derivative was probed. In detail, this chapter dealt with the solvate of C_{60} with (1,1,2)-trichloroethane, in which we determined the molecular conformations of the chloroethane molecules, the lattice structure and disorder, and the guest-molecule orientational dynamics down to the microsecond timescale. Both gauche and transoid conformations of the (1,1,2)-trichloroethane species were detected in the solvate, with a majority of gauche conformers. The two conformers exhibited separate dynamics with roughly simply-activated temperature dependence and Cole-Cole spectral profile, implying that they are local, at most weakly cooperative, relaxations of (1,1,2)-trichloroethane molecules “diluted” in the fullerene matrix. The isomer with larger dipole moment (transoid) polarized more strongly the C_{60} moieties, resulting in a more pronounced electrostatic drag against dipole reorientations and thus slower reorientational motions compared to the gauche conformer. The low degree of dynamic cooperativity likely stems from the presence of the C_{60} molecules acting as highly polarizable spacers that effectively decouple the molecular dynamics. The results show that the characteristic reorientational relaxation times of dipolar species depend on the details of intermolecular coupling such as dipole-induced dipole (polarization) interactions. Considering the very broad variety of structures with dynamic disorder that can be obtained with fullerene solvates with different solvent or guest molecules, we conclude orientationally disordered C_{60} solvates could become model systems to investigate the impact of the structure and thus of the interaction geometry on the molecular dynamics of heterogeneous binary systems.

The conclusions reached in this thesis should provide a sound basis for further investigations of the relaxation dynamics and conductivity properties of host-guest systems in particular and of heterogeneous systems in general. They represent a first step in the direction of extending the current experimental knowledge of disordered solid or quasi-solid phases to more complex systems of relevance in organic chemistry, biology, and related commercial applications.

LIST OF PUBLICATIONS

- R. Macovez, E. Mitsari, M. Zachariah, M. Romanini, P. Zygouri, D. Gournis, J. Ll. Tamarit Ultraslow Dynamics of Water in Organic Molecular Solids. *J. Phys. Chem. C* 118, 4941 (2014)

- E. Mitsari, M. Romanini, N. Qureshi, J. Ll. Tamarit, M. Barrio, R. Macovez C_{60} Solvate with (1,1,2)-Trichloroethane: Dynamic Statistical Disorder and Mixed Conformation. J. Phys. Chem. C (2016). DOI: 10.1021/acs.jpcc.6b02321

- E. Mitsari, M. Romanini, M. Zachariah, R. Macovez Solid State Physicochemical Properties and Applications of Organic and Metallo-Organic Fullerene Derivatives. *Curr. Org. Chem.* 20, 645 (2016)

- P. Zygouri, K. Spyrou, E. Mitsari, M. Barrio, R. Macovez, D. Gournis, P. Rudolf A facile synthetic approach based on Staudenmaier's method to hydrophilic oxidized buckminsterfullerene and its derivatives. Submitted.

Acknowledgements

So, I think that's it! It was a quite nice race...a relay race actually. I am really thankful for meeting all of you, people, and share moments with you.

Roberto, I was really lucky having you as my supervisor. Physics sounds way much better now. Thank you for everything, for all the support professionally and personally. I really want to thank Josep Lluis Tamarit for giving me the opportunity to work in the group and starting my academic life in GCM group. It was really nice working and sharing moments with you, GCM people.

I am also really lucky for having all the "non-uni" friends in my life all these years. Long talks, beers, dinner-times, tapas, long walks, barbacoas etc. are the best things have sharing with all of you. Thank you so much.

Επίσης, θέλω να ευχαριστήσω απίστευτα τους γονείς μου για όλη την αγάπη, την εμπιστοσύνη και συμπαράσταση αυτά τα χρόνια!

Un gracias grandísimo al Isaac Sánchez por su ayuda con la estética de la tesis y la compresión de todos estos días.

Ευχαριστώ! Thank you! Gracias!